



Utrecht University

# Probing the Surface pH during CO<sub>2</sub> Electroreduction using *in situ* Raman Spectroscopy

*Master Thesis*

*Inorganic Chemistry and Catalysis*

*Part of the Debye Institute for Nanomaterials Science*

*By Jan den Hollander*

**Under the supervision of  
Jim de Ruiter MSc  
dr. Ward van der Stam  
2020 – 2021**

## Abstract

The electrochemical reduction reaction of  $\text{CO}_2$  is a promising way of using carbon dioxide as a feedstock for more useful chemicals. Using a copper electrode as electrocatalyst, a variety of products can be formed, such as  $\text{CO}$ , ethylene and methanol. When using a neutral pH electrolyte, all  $\text{CO}_2$  reduction reactions form  $\text{OH}^-$  as a side-product, which increases the local pH on the electrode surface. As pH is known to have an effect on the selectivity of the copper electrocatalyst, local pH tracking can lead to more insight into the  $\text{CO}_2$  reduction reaction and may improve product-specific tuning of the reaction. In this work, our goal was to track the local pH development during  $\text{CO}_2$  electroreduction on copper, using Raman spectroscopy to interrogate our pH probes adsorbed on the electrode surface. To get a strong enough Raman signal, we made use of Shell-Isolated Nanoparticle-Enhanced Raman Spectroscopy (SHINERS) by using plasmon resonance induced by gold nanoparticles. These particles are functionalized with a pH-dependent Raman reporter molecule that undergoes changes to its Raman spectrum based on surrounding pH. Herein, we managed to successfully synthesize two pH probes based on two different organic molecules: 4-mercaptobenzoic acid and 4-mercaptophenol. The molecules were adsorbed on gold nanoparticles, which were then covered in a thin layer of silica to improve stability of the nanoparticles by preventing aggregation and to isolate the probes from electronic effects. Calibration curves which correlate Raman spectral changes to pH were successfully determined for both probes, and indicated that the pH sensitive regions were 6-8 for 4-MBA and 10-13 for 4-MP. When applying the probes in electrochemical environments, we found that applied reductive potentials cause electronic effects that influence the Raman spectra (such as peak shifts or intensity changes), despite the isolating silica coating. This complicated the measurements and made it difficult to quantitatively track the pH during electroreduction of  $\text{CO}_2$ . Still, we found that the pH reported by the 4-MBA probe increased with more negative potentials and decreased with less negative potentials. This is in agreement with the expected  $\text{OH}^-$  formation at reductive (negative) potentials, and subsequent diffusion away from the surface at less negative (or positive) potentials. Our work provides a good starting point for the use of SHINERS as pH probing tool in electrochemistry as we discovered several effects that should be taken into account for future research.

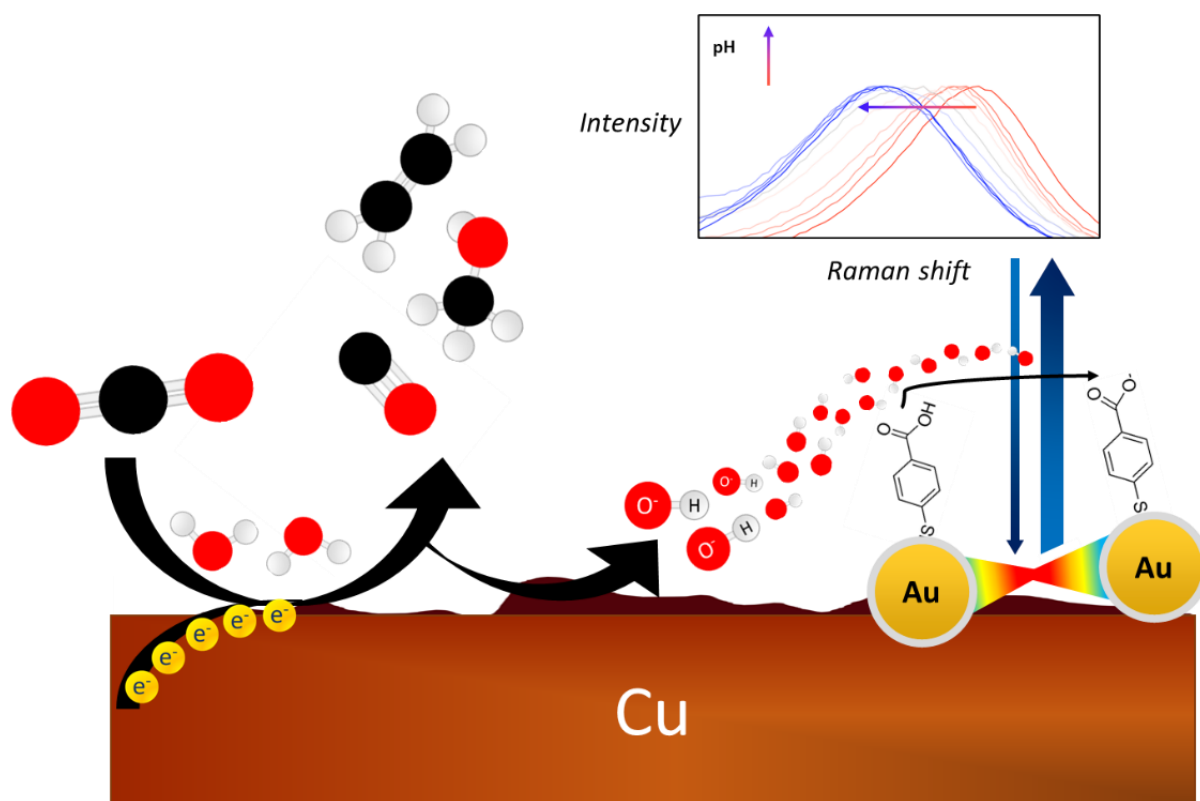


## Table of contents

1	General introduction .....	4
2	Theory.....	7
2.1	Electrochemistry.....	7
2.1.1	Setups and measurement modes.....	7
2.1.2	Electrochemical equations: Faradaic efficiency and Nernst equation .....	8
2.1.3	Electrochemical experiments: cyclic voltammetry and chronoamperometry .....	9
2.1.4	CO <sub>2</sub> reduction .....	10
2.2	Raman spectroscopy .....	13
2.2.1	Surface-, Tip- and Shell-Isolated Nanoparticle-Enhanced Raman Spectroscopy .....	15
2.2.2	SERS and SHINERS in electrochemical systems .....	16
2.3	pH probing methods.....	18
3	Methods .....	21
3.1	Chemicals.....	21
3.2	Nanoparticle synthesis .....	21
3.3	Characterization and experimental procedures of pH probes.....	22
4	Results and discussion.....	24
4.1	Preparation of Au-MBA@SiO <sub>2</sub> and Au-MP@SiO <sub>2</sub> pH probes .....	24
4.2	Probe utilization for pH calibration curve determination .....	34
4.3	<i>In situ</i> Raman spectroscopy during electrochemical CO <sub>2</sub> reduction .....	38
4.3.1	Application of the Au-MBA@SiO <sub>2</sub> probe .....	38
4.3.2	Application of the Au-MP@SiO <sub>2</sub> probe .....	44
5	Conclusions.....	51
6	Outlook.....	51
7	Acknowledgements .....	53
8	References.....	54
9	Appendix.....	58

# 1 General introduction

As global warming is one of the most pressing matters of modern times, strategies to combat CO<sub>2</sub> emissions are essential for reducing our environmental footprint.<sup>1</sup> By using CO<sub>2</sub> as a feedstock, it is possible to store excess energy in chemical bonds by converting it into more useful products, such as carbon monoxide (for syngas), ethylene (for plastics) or methanol (for e.g. antifreeze)<sup>2,3</sup>. Furthermore, the repurposing of carbon dioxide is an elegant way of combating global warming and also takes us a step closer to a circular economy.

However, as carbon dioxide repurposing reactions have a substantial activation energy, catalytic reduction methods are vital in order to reduce the amount of necessary energy and thereby increase the efficiency of the reactions. One way of CO<sub>2</sub> utilization is thermocatalytic reduction<sup>3,4</sup>, but an alternative way is electrochemical reduction, which is the focus of this thesis. In electroreduction, the electrode is used as a catalytic surface for CO<sub>2</sub> adsorption and subsequent reduction. When using renewable energy to provide the current necessary for the reaction, this process forms a sustainable way of carbon dioxide repurposing<sup>5</sup>. Additionally, when using electrocatalysis, it is easier to overcome the reduction reaction activation energy with only a few volts, whereas in thermocatalysis a relatively high temperature is necessary.

The way this method works is by applying a negative potential to an electrode in an electrochemical system where CO<sub>2</sub> is present in the electrolyte (e.g. in a carbonate solution). The negative current subsequently initiates reduction reactions. Depending on potential and electrode surface morphology, the products formed can be C<sub>1</sub>, C<sub>2</sub>, and even some C<sub>3</sub> products<sup>6</sup>. For the reduction of CO<sub>2</sub> (typically done in intermediate pH electrolyte<sup>7</sup>), water is used as the proton source, which results in the formation of OH<sup>-</sup> as a side product (Table 1). This causes an increase in pH and because the reactions happen on the surface of the electrode, the pH near the surface undergoes the most significant changes. This is referred to as the local pH, which can deviate substantially from the bulk pH<sup>8-10</sup>. As the pH is believed to have an influence on the products formed by the CO<sub>2</sub> electroreduction<sup>11-13</sup>, measuring the local pH behavior can lead to deeper insight into the selectivity of the reduction reactions.

Table 1. Several CO<sub>2</sub> electroreduction reactions in neutral pH. Table reproduced from ref<sup>14</sup>.

CO <sub>2</sub> Reduction Half Reactions	[V] vs RHE
CO <sub>2</sub> + H <sub>2</sub> O + 2e <sup>-</sup> → CO + 2OH <sup>-</sup>	-0.10
CO <sub>2</sub> + H <sub>2</sub> O + 2e <sup>-</sup> → HCOO <sup>-</sup> + OH <sup>-</sup>	-0.03
CO <sub>2</sub> + 5H <sub>2</sub> O + 6e <sup>-</sup> → CH <sub>3</sub> OH + 6OH <sup>-</sup>	0.03
CO <sub>2</sub> + 6H <sub>2</sub> O + 8e <sup>-</sup> → CH <sub>4</sub> + 8OH <sup>-</sup>	0.17
2CO <sub>2</sub> + 8H <sub>2</sub> O + 12e <sup>-</sup> → C <sub>2</sub> H <sub>4</sub> + 12OH <sup>-</sup>	0.08

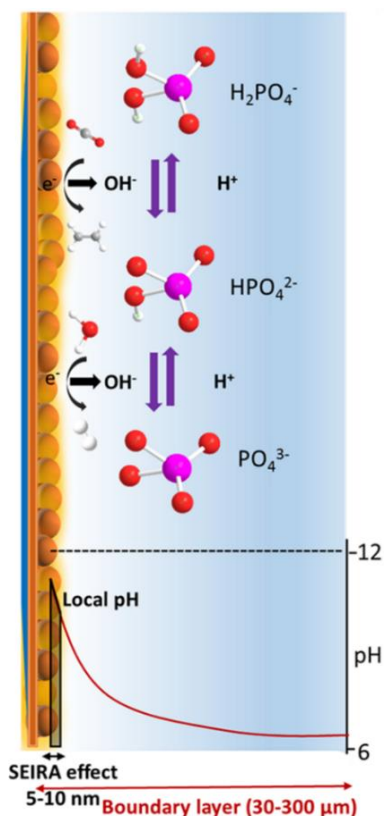


Figure 1. Representation of events on the surface of an electrode during electrochemical  $\text{CO}_2$  reduction in a phosphate-buffered electrolyte, and their effects on the local pH. As the boundary layer is  $30\text{-}300\ \mu\text{m}$  away from the electrode, the pH measurements are not directly on the surface. Figure reproduced from ref<sup>8</sup>.

Therefore, in our work we focused on tracking the pH behavior on, or up to a few hundred nanometers from, the surface of a copper electrode during  $\text{CO}_2$  electroreduction to get an even more local image of pH behavior. We used *in situ* Raman spectroscopy, for several reasons: it is a non-invasive technique and therefore does not destructively interact with the substrate. Another important reason is that the vibrational modes of water (the main part in the electrolyte) are Raman-inactive, which is convenient for surface-probing purposes, as there is no signal overlap between water molecules and reaction species.

Even though there are benefits to using Raman spectroscopy, the issue persists that Raman-active vibrations usually give very weak signals, because of the relatively low chance of inelastic light scattering (Raman scattering). To deal with this, we took advantage of Shell-Isolated Nanoparticle-Enhanced Raman Spectroscopy (SHINERS)<sup>15-18</sup>, which is an example of plasmon-enhanced Raman spectroscopy (PERS) and is elaborated in the theory chapter. Using this technique, the Raman signal becomes much stronger and molecules on the surface of the electrode can be measured directly and clearly and with a better time resolution (up to 1 second per spectrum) during electrochemical reduction of  $\text{CO}_2$ . This means that when a molecule that undergoes changes to its Raman spectrum based on the surrounding pH is placed on the surface, it might be possible to relate the changes in the spectrum to the change of pH. Such a molecule is called a (pH-dependent) Raman reporter, and this method of pH determination has previously been used by several research groups. For example, in the work of Scarpitti *et al.*<sup>19</sup>, they describe the use of an organic molecule called 4-mercaptobenzoic acid (4-MBA) in combination with SHINERS to determine the pH in live cells. They found the pH probe to be most sensitive around neutral pH, from around 6-8.

In this work, we broaden the application of 4-MBA as pH probe, making the transition from living cells to electrochemical environments. Additionally, we explored several other pH-dependent Raman

reporters, such as 4-mercaptophenol (4-MP), 4-nitrothiophenol and 3-amino-5-mercapto-1,2,4-triazole, to use during CO<sub>2</sub> electroreduction. However, only the 4-MBA and 4-MP probes proved successful. We started by focusing on the synthesis of these pH probes, which needed several optimization steps prior to using them in electrochemistry. Next, we determined pH calibration curves for both probes to be able to relate spectral changes to a quantitative pH value. The last step was to apply the pH probes to track the local pH during the electrochemical reduction of CO<sub>2</sub>. It appeared, however, that the introduction of an electric field in the form of an applied potential has influences on Raman signals that may not be neglected, such as wavenumber shifts or intensity changes. These effects and their causes are further elaborated in the theory chapter and throughout the results and discussion. Additional challenges of using a SHINERS-based pH probe in electrochemical environments include oxidation of the electrode surface and bubble formation, as they both contribute to disturbance of the Raman signal.

## 2 Theory

### 2.1 Electrochemistry

Electrochemistry describes the relation between electric potentials and chemical reactions. This means that using electrochemistry, chemical changes can be induced, such as reduction or oxidation reactions. As the focus in this work is on the electrochemical CO<sub>2</sub> reduction reaction, this chapter mainly focuses on this specific reaction.

#### 2.1.1 Setups and measurement modes

The principle of electrochemistry works by letting a current flow between a working electrode and a counter electrode through a solution with sufficient conductivity (the electrolyte). This is done by applying a potential using a potentiostat connected to the two electrodes (Figure 2). By using catalytically active material as the working electrode, it is possible to use the electrons for chemical reactions, like CO<sub>2</sub> reduction. Such a material acts as a surface for carbon dioxide molecules to adsorb on, where they can react with electrons and protons to form products like CO, methane, methanol and multi-carbon hydrocarbons. In addition to the working electrode and the counter electrode, a reference electrode is necessary to be able to study the potentials of the working and counter electrodes separately.

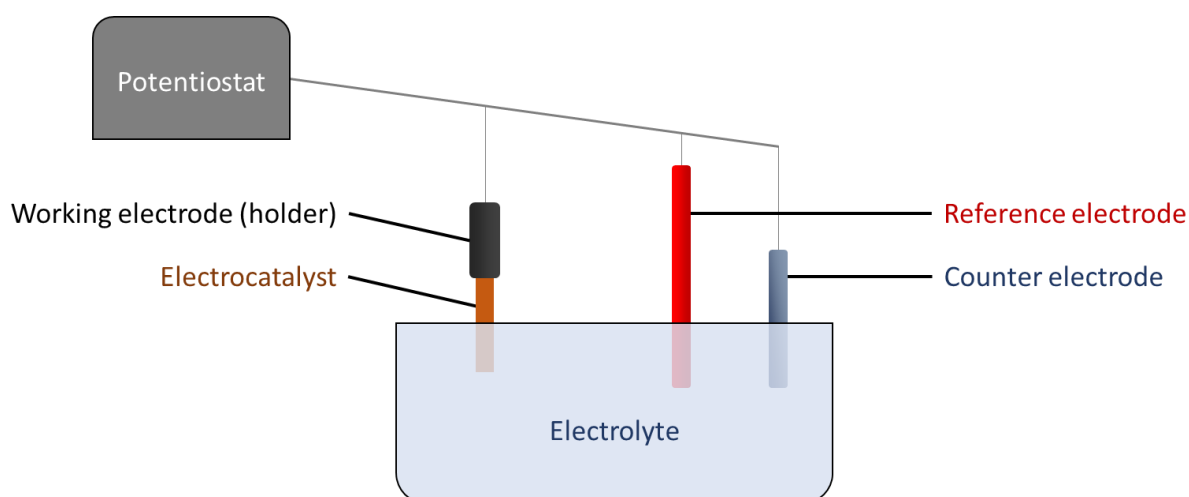


Figure 2. Simplified scheme of an electrochemical setup. When a cathodic bias (negative potential and current) is used, CO<sub>2</sub> reduction can happen on the surface of a suitable electrocatalyst (such as copper). Note that the electronic connections to the potentiostat are more complicated than depicted here.

Because the reference electrode potential is stable and well-known, its use greatly improves the reproducibility of electrochemical measurements and also makes for easy comparison between different publications. Additionally, the reaction within the reference electrode is kinetically very fast, so high currents can easily be passed through while maintaining high efficiency of the redox reaction. Using this, the potential for the other half-cell (working electrode + counter electrode) can accurately be determined.

With accurate potential and current measurements, it is possible to document which products are formed at which potentials. Certain electroreduction reactions use more electrons (Table 2) and have more steps in their reaction pathways, which is why they need a stronger reducing potential to make the reaction occur. Additionally, as is generally the case in ordinary chemical reactions, there is a certain activation energy barrier to overcome. This barrier comes from the substantial energy it costs to break the carbon-oxygen bonds, before energy is gained by forming new bonds in the products. As

a consequence, the thermodynamically ideal potential at which a reaction should proceed is usually not sufficient. This means that a stronger reducing potential is required (known as overpotential), consuming more energy than necessary, which results in a decrease in efficiency and also impacts the selectivity of the reaction. As the selectivity is defined as the part of the electrons used that experimentally ends up going to the desired product compared to the ideal situation where all electrons go to the product, it follows that selectivity towards desired products also decreases with overpotential.

### 2.1.2 Electrochemical equations: Faradaic efficiency and Nernst equation

In electrochemistry, the use of electrons to certain products is called the Faradaic efficiency (Equation 1):

$$\text{Faradaic efficiency} = \frac{I_{\text{Experimental}}}{I_{\text{Theoretical}}} \times 100\% \quad (1)$$

where  $I_{\text{Experimental}}$  is the current that ends up going to the product and  $I_{\text{Theoretical}}$  is the total current. Another way of calculating the Faradaic efficiency is formulated in Equation 2:

$$\text{Faradaic efficiency} = \frac{z \times n \times F}{Q} \times 100\% \quad (2)$$

where  $z$  is the number of electrons required for the product,  $n$  is the number of moles of product formed,  $F$  is the Faraday constant and  $Q$  is the charge passed through during electrolysis<sup>20</sup>. The Faradaic efficiency is used to get an indication of the efficiency of a reaction towards a specific product.

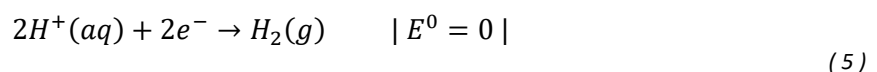
Another relevant formula is the Nernst equation, which describes the relation between reaction potential, electrolyte concentrations, temperature and the standard electrode potential. It can be used for determining minimal potentials for electrolysis reactions, but it is also useful for calculating the pH of electrochemical systems. The equation is given in Equation 3:

$$E = E^0 - \frac{RT}{nF} \ln(Q) \quad (3)$$

where  $E$  is the reaction potential,  $E^0$  is the standard reaction potential (potential where  $H_2$  is converted to  $H^+$  at standard conditions and is the value that is often given in half reaction tables),  $R$  is the universal gas constant,  $T$  is the temperature in Kelvin,  $n$  is the number of electrons transferred in the reaction,  $F$  is the Faraday constant and  $Q$  is the reaction quotient. When the reaction occurs at 298 K and  $\ln(Q)$  is changed to  $\log(Q)$ , the formula can be simplified to Equation 4:

$$E = E^0 - \frac{0.059}{n} \log(Q) \quad (4)$$

When  $H^+$  is involved in the reaction, the equation can be simplified even more, and it can be used to determine the pH. For example, in the hydrogen evolution reaction (Equation 5):



the reaction quotient is equal to (Equation 6):

$$Q = \frac{P_{H_2}}{[H^+]^2} \quad (6)$$

and the number of electrons  $n$  is 2, so at atmospheric pressure, Equation 6 reduces to Equation 7:

$$E = 0 - \frac{0.0591}{2} \log \frac{1}{[H^+]^2} \quad (7)$$

which can be written as Equation 8:

$$E = -\frac{0.0591}{2} \times -2 \log(H^+) = \mathbf{0.0591} \times \mathbf{pH} \quad (8)$$

This way, provided that the number of electrons and protons is equal, the pH can be determined when the electrode potential is known, and vice versa. Additionally, the Nernst equation is useful for the conversion between reference electrode and the standard hydrogen electrode potentials. For example, when a silver chloride reference electrode is used, we can fill in  $E^0 = 0.197$  V in Equation 4, leading to Equation 9:

$$E \text{ (vs. RHE)} = 0.197 \text{ V} - \frac{0.059}{n} \log(Q) \quad (9)$$

Similar to the previous steps, this equation can be simplified when the number of electrons and protons is the same, which eventually leads to Equation 10:

$$E \text{ (vs. RHE)} = 0.197 \text{ V} + 0.0591 \times \text{pH} \quad (10)$$

### 2.1.3 Electrochemical experiments: cyclic voltammetry and chronoamperometry

Some common methods of doing electrochemical measurements include chronoamperometry and cyclic voltammetry (CV).

Chronoamperometry works by applying a predetermined potential for a certain amount of time and simultaneously measuring the current flowing through the cell. Additionally, the potential can be stepped to see the difference in current at select potentials (Figure 3a). The result is a graph where time is on the x-axis and current is on the y-axis (Figure 3a). Integration of the graph results in the total charge that is transferred.

In cyclic voltammetry, potential is swept and the resulting current is measured. The potential can vary from reductive (negative) to oxidative (positive) biases and repeats for several cycles (Figure 3c). This method can be used to see the effects that different potentials have on the electrochemical environment, and the repetitive nature of CV ensures reproducible results. Additionally, cyclic voltammetry diagrams show oxidation and reduction points of the metal electrode, and for the CO<sub>2</sub> reduction reaction specifically, they also indicate the potential regions where the reduction takes place. This is due to the fact that currents are induced (and peaks arise) when oxidation or reduction processes are initiated, which is also illustrated in Figure 3d.

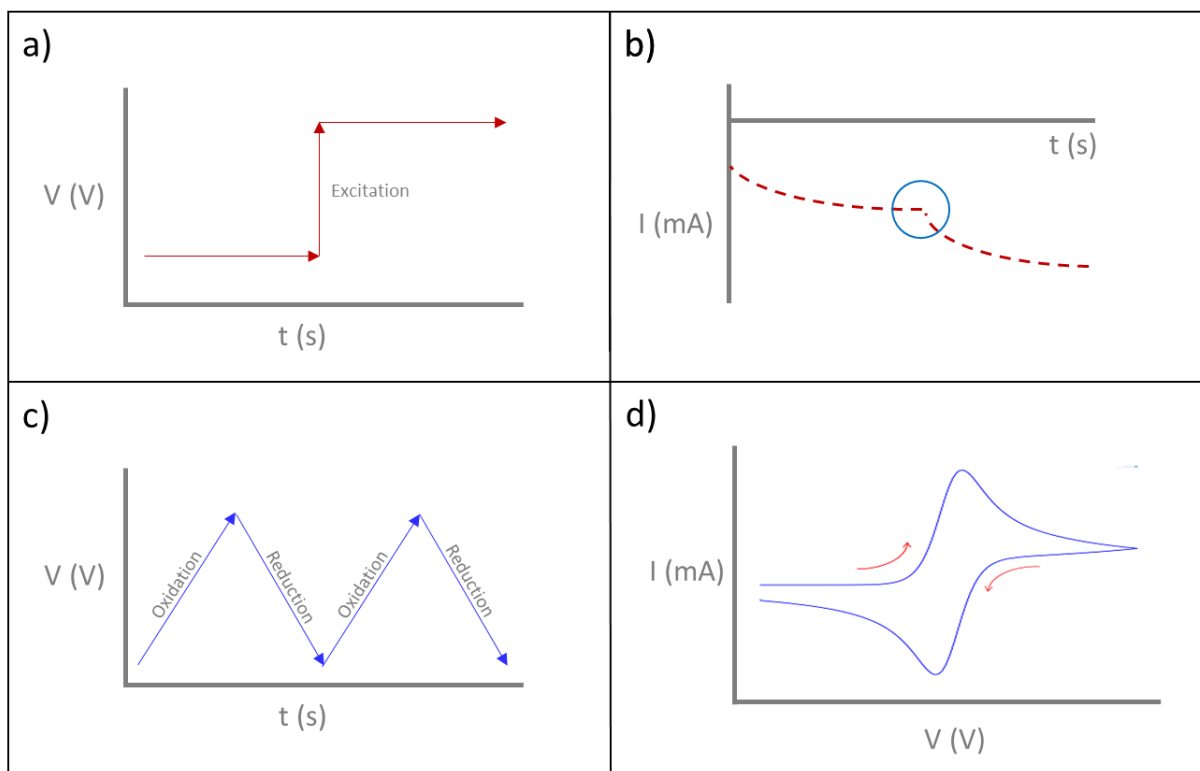


Figure 3. Simplified schemes of electrochemical methods: a) Chronoamperometry, potential development with time. The sudden increase is an excitation wave. b) Chronoamperometry, current development with time. The blue circle indicates the point of the excitation wave. c) Cyclic voltammetry potential development with time. Two cycles are illustrated here. d) Cyclic voltammetry current development with potential. Only one cycle is illustrated in this figure; one oxidation and one reduction.

#### 2.1.4 CO<sub>2</sub> reduction

The electroreduction reaction of CO<sub>2</sub> most often leads to the formation of carbon monoxide or formate, as they are 2-electron products<sup>6, 14, 21</sup>. When it comes to the production of hydrocarbon fuels, such as gasoline or diesel, these products are generally undesirable<sup>6</sup>. A solution is to mix the formed CO with hydrogen to form syngas and use the Fischer-Tropsch reaction to synthesize hydrocarbons<sup>22</sup>. A more direct approach, however, is to use electrocatalysts with high selectivity towards C<sub>2+</sub> products, such as copper, to ensure the formation of desired products<sup>23</sup>. As visible in Table 2, there is an abundance of CO<sub>2</sub> reduction reactions, using different amounts of electrons, different reactants and producing a variety of products. Note that the reactions are given for acidic electrolytes, but reduction reactions are also possible in neutral pH solutions (see Table 1). The values for E<sup>0</sup> indicate the thermodynamically ideal potentials that are necessary for the reactions to occur, but in practice, stronger potentials are usually required (overpotential). This is partly because of the activation energies that have to be overcome for several different steps in the reaction pathways, and decreases the efficiency.

Table 2. Several electrochemical reactions in acidic electrolyte (reproduced from ref<sup>23</sup>)

Reaction	$E^0$ /[V vs RHE]	(Product) Name, abbreviation
$2\text{H}_2\text{O} \rightarrow \text{O}_2 + 4\text{H}^+ + 4\text{e}^-$	1.23	Oxygen Evolution Reaction, OER
$2\text{H}^+ + 2\text{e}^- \rightarrow \text{H}_2$	0	Hydrogen Evolution Reaction, HER
$x\text{CO}_2 + n\text{H}^+ + ne^- \rightarrow \text{product} + y\text{H}_2\text{O}$		$\text{CO}_2$ Reduction, $\text{CO}_2\text{R}$
$\text{CO}_2 + 2\text{H}^+ + 2\text{e}^- \rightarrow \text{HCOOH}_{(\text{aq})}$	-0.12	Formic acid
$\text{CO}_2 + 2\text{H}^+ + 2\text{e}^- \rightarrow \text{CO}_{(\text{g})} + \text{H}_2\text{O}$	-0.10	Carbon monoxide
$\text{CO}_2 + 6\text{H}^+ + 6\text{e}^- \rightarrow \text{CH}_3\text{OH}_{(\text{aq})} + \text{H}_2\text{O}$	0.03	Methanol, MeOH
$\text{CO}_2 + 4\text{H}^+ + 4\text{e}^- \rightarrow \text{C}_{(\text{s})} + 2\text{H}_2\text{O}$	0.21	Graphite
$\text{CO}_2 + 8\text{H}^+ + 8\text{e}^- \rightarrow \text{CH}_{4(\text{g})} + 2\text{H}_2\text{O}$	0.17	Methane
$2\text{CO}_2 + 2\text{H}^+ + 2\text{e}^- \rightarrow (\text{COOH})_{2(\text{s})}$	-0.47	Oxalic acid
$2\text{CO}_2 + 8\text{H}^+ + 8\text{e}^- \rightarrow \text{CH}_3\text{COOH}_{(\text{aq})} + 2\text{H}_2\text{O}$	0.11	Acetic acid
$2\text{CO}_2 + 10\text{H}^+ + 10\text{e}^- \rightarrow \text{CH}_3\text{CHO}_{(\text{aq})} + 3\text{H}_2\text{O}$	0.06	Acetaldehyde
$2\text{CO}_2 + 12\text{H}^+ + 12\text{e}^- \rightarrow \text{C}_2\text{H}_5\text{OH}_{(\text{aq})} + 3\text{H}_2\text{O}$	0.09	Ethanol, EtOH
$2\text{CO}_2 + 12\text{H}^+ + 12\text{e}^- \rightarrow \text{C}_2\text{H}_4_{(\text{g})} + 4\text{H}_2\text{O}$	0.08	Ethylene
$2\text{CO}_2 + 14\text{H}^+ + 14\text{e}^- \rightarrow \text{C}_2\text{H}_6_{(\text{g})} + 4\text{H}_2\text{O}$	0.14	Ethane
$3\text{CO}_2 + 16\text{H}^+ + 16\text{e}^- \rightarrow \text{C}_2\text{H}_5\text{CHO}_{(\text{aq})} + 5\text{H}_2\text{O}$	0.09	Propionaldehyde
$3\text{CO}_2 + 18\text{H}^+ + 18\text{e}^- \rightarrow \text{C}_3\text{H}_7\text{OH}_{(\text{aq})} + 5\text{H}_2\text{O}$	0.10	Propanol, PrOH
$x\text{CO} + n\text{H}^+ + ne^- \rightarrow \text{product} + y\text{H}_2\text{O}$		$\text{CO}$ Reduction, $\text{COR}$
$\text{CO} + 6\text{H}^+ + 6\text{e}^- \rightarrow \text{CH}_{4(\text{g})} + \text{H}_2\text{O}$	0.26	Methane
$2\text{CO} + 8\text{H}^+ + 8\text{e}^- \rightarrow \text{CH}_3\text{CH}_2\text{OH}_{(\text{aq})} + \text{H}_2\text{O}$	0.19	Ethanol, EtOH
$2\text{CO} + 8\text{H}^+ + 8\text{e}^- \rightarrow \text{C}_2\text{H}_4_{(\text{g})} + 2\text{H}_2\text{O}$	0.17	Ethylene

The choice of electrocatalyst has a large influence on the selectivity towards certain products, and this can be used to control the  $\text{CO}_2$  reduction reaction. In the work of Y. Hori<sup>21</sup>, the main products of electrochemical  $\text{CO}_2$  reduction for several metal catalysts are collected and are shown in Table 3. It can be seen that copper is the only (pure) metal electrocatalyst that catalyzes  $\text{CO}_2$  reduction to a wide variety of carbon products. Therefore, many reaction pathways can occur for the  $\text{CO}_2$  reduction on a copper surface (Figure 4). Much research is ongoing to improve its selectivity and efficiency, in order to improve the ability to steer the electroreduction reaction to the desired products. In this work, copper is also the catalyst of choice, and we focus on determining the pH near the surface of the electrode. This will help get more insight into the selectivity of the  $\text{CO}_2$  reduction reaction on copper, as pH is believed to have an influence on the products that are formed<sup>11-13</sup>.

Table 3. Several metal electrocatalysts and their main product yield in the electrochemical  $\text{CO}_2$  reduction reaction. Table adapted from ref<sup>21</sup>.

Metal electrocatalyst	Main product(s)	Metal electrocatalyst	Main product(s)
<b>Pb</b>	$\text{HCOO}^-$	<b>Au</b>	CO
<b>Hg</b>	$\text{HCOO}^-$	<b>Ag</b>	CO
<b>Tl</b>	$\text{HCOO}^-$	<b>Zn</b>	CO, $\text{HCOO}^-$
<b>In</b>	$\text{HCOO}^-$	<b>Pd</b>	CO, $\text{HCOO}^-$
<b>Sn</b>	$\text{HCOO}^-$	<b>Ga</b>	CO
<b>Cd</b>	$\text{HCOO}^-$	<b>Cu</b>	$\text{CH}_4$ , $\text{C}_2\text{H}_4$ , $\text{C}_2\text{H}_5\text{OH}$ , $\text{HCOO}^-$

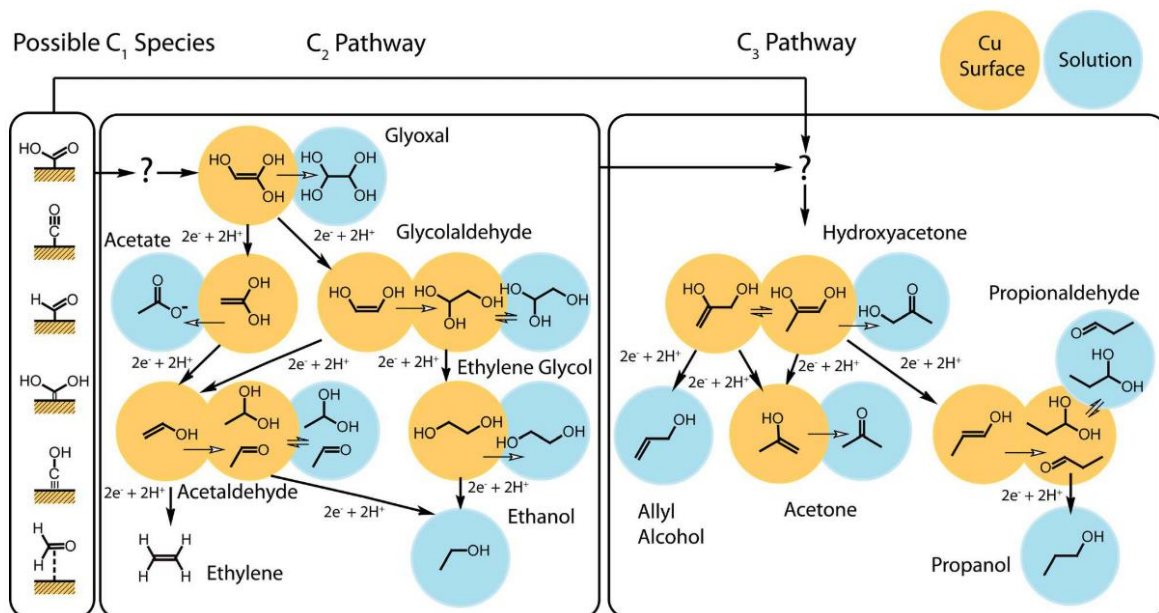
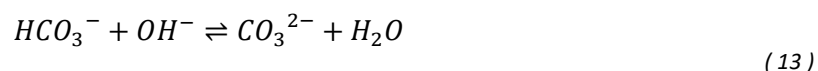
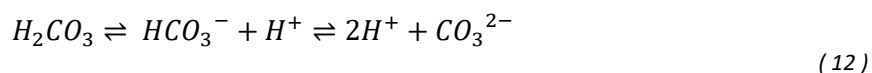


Figure 4. Reaction pathways for  $\text{CO}_2$  reduction on a copper electrode. Figure reproduced from ref <sup>6</sup>.

In addition to the pH having an effect on the selectivity of  $\text{CO}_2$  electroreduction, the electrolyte influences the formed products as well. A  $\text{CO}_2$ -saturated bicarbonate solution is often used, to ensure sufficient  $\text{CO}_2$  in the electrolyte. In Equation 11, the dissolution reaction of  $\text{CO}_2$  in water is given and in Equation 12, the equilibrium reactions of different carbonate species are shown. When using this electrolyte, the  $\text{HCO}_3^-$  has a buffering effect, which lowers the pH by reacting with the formed  $\text{OH}^-$  to  $\text{CO}_3^{2-}$  (Equation 13) and thereby influences the hydrogen evolution reaction as well as the pH-dependent  $\text{CO}_2$  reduction reactions, e.g. towards methane<sup>13,24</sup>. Consequently, a higher bicarbonate concentration in the electrolyte has a stronger buffering effect, lowering the local pH, which in turn influences the formed products. From the work by Valera *et al.*, it appeared that when using the  $\text{CO}_2$  reduction reaction conditions with optimal selectivity for ethylene (0.1 M  $\text{KHCO}_3$ , -1.1 V vs Ag/AgCl, 9 atm<sup>25</sup>), and only increasing the bicarbonate concentration in the electrolyte to 0.3 M, the main product became methane rather than ethylene<sup>26</sup>, as the reaction mechanism towards methane favors lower pH (Figure 5). This study shows that many pH-related environmental parameters can have an influence on  $\text{CO}_2$  reduction and indicates the relevance of studying the local pH during this reaction.



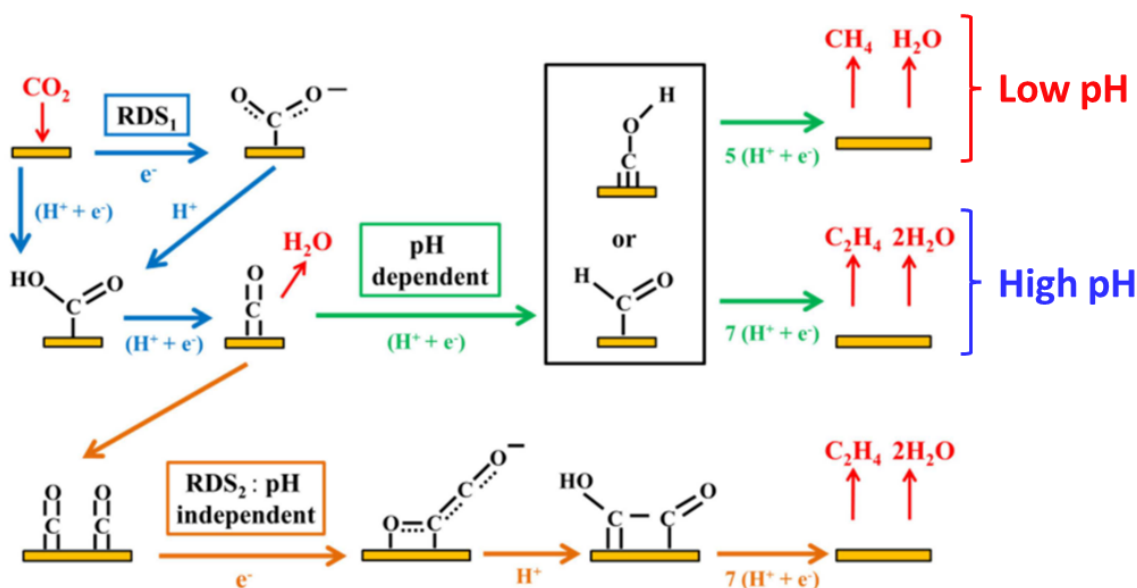


Figure 5. Possible pH-dependent and pH-independent reaction mechanisms of  $\text{CO}_2$  electroreduction. As methane formation only happens using protons, methane production is favored over ethylene at lower pH. Figure reproduced from ref <sup>13</sup>.

## 2.2 Raman spectroscopy

In general, Raman spectroscopy is a light-scattering spectroscopic technique that can give information based on the chemical structure in a target molecule. Light can be scattered in two ways: elastically, which is called Rayleigh scattering, or inelastically, called Raman scattering. The majority of light scatters elastically, which means that the outgoing light has the same wavelength as the incoming light and there is no net transfer of energy. However, a fraction of the light (approximately one millionth<sup>15</sup>) will scatter inelastically, which happens due to the interaction of the vibrational energy of the molecule with the photon energy, resulting in scattered light with a longer or shorter wavelength. When the scattered photons have a longer wavelength, and have therefore lost energy, the change in energy is called Stokes scattering or Stokes shift. When the scattered light has a shorter wavelength, it means that the photons have gained energy, which is referred to as the anti-Stokes shift. When comparing Raman spectroscopy to IR spectroscopy, a key difference is that their physical principles differ: for infrared spectroscopy, a photon is absorbed and excites a bond to a higher vibrational energy state. In Raman spectroscopy, the photon excites a bond to a virtual energy state, which means that the bond gains some energy, but is not excited to a quantized vibrational energy level. In Figure 6, their principles are depicted as well as the difference between Rayleigh, Stokes and anti-Stokes scattering.

Both Stokes and anti-Stokes shifts are used in Raman spectroscopy, but Stokes shift is more common than anti-Stokes shift. The reason for this is that anti-Stokes scattering can only occur when molecules are vibrationally excited prior to irradiation by the laser<sup>27</sup>. This also explains why the intensity of the anti-Stokes shift bands is usually much lower than the Stokes shift bands, as visible in Figure 7.

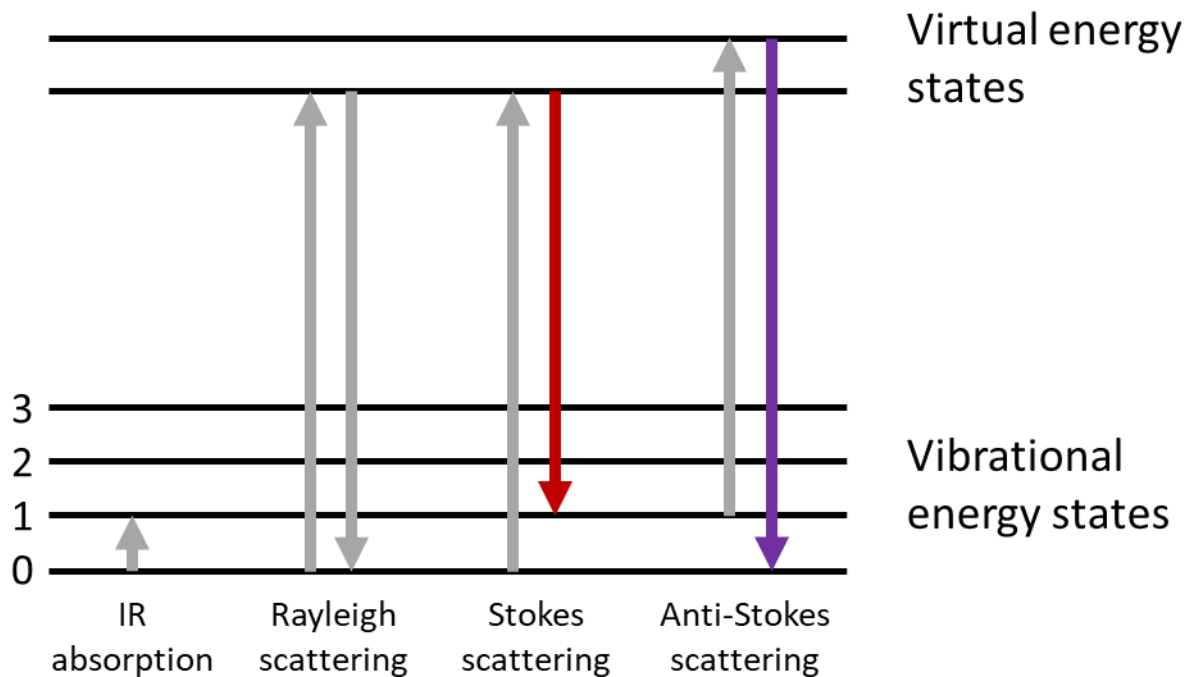


Figure 6. Principle of IR absorption and the different kinds of Raman scattering. It is visible that Stokes scattering causes the photon to gain energy from the vibrational energy, whereas the anti-Stokes scattering photon loses energy to the vibration. Scheme adapted from refs <sup>15,16</sup>.

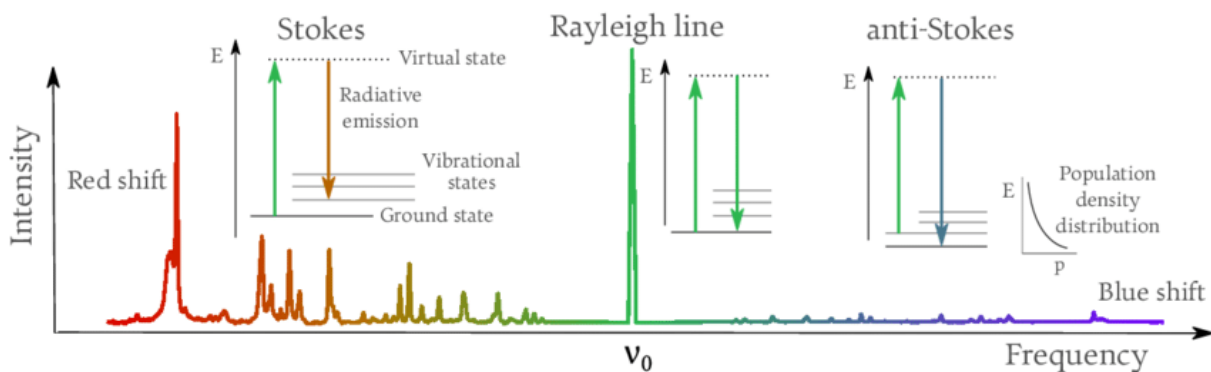


Figure 7. Example Raman spectrum indicating the difference between Stokes, Rayleigh and anti-Stokes lines. Figure reproduced from ref <sup>28</sup>.

Raman and IR spectroscopy differ in selection rules: in infrared spectroscopy, a vibration has to change the dipole moment of the molecule, whereas in Raman spectroscopy, a vibration has to induce a change in polarizability of the molecule in order to produce a signal. Polarizability can be understood as the likelihood of deformation of the electron cloud of a molecule. This means that generally, asymmetric vibrations are more IR-active, whereas symmetric vibrations are more Raman-active. The difference between changes in dipole moment and polarizability is illustrated in Figure 8.

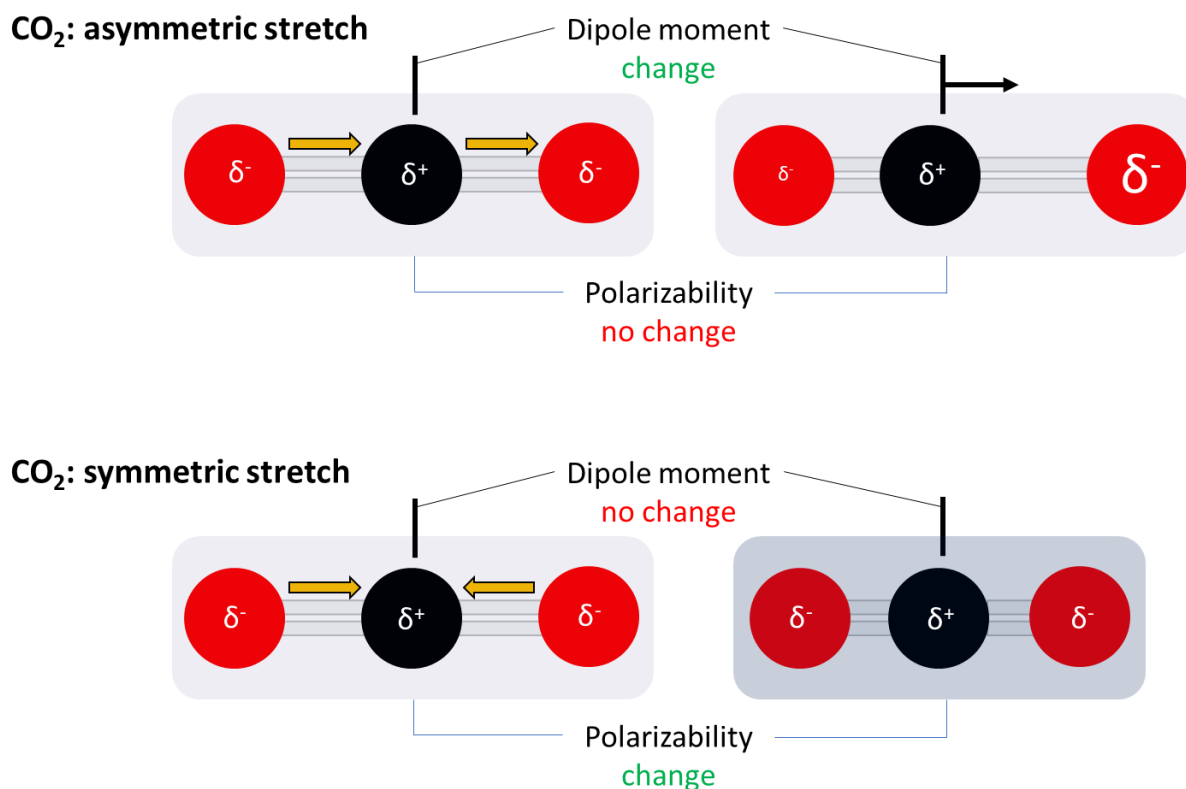


Figure 8. Simplified illustration of asymmetric stretching (IR-active) and symmetric stretching (Raman-active) vibrational modes of CO<sub>2</sub>. The main difference is the change of dipole moment and the change in the shape of the electron cloud (polarizability), respectively.

### 2.2.1 Surface-, Tip- and Shell-Isolated Nanoparticle-Enhanced Raman Spectroscopy

The weak inelastic scattering of molecules can make it challenging to obtain good Raman signals<sup>16</sup>. A solution for this is to use Raman signal enhancement techniques, such as Surface-Enhanced Raman Spectroscopy (SERS), Tip-Enhanced Raman Spectroscopy (TERS) or Shell-Isolated Nanoparticle-Enhanced Raman Spectroscopy (SHINERS). All of these enhancement techniques work by taking advantage of the same physical phenomenon, which is called localized surface plasmon resonance (LSPR)<sup>15</sup> and is induced by the excitation of localized surface plasmons in certain metallic nanostructures, such as gold or silver. Surface plasmons can be described as the coherent oscillations of delocalized electrons at the surface of a material, which become localized surface plasmons when confined in a metal nanoparticle that is smaller than the wavelength of the light used for irradiation<sup>29</sup>. The excitation happens when an external electric field matches the resonant frequency of the plasmons. As a consequence, a strong localized electromagnetic field is formed which in turn drastically enhances Raman signals in its vicinity<sup>15,16,18</sup>. This effect is even stronger in between two nanoparticles, which is referred to as a 'hot spot'.

In SERS, plasmon resonance is induced on a roughened surface (Figure 9a)<sup>15,16,30–36</sup>; in TERS, it is induced between an extremely thin tip and the underlying substrate (Figure 9b)<sup>15,16,37,38</sup>; and in SHINERS, the plasmon resonance is induced by two nanoparticles that are close together (Figure 9c)<sup>15,16,18</sup>. These techniques provide more applications for Raman spectroscopy, as signals can be enhanced up to 10<sup>11</sup> times<sup>15</sup>, significantly increasing its sensitivity for adsorbed molecules. In this work, we take advantage of both SERS and SHINERS to gain information about the events happening on the surface of a copper electrode during electroreduction of CO<sub>2</sub>.

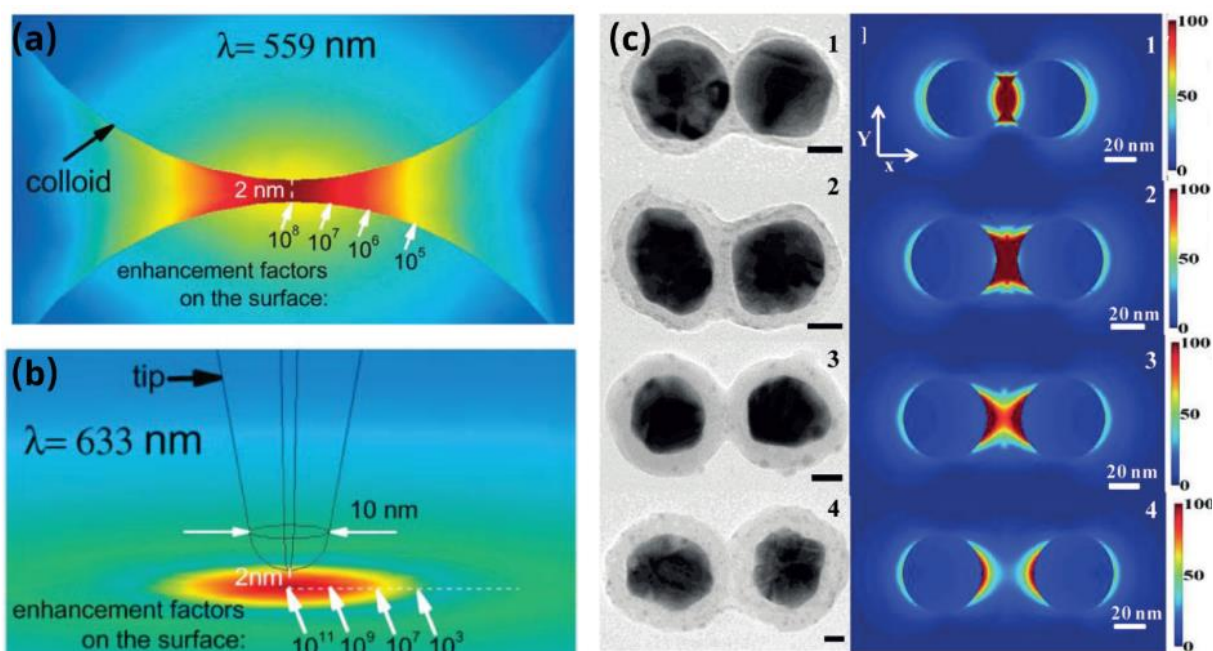


Figure 9. The enhancement factors for different uses of plasmon-enhanced Raman spectroscopy. a) Enhancement from dimer gold nanoparticles (SERS). b) Enhancement between a gold tip and gold surface (TERS). c) Enhancement between two silica-coated gold nanoparticles (SHINERS). Figure reproduced from ref<sup>15</sup>.

The application of SHINERS in this work takes advantage of LSPR between two silica-coated gold nanoparticles to enhance Raman signals, as used in the work of T. Hartman<sup>15</sup>. The reason for the silica coating is to increase the stability of the gold nanoparticles by decreasing the rate of aggregation, which in turn increases shelf time. In the TEM image in Figure 9c, silica-coated gold nanoparticles are visible with increasing shell thickness from top to bottom. To the right of the TEM image, it can be seen that the shell thickness has a significant effect on the size and strength of the hotspot, where generally, a thinner shell causes stronger enhancement. This means that there is a balance between nanoparticle stability and Raman signal enhancement, which should be taken into account for application in this work.

### 2.2.2 SERS and SHINERS in electrochemical systems

The introduction of an applied potential in enhanced Raman spectroscopy causes several effects that cannot be neglected. Raman spectra taken on surfaces with an external electric field present often feature peak intensity changes and wavenumber shifts. This is because of several factors that are at play when combining an electronic potential with vibrational spectroscopy.

One example is the work of Ray and Anderson<sup>39</sup>, where they describe the characteristics of CO chemisorption on a platinum electrode and the influence of the applied (external) electric field (Figure 10). Using the Dewar-Chatt-Duncanson model, they explain that chemisorption of CO on a Pt surface is characterized by a donating  $5\sigma$  orbital and an accepting  $2\pi^*$  orbital (both from the carbon monoxide). This means that when an anodic (positive) potential is applied, the back-donation from the Pt 4d-orbital decreases as the s-d valence band increases to higher binding energy, causing less overlap with the  $\pi^*$  orbital (which is bonding for Pt-C) and consequently weakening the Pt-C bond. On the other hand, the  $5\sigma$  orbital increases its electron donation to the platinum, which strengthens the Pt-C bond. However, as the decrease in  $\pi$ -d overlap is more significant than the increase in  $\sigma$ -donation, the Pt-C bond becomes weaker. This in turn decreases the vibrational energy and causes the bond to absorb at lower frequencies in a Raman spectrum. The effects regarding the C-O bond are exactly opposite, as the  $\pi^*$  orbital is anti-bonding for C-O. Less overlap with an anti-bonding orbital causes an

increase in bond strength, which is characterized by Raman signals at higher energies. Subsequently, the Raman spectrum looks different, as characteristic peaks are shifted to higher (C-O) or lower (Pt-C) energies. This effect shows that electrochemical potentials can have significant influence on enhanced Raman spectroscopy and should be taken into account for the measurements.

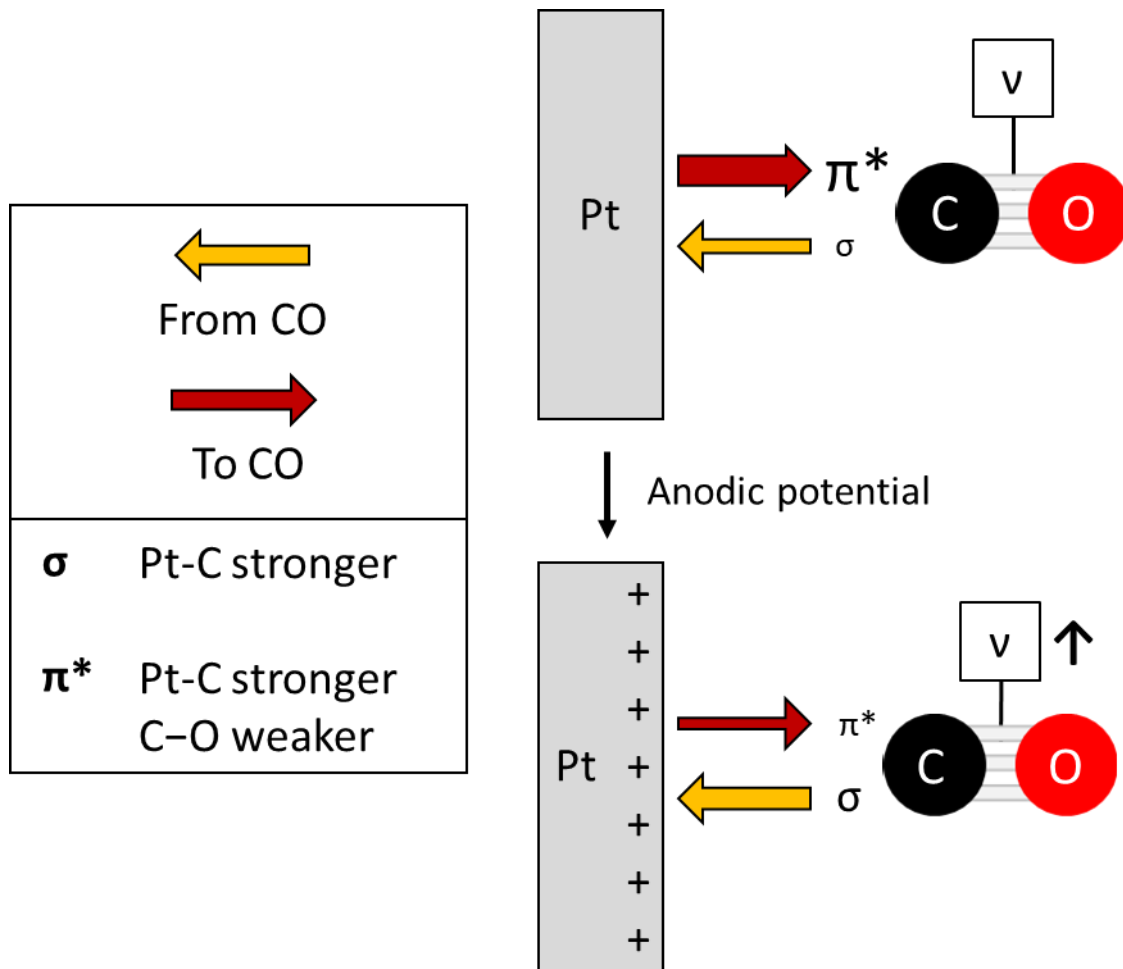


Figure 10. CO-adsorption on a Pt electrode. When an anodic potential is applied, the Pt-C bond decreases in bond strength and the C-O bond strengthens, causing Raman signals at higher wavenumbers.

## 2.3 pH probing methods

A widely used method of pH measuring is by using pH electrodes. They work by measuring the activity of a certain ion in solution and subsequently translating that to an electrical potential. As this potential is directly dependent on pH by the Nernst equation, the pH can be determined<sup>40</sup>. Note that the activity is not exactly the same as the concentration, which might cause deviating results.

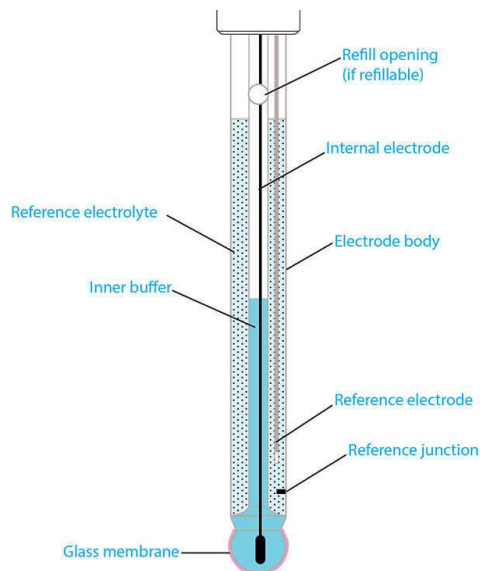


Figure 11. Structure of a typical pH electrode. Figure reproduced from ref<sup>40</sup>.

Additionally, for some *in situ* measurements, pH electrodes have limited applicability. For example, in this work we intend to track the local pH on a metal surface, where a pH electrode would only be able to measure the bulk pH. Alternative methods include spectroscopy-based pH sensors, such as luminescent pH probes or Raman reporter based probes. An example of a photoluminescence-based pH-dependent molecule is fluorescein, which undergoes changes to its fluorescence intensity based on its protonation (Figure 12). In the work of Wirnsberger *et al.*<sup>41</sup>, a mesoporous silica film is doped with fluorescein to form a pH sensor. In Figure 13a, the difference in spectrum for the probe at different pH is visible, and in Figure 13b the pH calibration curve is depicted.

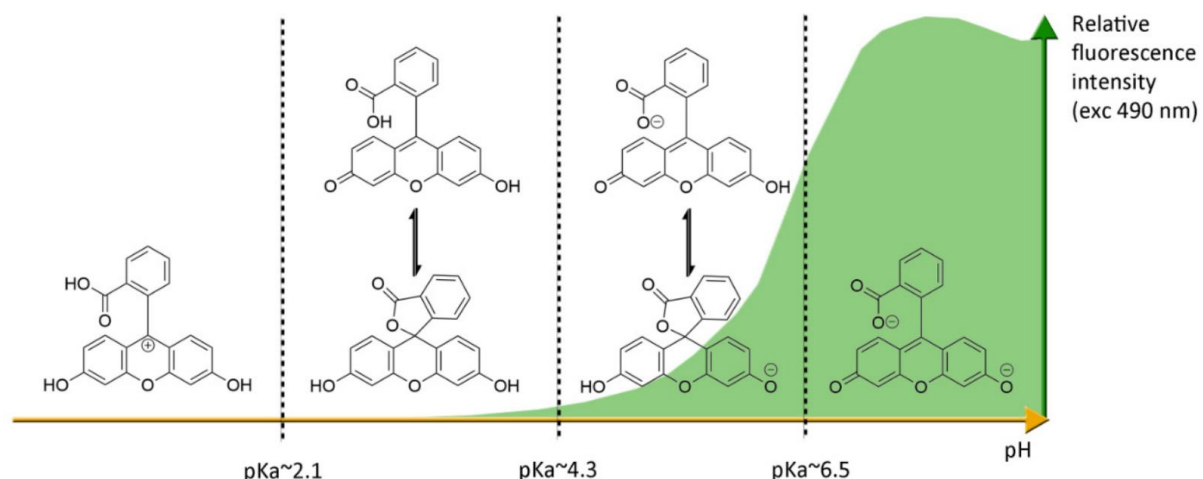


Figure 12. Fluorescein protonation changes that cause the fluorescence intensity dependency on pH. Figure reproduced from ref<sup>42</sup>.

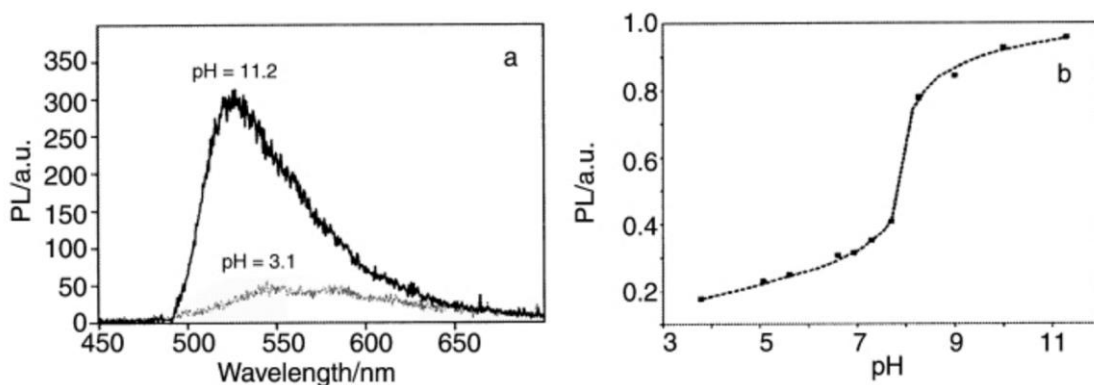


Figure 13. The results of the fluorescein-doped mesoporous silica pH sensor by Wirnsberger *et al.* a) Photoluminescence spectra of a at acidic and basic pH. b) Calibration curve relating photoluminescence intensity to pH. Figure reproduced from ref<sup>41</sup>.

As visible in the calibration curve, the sensitivity of the probe is best around pH 7-8.5, because the photoluminescence intensity undergoes the most changes around these values. The reason for sensitivity can be explained using the  $pK_a$  values of fluorescein. The  $pK_a$  of a functional group (such as a carboxylic acid) indicates the pH at which 50% of that group is protonated. This means that when the pH is around the  $pK_a$ , small deviations in pH cause substantial changes in protonation, because pH is a logarithmic scale. At low pH all groups are protonated. When the pH is then increased, slow deprotonation occurs until it reaches the  $pK_a$ , where rapid deprotonation happens. Increasing the pH further then causes slow deprotonation of the remaining groups, which results in the S shaped curve visible in Figure 13b (similar to a titration curve). For local pH measuring in electrochemical systems, this mesoporous silica-based method is not really suitable, as the used silica has a thickness of around 1  $\mu\text{m}$ . This means that the measured pH is not on the surface, which is the goal of our research. Additionally, the sensitivity is not suitable either, as we need to be able to measure between pH 7 and 12 for the  $\text{CO}_2$  reduction reaction.

Another example of a spectroscopy-based pH probe uses Raman spectroscopy, and works similar to the above described method. In the work of Scarpitti *et al.*<sup>19</sup>, they describe a probe using 4-mercaptobenzoic acid (4-MBA, inset Figure 14a) as pH-sensitive Raman reporter for pH determination in live cells. There are several reasons why 4-MBA is suitable as a pH probe. The thiol group can easily and stably bind to gold nanoparticles, which makes it detectable in Raman spectroscopy. Furthermore, the carboxylic acid group will act as pH probe, as protonation and deprotonation of the acid group cause visible (and reversible) changes in the Raman spectrum (Figure 14a, c, d). This way, a calibration curve can be experimentally determined, where either relative peak intensity or peak shift are plotted against pH (which is the working principle of the probe). Finally, the aromatic ring featured in the pH probe provides an internal standard for the Raman spectra to be normalized to, as ring vibrations give rise to the most intense peaks (Figure 14b). Similar to the fluorescein probe, the 4-MBA probe is most sensitive around the  $pK_a$  of the carboxylic acid group.

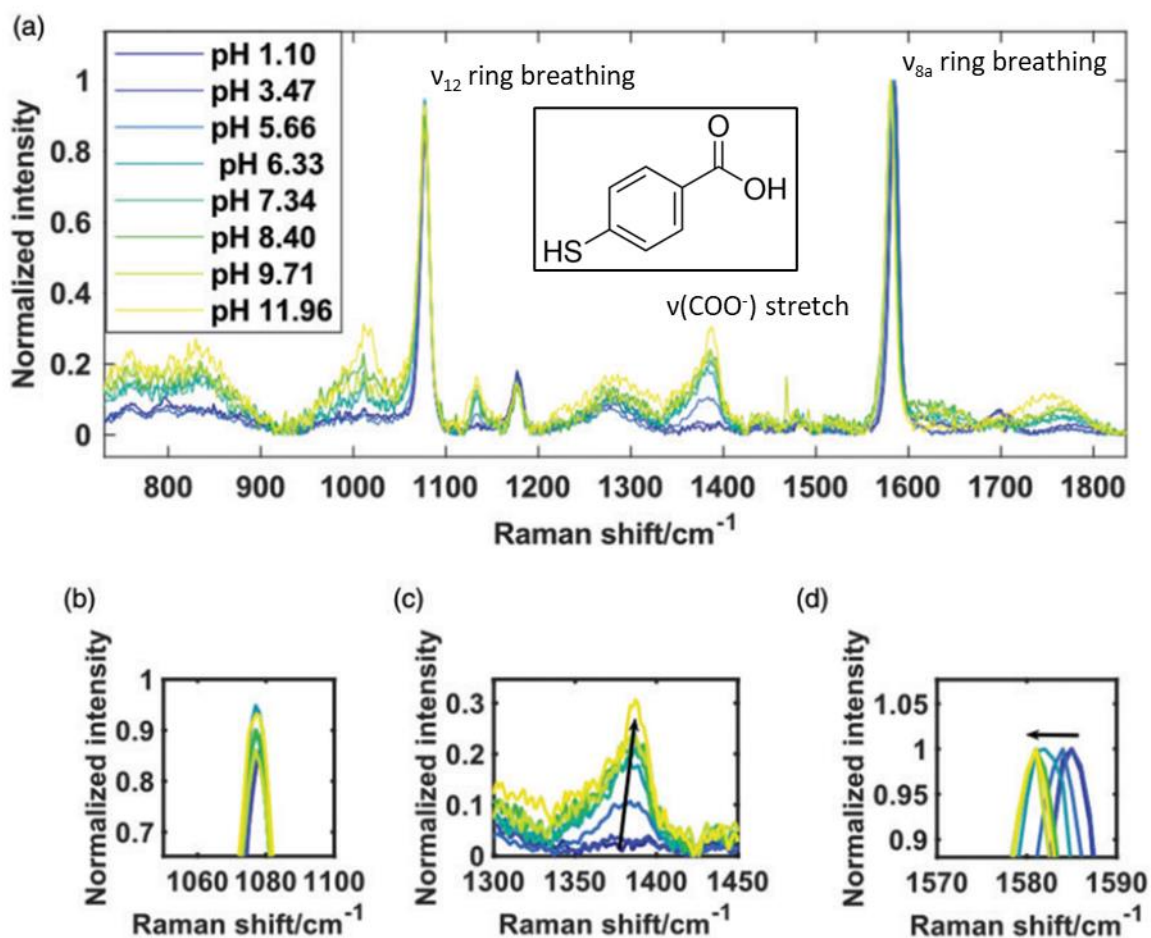


Figure 14. pH-dependent trends observed in the Raman spectra for the 4-MBA probe. a) All Raman spectra at indicated pH. The most relevant vibrational modes are indicated and inset figure is the structure of 4-mercaptobenzoic acid. b) The 1080 cm<sup>-1</sup> peak (ring breathing vibration) does not show dependency on pH, and is used for normalization. c) Increase in intensity with pH for the COO<sup>-</sup> symmetric stretching vibration at 1380 cm<sup>-1</sup>. d) The 1580 cm<sup>-1</sup> peak (ring stretching vibration) redshifts with increasing pH. Figure reproduced from ref<sup>19</sup>.

## 3 Methods

### 3.1 Chemicals

Trisodium citrate dihydrate ( $\text{Na}_3\text{Cit}\cdot 2\text{H}_2\text{O}$ , 99%) was purchased from Acros Organics.

Copper foil (Cu, purity: 99.9999%, puratonic), potassium hydroxide pellets (KOH, 85%), gold chloride trihydrate ( $\text{HAuCl}_4\cdot 3\text{H}_2\text{O}$ , 99.99% metals basis), 4-mercaptophenol (4-MP, 97%) were purchased from Alfa Aesar.

Potassium phosphate ( $\text{K}_3\text{PO}_4$ ,  $\text{K}_2\text{HPO}_4$  and  $\text{KH}_2\text{PO}_4$ ), pyridine anhydrous (Py, >99.98%) were purchased from Fisher.

Potassium bicarbonate ( $\text{KHCO}_3$ , purity >99.7%) was purchased from Fluka.

Carbon dioxide gas ( $\text{CO}_2$ , purity: 99.995%) was purchased from Linde Gas.

Hydrochloric acid (HCl, 37%) was purchased from Merck.

4-mercaptobenzoic acid (4-MBA, 99%), tetraethyl orthosilicate (TEOS, >99.0%), (3-aminopropyl)trimethoxysilane (APTMS, 97%), sodium silicate ( $\text{Na}_{2x}\text{Si}_y\text{O}_{2y+x}$ , 27%  $\text{SiO}_2$  in 14% NaOH), hydroxylamine hydrochloride ( $\text{NH}_2\text{OH}\cdot\text{HCl}$ , >98%), rhodamine 6G (Rh6G) were purchased from Sigma-Aldrich.

Ethanol absolute (EtOH, 99.9%), ammonia solution ( $\text{NH}_3$ , 28-30%), sulfuric acid ( $\text{H}_2\text{SO}_4$ , AnalaR NORMAPUR<sup>®</sup> analytical reagent, 95~97%) were purchased from VWR Chemicals.

### 3.2 Nanoparticle synthesis

Gold nanoparticles were prepared by colloidal growth induced by dropwise addition of gold precursor ( $\text{HAuCl}_4$ ) and reducing agent ( $\text{NH}_2\text{OH}\cdot\text{HCl}$ ) to gold nanoseeds synthesized by the Turkevich method.<sup>43</sup>

#### *Preparation of gold seeds*

30 mL of mQ  $\text{H}_2\text{O}$  (resistivity@298K > 18.2 M $\Omega$ cm) was heated to 100°C in an aqua regia cleaned round bottom flask while stirring vigorously. 300  $\mu\text{l}$  of 1 wt.% (W/V)  $\text{HAuCl}_4$  aqueous solution and 1 mL 1 wt.% (W/V) trisodium citrate aqueous solution were added. The mixture was stirred and heated for 15 minutes after which the color had changed from faint yellow to red, indicating successful gold seed formation.<sup>43</sup>

#### *Gold nanoparticle growth*

1 mL of as-prepared gold seeds were added to 112 mL mQ  $\text{H}_2\text{O}$  in a 250 mL round bottom flask, to which 2 mL of 1 wt.% trisodium citrate was added while stirring. To go from gold seeds to nanoparticles of around 80 nm, 1.6 mL of 10 mM  $\text{NH}_2\text{OH}\cdot\text{HCl}$  solution and 2 mL 0.5 wt.%  $\text{HAuCl}_4$  solution were carefully added dropwise over 30 minutes.<sup>18</sup>

#### *Silica coating using APTMS or MPTES*

0.2 mL of a 1 mM aqueous (3-aminopropyl)trimethoxysilane (APTMS) or (3-mercaptopropyl)trimethoxysilane solution was added to 15 mL as-prepared gold nanoparticles and the mixture was stirred for 15 minutes. Then, 1.6 mL of a 0.5 wt.% aqueous sodium silicate solution (acidified by adding 0.85 mL 1M HCl to the volumetric flask prior to filling it with  $\text{H}_2\text{O}$ ) was added and heated to 80°C. When 80°C was reached, the mixture was left stirring for 25 minutes after which it was force-cooled in a cold-water bath. The nanoparticles were then centrifuged and washed 3 times in mQ  $\text{H}_2\text{O}$  and eventually resuspended in 5 mL mQ  $\text{H}_2\text{O}$ .<sup>44</sup>

#### *4-MBA functionalization and TEOS coating of gold nanoparticles*

15  $\mu\text{L}$  of a 1 mM 4-mercaptobenzoic acid (4-MBA) in ethanol solution was added to 10 mL of as-prepared gold nanoparticles and the mixture was left stirring at 800 RPM for 30 minutes. The particles were then centrifuged and redispersed in 10 mL 1:3 (V/V) mQ  $\text{H}_2\text{O}$ :ethanol solution after which 280  $\mu\text{L}$  of 28% aqueous ammonia solution was added. Using a syringe pump, 30  $\mu\text{L}$  of TEOS was then added over 2 hours, while continuously stirring. After all was added, the mixture was centrifuged and washed twice in 3 mL mQ  $\text{H}_2\text{O}$  and finally resuspended in 2 mL mQ  $\text{H}_2\text{O}$ .<sup>34</sup>

#### *4-MP functionalization and TEOS coating of gold nanoparticles*

20  $\mu\text{L}$  of 28% ammonia solution was added to 10 mL of as-prepared gold nanoparticles to increase the pH to 8.5. Then, 10  $\mu\text{L}$  of a 1 mM aqueous 4-mercaptophenol (4-MP) solution was added and the mixture was sonicated for 10 minutes. The particles were then mildly centrifuged (3500 RPM, 3 minutes) and redispersed in 10 mL 1:3 mQ  $\text{H}_2\text{O}$ : ethanol solution. Subsequently, 100  $\mu\text{L}$  28-30% ammonia solution was added before 30  $\mu\text{L}$  TEOS was added over 2 hours using a syringe pump, while continuously stirring. The sample was then centrifuged and washed twice in 3 mL mQ and finally resuspended in 1 mL mQ. This synthesis was based on Au-MBA@ $\text{SiO}_2$  synthesis in ref<sup>34</sup>.

### 3.3 Characterization and experimental procedures of pH probes

Potassium phosphate buffer solutions were used for pH calibration curve determination and were prepared by dissolving  $\text{K}_3\text{PO}_4$ ,  $\text{K}_2\text{HPO}_4$  and  $\text{KH}_2\text{PO}_4$  in certain ratios to prepare 0.1M phosphate solutions with different pH (Table 4). For sample 10, addition of 1 mL of 1M KOH was necessary to sufficiently increase the pH. For pH 0 and pH 14 measurements, 1M HCl and 1M KOH were used, respectively. Prior to use in calibration curve measurements, the pH was measured again for each sample to guarantee accurate results.

Table 4. Potassium phosphate buffer solution preparation.

Sample	Initial pH	$\text{KH}_2\text{PO}_4$ (mg)	$\text{K}_2\text{HPO}_4$ (mg)	$\text{K}_3\text{PO}_4$ (mg)	mQ $\text{H}_2\text{O}$ (mL)
1	4.58	147	0	0	10.8
2	6.06	123	24	0	10.4
3	7.00	73	118	0	12.1
4	8.04	10	173	0	10.7
5	9.27	0	175	0	10.1
6	10.33	0	178	9	10.4
7	11.32	0	161	76	12.8
8	12.05	0	43	172	10.6
9	12.31	0	0	212	9.91
10	12.90	0	0	234	10 (+1 mL 1M KOH)

Transmission Electron Microscopy images were collected using a Tecnai20F electron microscope with an operating voltage of 200 kV.

Raman spectra were collected using a *Renishaw InVia Microscope* or a *Horiba Raman spectrometer* with a 785 nm laser. For all Raman spectra, the calibration was performed on a silica wafer. For time-resolved measurements we measure with a Nikon N40X-NIR water-dipping objective at 10% laser power. A pyridine-pinhole test was used to check silica coating quality, and is performed by dropcasting 10  $\mu\text{L}$  of a 1 mM pyridine solution onto dried nanoparticles and measuring the Raman spectrum to see whether pyridine peaks are present. To check for enhancement for the nanoparticles without a functionalized probe molecule, a rhodamine-6G solution was used. For the final probes this was unnecessary, as the probe molecule itself can indicate whether enhancement is sufficiently strong.

All electrochemical experiments were performed in a CO<sub>2</sub> saturated 0.1 M KHCO<sub>3</sub> solution (pH=6.8), using an aqua regia-cleaned petri dish. Solutions were saturated with CO<sub>2</sub> either by bubbling while stirring for at least 1 hour or by exposure of the solution to a CO<sub>2</sub> rich atmosphere and subsequent homogenization. CO<sub>2</sub> saturation was verified by pH measurements. A Pt mesh was used as a counter electrode and a leakless Ag/AgCl reference electrode (eDAQ) was used as a reference. The potential was converted to RHE using the following formula:

$$E(\text{vs. RHE}) = E(\text{vs. Ag/AgCl}) + 0.197 \text{ V} + 0.0591 * \text{pH}$$

Cyclic voltammetry measurements were performed using a Ivium compactstat.h10800 potentiostat. The cycles started at 0.55 V<sub>RHE</sub> and ranged between +1.05 to -0.85 V<sub>RHE</sub> using 10 mV step size and a scan rate of 10 mVs<sup>-1</sup>.

The copper plates used as electrodes in the electrochemical procedures were approximately 30x5x0.1 mm in size. Prior to use, they were sonicated for three minutes in a 1M HNO<sub>3</sub> solution and rinsed in mQ H<sub>2</sub>O. For plated (electrodeposited) copper, an acidic CuSO<sub>4</sub> solution was used and a current of -0.5 mA was applied for 30 seconds to acquire the desired plating, after which the electrode was briefly washed in mQ H<sub>2</sub>O again to remove leftover copper sulfate solution. The acidic CuSO<sub>4</sub> solution was prepared by dissolving 5 grams of CuSO<sub>4</sub> · 5 H<sub>2</sub>O in 90 mL MQ H<sub>2</sub>O and 10 mL concentrated H<sub>2</sub>SO<sub>4</sub> was added.

## 4 Results and discussion

### 4.1 Preparation of Au-MBA@SiO<sub>2</sub> and Au-MP@SiO<sub>2</sub> pH probes

The general approach in preparing the pH probes is based on a bottom-up synthesis, which is illustrated in Figure 15. We first established a solid SHIN procedure based on the work by T. Hartman<sup>15</sup>. The first step was the synthesis of gold nanoparticles. In Figure 16, TEM images show the shape and size of these particles, and it can be seen that the size of the particles is approximately 90 nm. AuNP synthesis was successful, showing homogeneously shaped particles (Figure 16a, b).

To improve the stability of the nanoparticles, the next step was to coat the particles with a thin layer of silica, to create the shell-isolated nanoparticles (SHINs) necessary for SHINERS. As described in the previous chapter, this was done by using slow sodium silicate hydrolysis, forming a silica layer around the AuNPs by first functionalizing them with the linker molecule (3-aminopropyl)triethoxysilane.

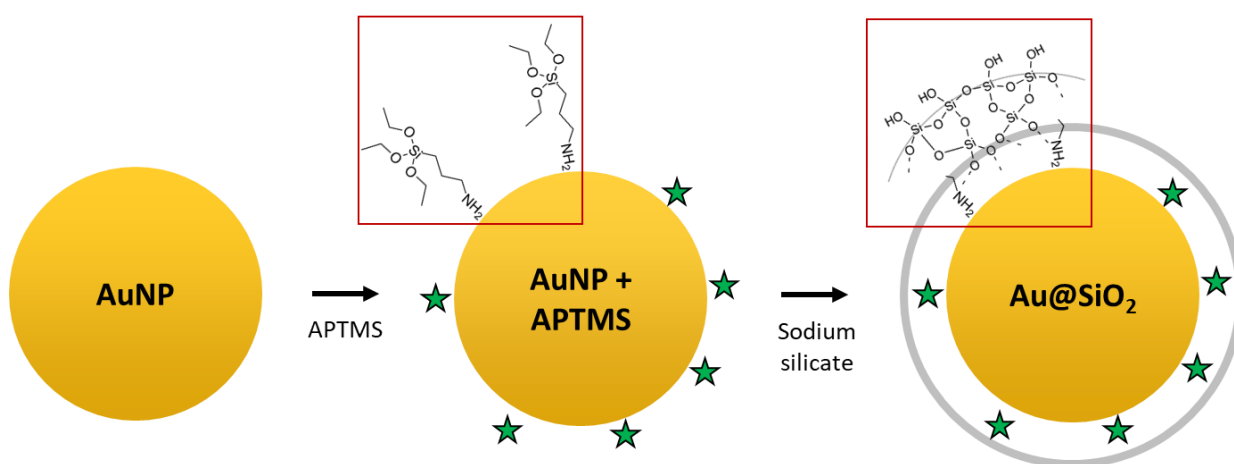


Figure 15. Schematic depiction of the AuNP silica coating procedure. Stars represent APTMS molecules, the grey circle represents a silica coating. In the red squares, an indication of the molecular structure is presented. Silica structure adapted from ref<sup>45</sup>.

The TEM images of the first successfully synthesized silica-coated gold nanoparticles are visible in Figure 16c. The coating thickness ranged between 1-3 nm.

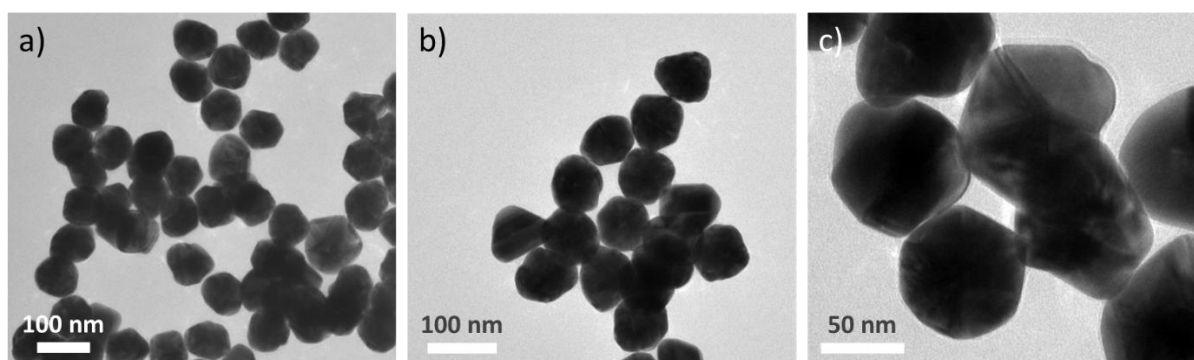


Figure 16. a, b) TEM images of synthesized citrate-stabilized gold nanoparticles. c) TEM image of the same AuNPs, but coated with a silica layer. The coating can be seen as a thin light-grey layer around the dark gold particles.

Both the nanoparticle synthesis and the silica-coating procedure were successfully executed. To verify if the coating is also pinhole-free, a pyridine pinhole test was included in the analysis of the synthesis. The pyridine test works by first drying a droplet of a suspension of silica-coated gold nanoparticles (Au@SiO<sub>2</sub>) and subsequently wetting it with a 1 mM pyridine solution before measuring its Raman

spectrum. Nitrogen containing functional groups tend to bind strongly to gold, hence pinholes could easily be detected by the characteristic (surface-enhanced) pyridine ring vibrations at  $1020\text{ cm}^{-1}$ .

The thickness and quality of the coating have influence on the factor of Raman enhancement. To check the coating quality, we used the probe molecule rhodamine-6G (Rh6G) to verify the enhancement factor for SERS or SHINERS substrates<sup>15</sup> (Figure 17). These methods provide more insight into the quality of the nanoparticles and into the quality of the coating.

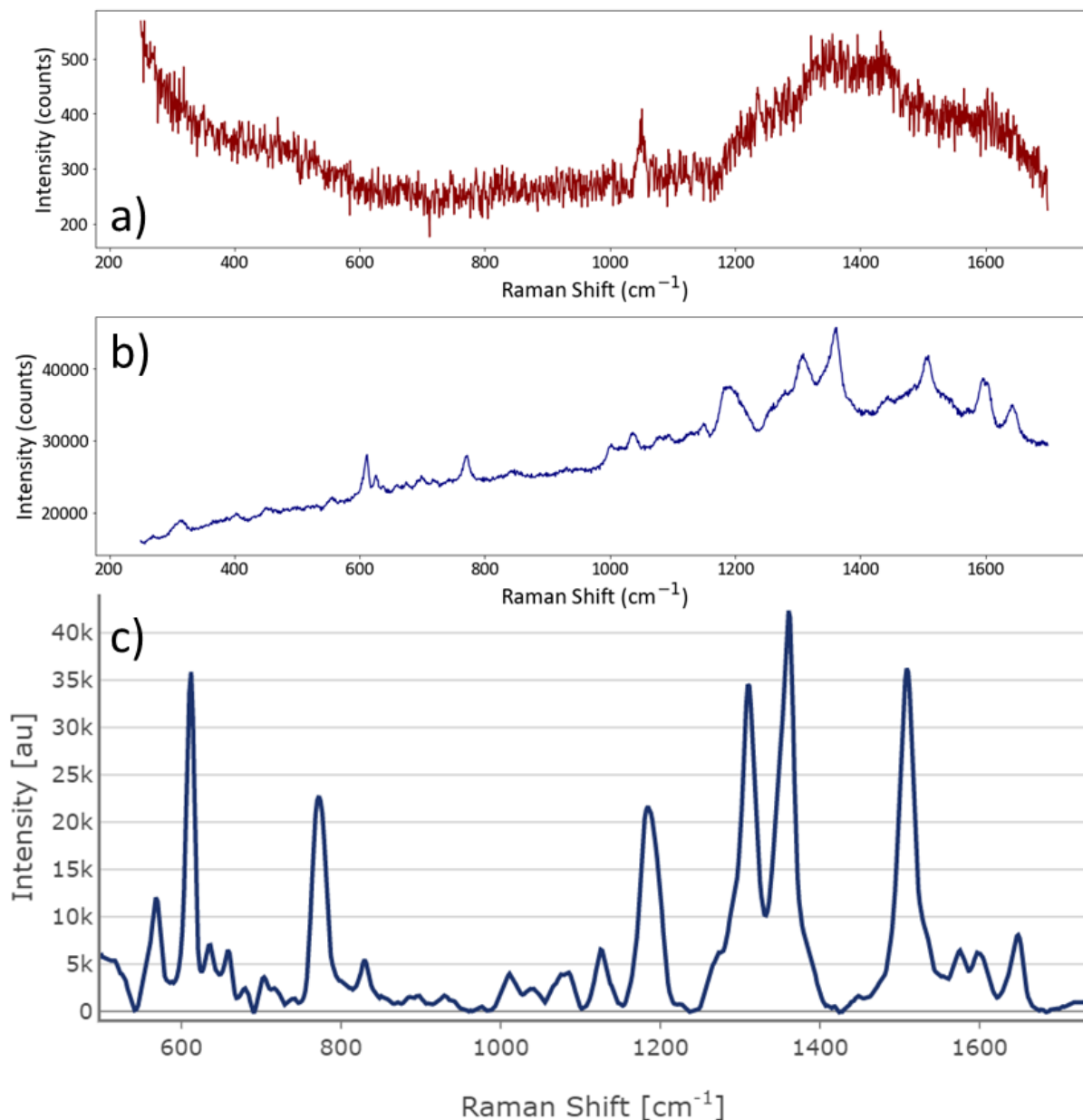


Figure 17. Raman spectrum of a) Au@SiO<sub>2</sub>. b) Au@SiO<sub>2</sub> + Rhodamine 6G. c) Rhodamine 6G, reproduced from ref<sup>46</sup>. It can be seen that the Raman signal enhancement by the SHINs is significant, with maximum counts increasing from 500 to more than 40000.

The next step was the incorporation of a pH probing molecule into the SHINs. Scarpitti *et al.* used a functional organic Raman-spectroscopy based pH sensor: 4-mercaptobenzoic acid (4-MBA), for pH determination in live cells<sup>19</sup>. As this pH probe molecule has already been well-researched, it provided a good starting point for the use of SHINERS in electrochemistry to gain a deeper insight into surface pH.

Therefore, we first decided to reproduce the methods of Scarpitti *et al.* using 4-MBA, but because this molecule is sensitive in acidic-neutral pH environments (pH 6-8)<sup>19</sup>, we later also explored 4-mercaptophenol (4-MP, not used in literature), 4-nitrothiophenol (4-NTP, already used in electrochemistry<sup>47</sup>, but not with SHINERS) and 3-amino-5-mercapto-1,2,4-triazole (3-AMT, reported pH range of 8-12, but on silver<sup>48</sup>). These molecules all work by undergoing changes in their Raman spectrum with changing pH. Herein, we managed to successfully synthesize two pH probes, based on the above mentioned 4-MBA and 4-MP. The 4-MBA probe is thus sensitive in the acidic-neutral regime (around pH 4-8) and the 4-MP probe is more sensitive in alkaline environments (pH 10-14). In Figure 18, the (enhanced) Raman spectra of both molecules adsorbed on gold nanoparticles are presented. In this chapter, the syntheses of the probes are discussed.

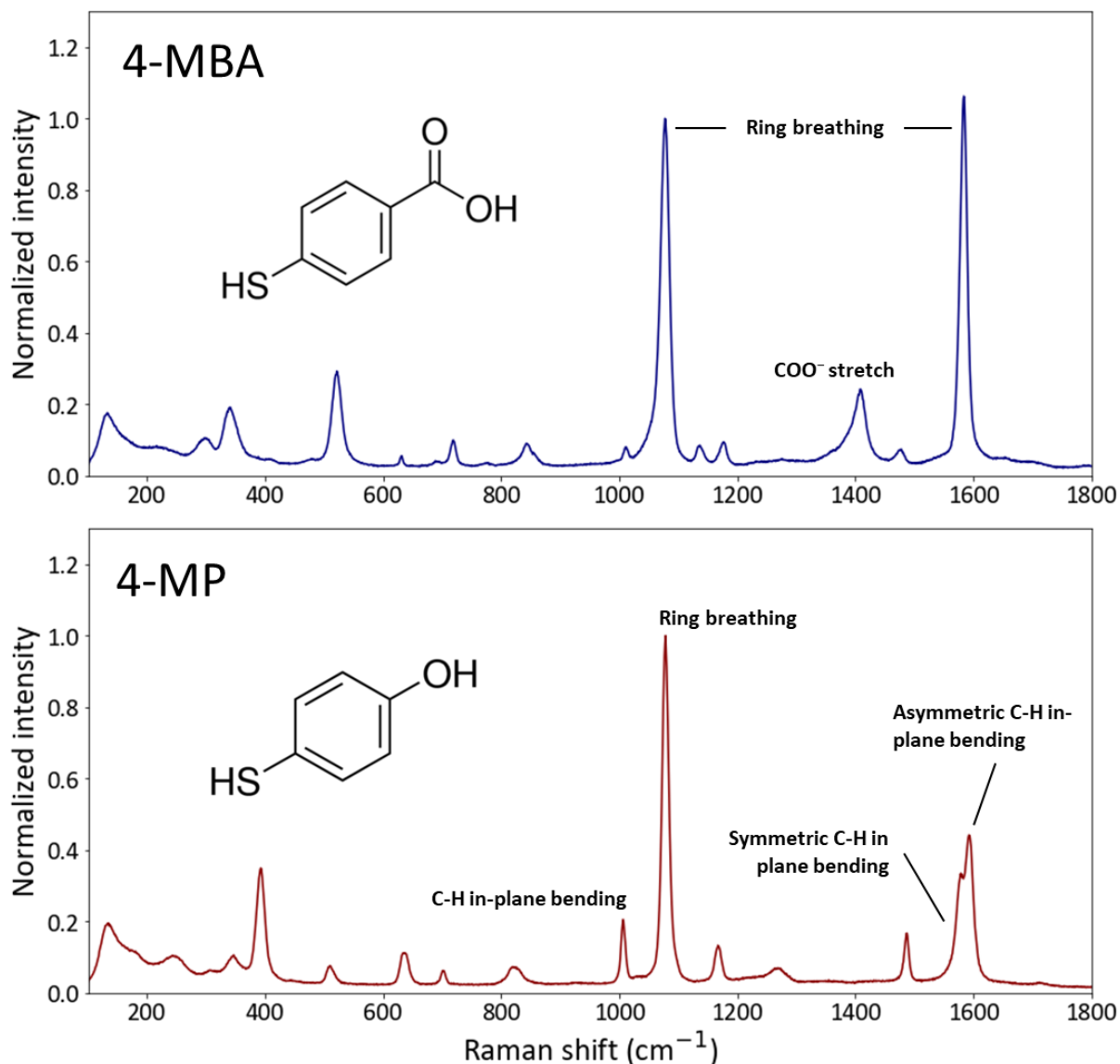


Figure 18. Raman spectra of 4-MBA (upper) and 4-MP (lower) on gold nanoparticles. For 4-MP, the relevant peaks are assigned according to ref<sup>49</sup>.

The incorporation of 4-MBA in the silica shell was studied by modifying the original silica-coated gold nanoparticle synthesis procedure. We found that the introduction of the probe molecule depends on the stage in the synthesis at which it was added. First, we added the 4-MBA together with the APTMS (Figure 19a). In this procedure, the APTMS and 4-MBA were predicted to compete for binding spots on the gold, where 4-MBA would have the upper hand due to its stronger binding affinity to gold. In a

second synthesis, we added it together with the sodium silicate (Figure 19b). Here, it was predicted that APTMS would have covered most of the gold as the 4-MBA comes in, avoiding competition for binding spots. However, 4-MBA binds with a sulfur group, which is stronger than the gold-amine bond formed by APTMS and therefore might replace the silica-linker molecule. Lastly, we added the 4-MBA to already prepared SHINs (Figure 19c). 4-MBA would then only be able to bind to the gold at spots where the coating is lacking in quality and contains pinholes. Also, the probe would not be in the shell, which is unwanted, as the coating should help isolate the probe from the electrochemical events during CO<sub>2</sub> reduction.

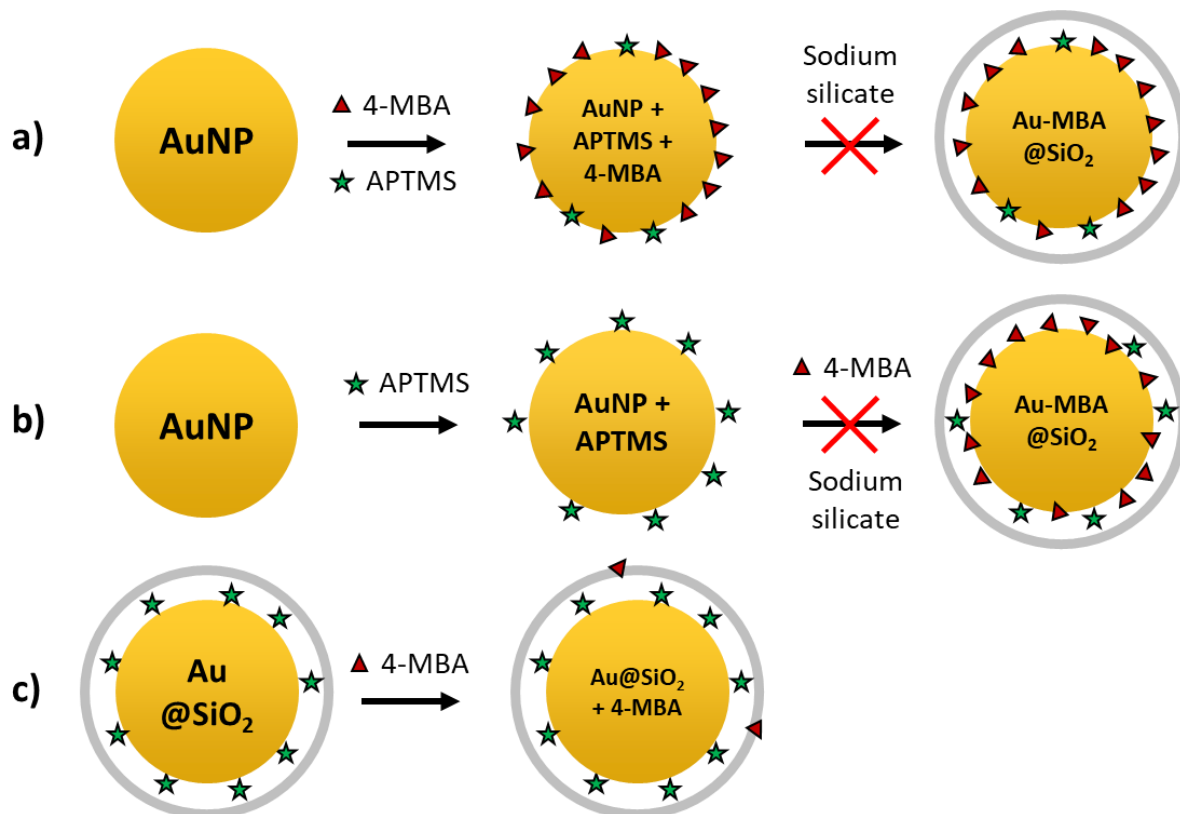


Figure 19. Schemes of Au-MBA@SiO<sub>2</sub> syntheses using APTMS. a) 4-MBA added together with APTMS. b) 4-MBA added together with sodium silicate. c) 4-MBA added to already prepared SHINs.

The results of the first two syntheses looked similar: the nanoparticles had lost most of their color after the synthesis, which indicates a lack of stability and subsequently a high rate of aggregation. Aggregation results in color loss because the confinement needed for localized surface plasmons is lost when the nanoparticles become too large and become bulk gold. Adding 4-MBA to already prepared SHINs caused the resulting suspension to retain its color, which indicates adequate stability.

Nonetheless, all Raman spectra were of low quality (appendix Figure 47), with a high baseline and a lot of noise that caused the relevant peaks to be hard to interpret. An explanation for this is that the 4-MBA replaces all of the APTMS in the first two syntheses, because of its thiol group having a stronger affinity for gold than the amine group of APTMS. Hence, the coating was not formed and the AuNP have low stability, resulting in aggregation. To solve this problem, we decided to use (3-mercaptopropyl)trimethoxysilane (MPTES, Figure 20) instead of APTMS. It was expected that competition between the linker MPTES and the probe 4-MBA would still happen, but without favoring the 4-MBA as now both contain the same functional thiol group.

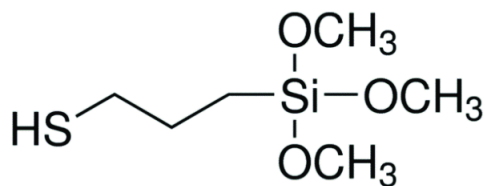


Figure 20. (3-mercaptopropyl)trimethoxysilane, a thiol-based linker molecule for starting silica growth.

Multiple syntheses using MPTES were conducted, where the 4-MBA was added at different steps in the synthesis. We added the 4-MBA three minutes after adding sodium silicate (Figure 21a), as we expected the 4-MBA to bind so strongly that even after a few minutes of silica growth it would find places to bind and be incorporated in the coating. This resulted in a film of aggregated gold on the bottom of the centrifuge tube after centrifugation, which indicated low stability and therefore the absence of a silica coating. In another synthesis, we added the 4-MBA together with the MPTES (Figure 21b), so that both molecules can bind to the gold nanoparticles simultaneously. As both bind with a thiol group, binding affinity was expected to be roughly equal. This procedure improved stability, as no gold film was visible in the centrifuge tubes. Next, we added 4-MBA three minutes before adding MPTES (Figure 21c) to make sure 4-MBA is adsorbed on the gold prior to coating growth. As with the previous synthesis, no aggregation was visible after centrifugation. As a control procedure, we also added 4-MBA without adding any linker molecules (no APTMS or MPTES, Figure 21d). Sodium silicate needs a linker molecule to successfully form a silica coating, so this experiment was bound to fail. Expectedly, gold aggregation was visible after centrifugation, which indicated that no coating was formed.

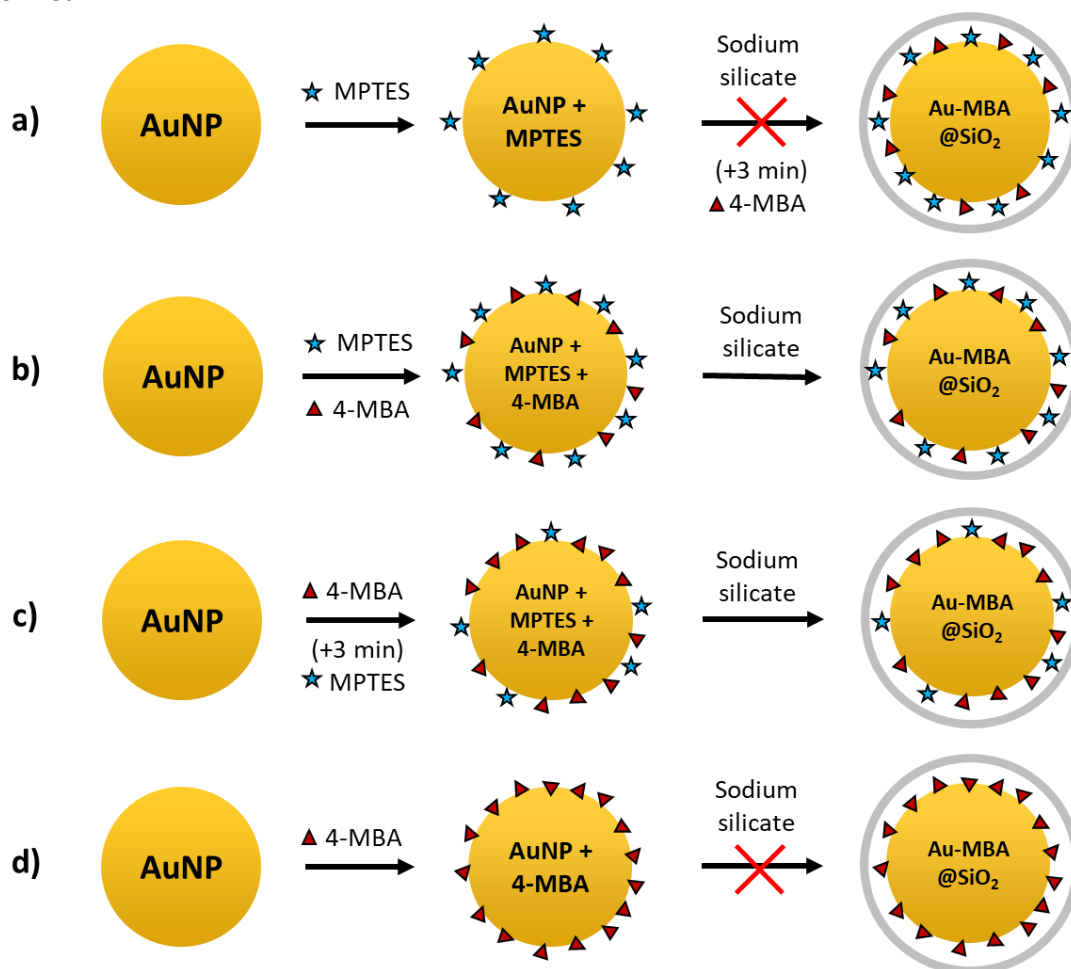


Figure 21. Schemes of Au-MBA@SiO<sub>2</sub> syntheses using MPTES. a) 4-MBA added 3 minutes after sodium silicate. b) 4-MBA added together with MPTES. c) 4-MBA added 3 minutes after MPTES. d) No MPTES used.

We tested the Raman signal of all samples, and the clearest Raman signals were observed for the procedure where 4-MBA was added before the MPTES (appendix Figure 48a). However, the Raman spectrum still featured several extra peaks that could not be assigned and the signal to noise ratio could still be improved. Therefore, we tried several additional optimization steps: decreasing and increasing coating growth time, increasing the amount of 4-MBA and adjusting the time between 4-MBA and MPTES addition. Eventually, we found that the increase of 4-MBA from 10 to 20  $\mu\text{l}$  (0.03 mM aqueous solution) and adding 4-MBA 6 minutes instead of 3 minutes before MPTES resulted in a clearer Raman spectrum, giving rise to relatively high intensity Raman signals in which 4-MBA is recognizable (appendix Figure 48b). Still, the spectrum featured several additional unexpected peaks, which might be due to the linker molecule itself. Additionally, the pyridine pinhole test indicated an inhomogeneously coated sample, as visible in the spectrum in Figure 22. In this spectrum, an extra peak is visible, at  $1240\text{ cm}^{-1}$ , which is attributed to an impurity in the sample. In addition to the pyridine test, TEM images were collected to gain visible information about the quality of the coating (Figure 23). From these images, it became clear that there are several spots where the coating is missing or where the thickness diverges from other spots. These results pointed out that the silica coating procedure for incorporating 4-MBA still needed improvement, in order to get a homogeneous coating, stable nanoparticle suspensions and clear Raman spectra.

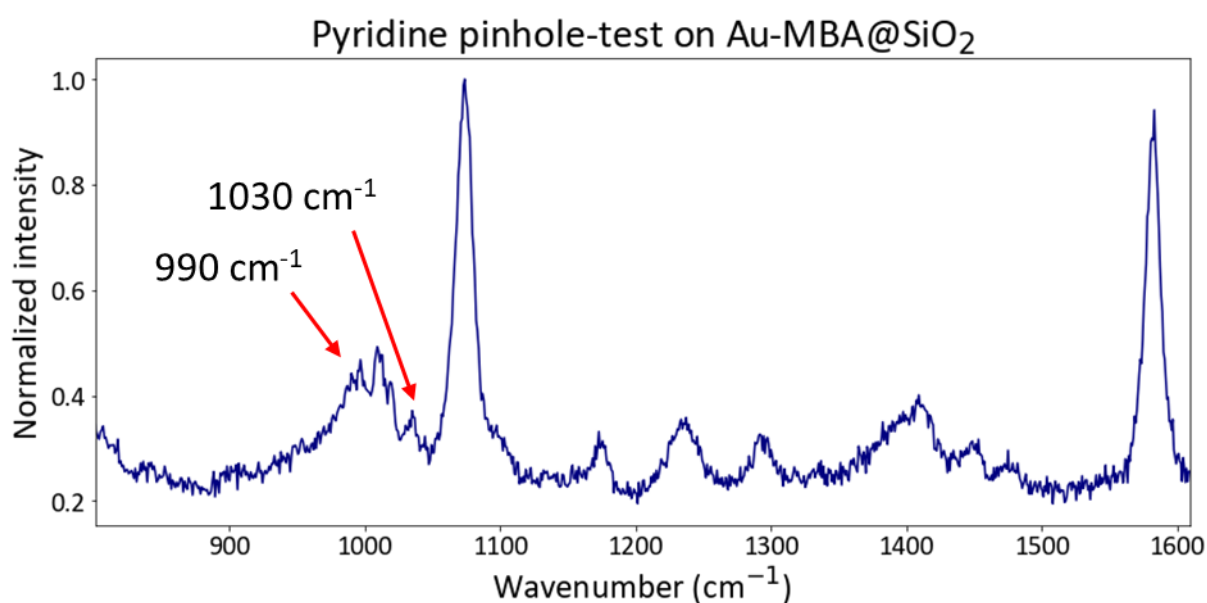


Figure 22. Pyridine pinhole test Raman spectrum. The characteristic pyridine peaks are indicated with red arrows and their presence in the spectrum indicates that the silica coating contains pinholes.

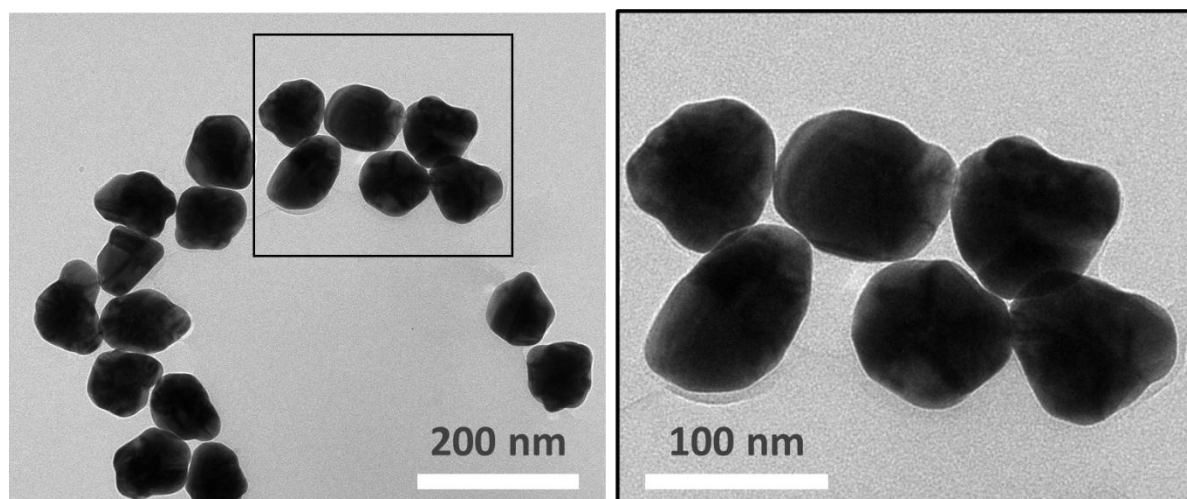


Figure 23. TEM images of Au-MBA@SiO<sub>2</sub>. In the enhanced image (right), the inhomogeneity of the coating is clearly visible.

To improve our synthesis, we decided to look for alternative routes. In the work of Wei *et al.*, they used 4-MBA in a ‘SERS-based immunoassay’<sup>34</sup>. For this purpose, they made 4-MBA-functionalized gold nanoparticles and coated them with silica (Au-MBA@SiO<sub>2</sub>), before using them as bio-focused nanotags. Using tetraethyl orthosilicate (TEOS), they managed to use the 4-MBA itself as the linker molecule between the gold and the silica layer (Figure 24). Based on this, we synthesized our own Au-MBA@SiO<sub>2</sub> particles using TEOS to check whether they would be effective as a SHINERS-based pH probe.

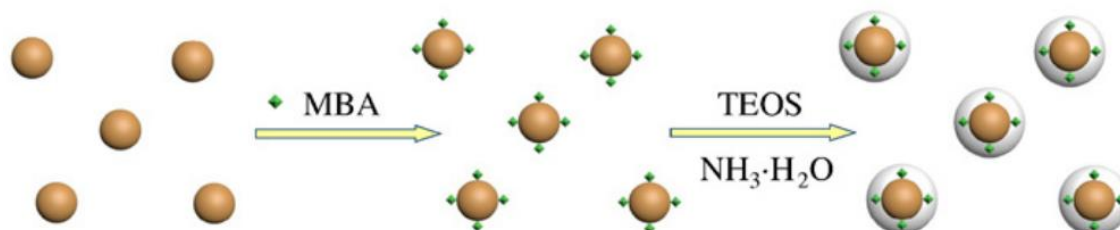


Figure 24. Preparation of 4-MBA functionalized gold nanoparticles (Au-MBA@SiO<sub>2</sub>). Figure reproduced from ref<sup>34</sup>.

After several syntheses of using TEOS as silica source, we managed to optimize the procedure and successfully coated 4-MBA-functionalized gold nanoparticles with a thin silica layer. This was confirmed by both TEM imaging and pyridine pinhole testing, which are shown in Figure 25. The key step in the optimization was the use of a syringe pump to add TEOS more gradually (30  $\mu$ l over 2 hours = 15  $\mu$ l/hour). Also, we added more TEOS in total, because our gold nanoparticles were larger and thus required more silica than in the work of Wei *et al.*

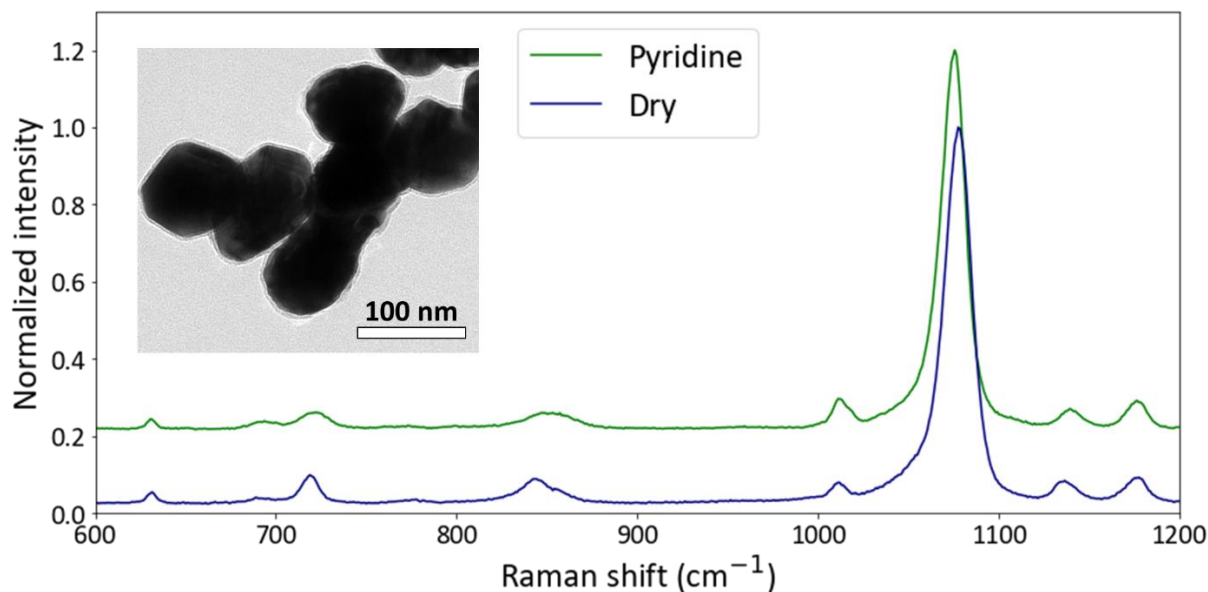


Figure 25. Raman spectrum of dry and pyridine-treated Au-MBA@SiO<sub>2</sub> particles produced with TEOS. Note how there is no pyridine peak visible, which suggests a pinhole-free silica layer. Inset figure is a TEM image of the same particles and shows a homogeneous coating.

Expanding the 4-MBA-based pH probe synthesis to 4-mercaptophenol, we copied the procedure but replaced the 4-MBA with 4-MP. It appeared, however, that upon addition of a 4-MP solution to gold nanoparticles, the particles slowly lose their color over time (Figure 26). Hard to see in the figure is the solid black precipitation that floats in the suspension, which indicates that the nanoparticles are not dissolving. Therefore, the color loss is attributed to aggregation of gold nanoparticles that seemingly lose their stability when exposed to 4-MP particles. The AuNPs in this work are citrate-stabilized, and upon addition of 4-MBA the citrate molecules are replaced and the particles become 4-MBA-stabilized.

Both citrate and 4-mercaptobenzoic acid have negatively charged acid groups, which cause effective repulsion between the nanoparticles, preventing unwanted aggregation. On the other hand, 4-MP has a much more basic OH-group. As the  $pK_a$  of phenol is around  $10^{5.0}$  and the solution of gold nanoparticles has a pH between 4 and 5, the alcohol groups are mainly protonated, yielding a neutral group. In turn, the absence of the necessary inter-particle repulsive forces causes a significantly increased rate of aggregation (Figure 27). This means that the confinement of the nanoparticles becomes less and eventually disappears. As visible in Figure 26, this translates in the loss of light scattering and absorption and over time renders the suspension virtually colorless.

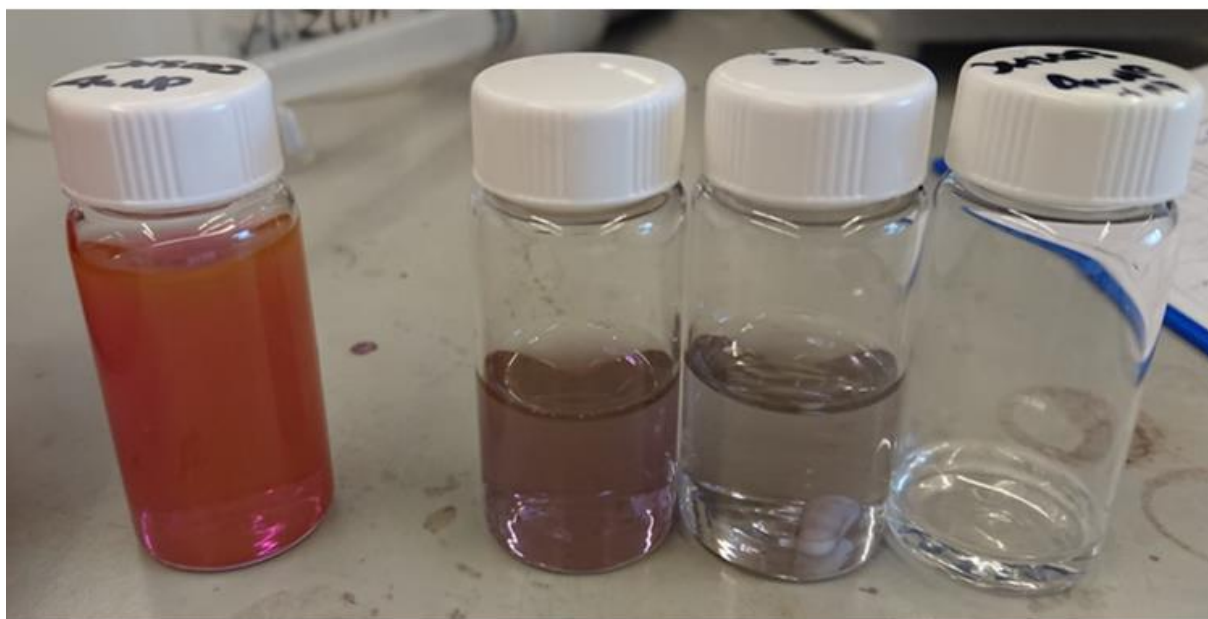


Figure 26. Gold nanoparticle aggregation upon addition of 4-mercaptophenol after different amounts of time. From left to right: AuNPs, AuNPs + 4-MP (two minutes), AuNPs + 4-MP (ten minutes), AuNPs + 4-MP (two days).

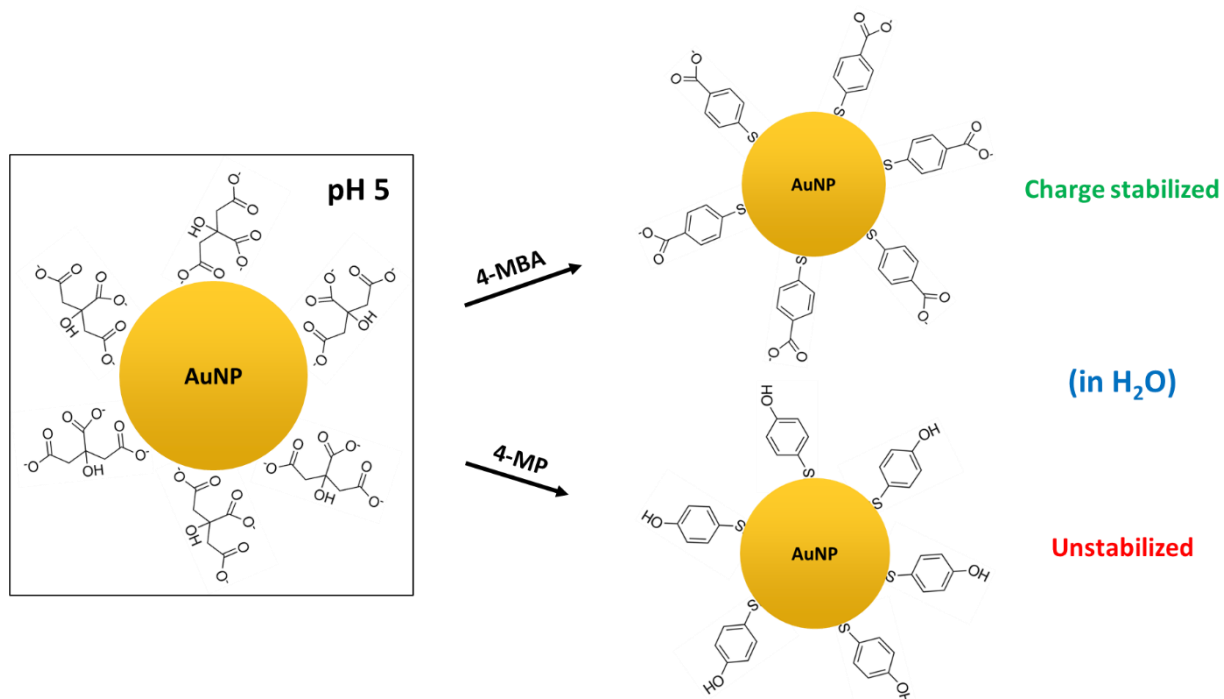


Figure 27. Effects of the substitution of citrate molecules for 4-MBA and 4-MP on gold nanoparticle stability in water. The protonated alcohol group is argued to be the cause of unwanted aggregation in low-medium pH environments.

To resolve this problem, we increased the pH of the citrate-stabilized gold nanoparticles prior to adding the 4-MP probe molecule to make sure that the OH-group would be deprotonated and therefore retain the charge stabilization. This was done by adding different amounts of ammonia solution, as this is also used as base catalyst for TEOS growth. Subsequently, 4-MP was added and the AuNP suspension retained its color, which was expected based on our explanation. We found that the pH should be at least 8.5 prior to addition of 4-MP in order to retain AuNP stability and prevent aggregation. To make sure that the Au-MP was in fact stable, an excess of 4-MP was added to a nanoparticle suspension of pH 9.6 and the sample was left untouched in a vial for a week. After this time, the suspension still had its original color, confirming that increasing the pH indeed has a significant effect on the stability of the gold nanoparticles.

Having solved the 4-MP stability problem, we continued pH probe preparation by isolation of the Au-MP with a silica coating. Using a procedure similar to the optimized 4-MBA procedure, the coating was successfully synthesized. However, it appeared that the coating was not homogeneous in terms of thickness, which is clear when looking at the TEM images in Figure 28a-c. A reason for this could be that the stirring during the addition of TEOS was insufficient, causing inhomogeneous coating growth. The pyridine pinhole test indicated that the coating did not contain a significant number of pinholes, but was not pinhole-free (Figure 28d). It should be noted that the procedure used for silica growth using TEOS as described in the work of Wei *et al.*<sup>34</sup> is specific for 4-MBA-functionalized AuNPs, as they ascribe the successful coating growth to the interaction of hydrolyzed TEOS with the carboxylic acid groups of the 4-MBA. With this in mind, it is understandable that a similar reaction involving the alcohol group and TEOS might have different properties, which may have caused the deviating result.

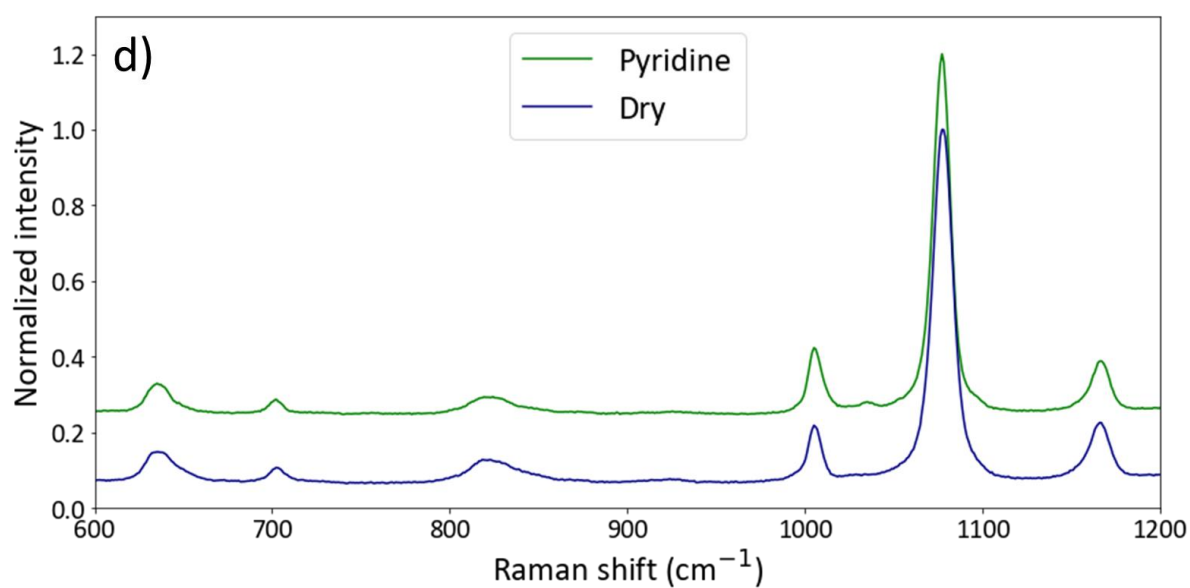
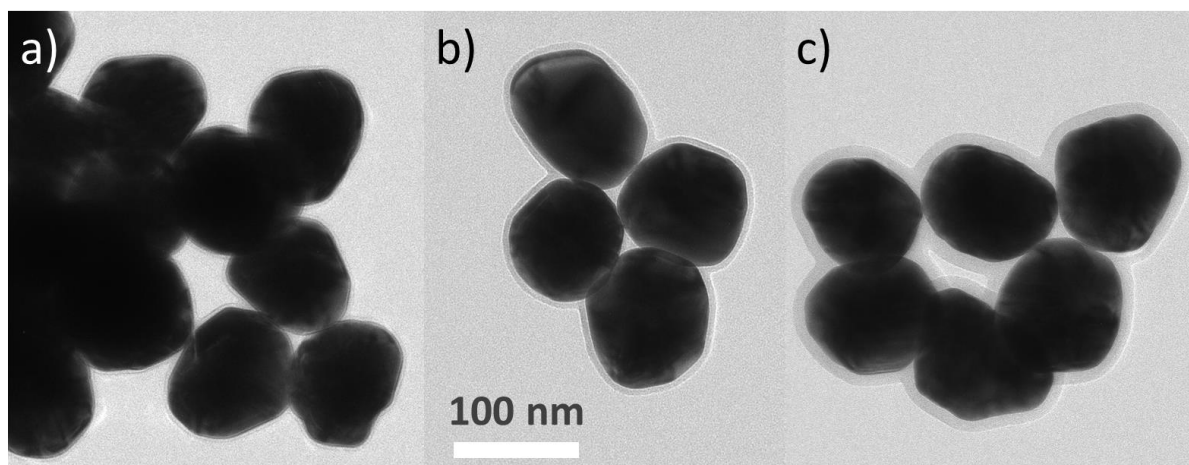


Figure 28. a-c) TEM images of the same sample of Au-MP@SiO<sub>2</sub> particles. It can be seen that the coating thickness varies significantly. d) Raman spectrum of dry and pyridine-treated Au-MP@SiO<sub>2</sub> particles produced with TEOS. Note the small pyridine peak at 1030 cm<sup>-1</sup>, which suggests the presence of some pinholes.

## 4.2 Probe utilization for pH calibration curve determination

The first step towards a successful pH probe is the determination of a pH calibration curve. This is done by measuring Raman spectra of the probe (Au-MBA@SiO<sub>2</sub> and Au-MP) at different pH values. In preparation, phosphate buffer solutions with known pH were prepared in a range of pH 4 up to pH 13. To measure the Raman spectra, 10  $\mu$ l of probe suspension is dropcasted on a glass plate and dried. Subsequently, a droplet of buffer solution is applied and covered with another glass plate (Figure 29).

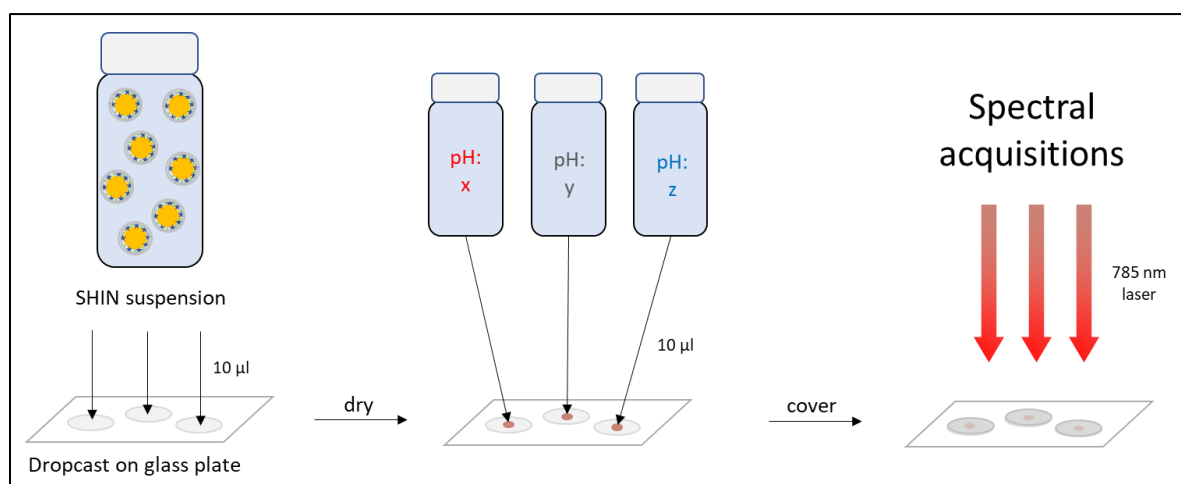


Figure 29. Preparation procedure for determining a pH calibration curve. In this work, potassium phosphate buffer solutions with known pH were used. Ideally, a trend in the resulting Raman spectra for solutions with different pH values is clearly identifiable.

For the 4-MBA probe, the Raman spectra at different pH values are depicted in Figure 30. From these spectra, there appear to be four peaks that increase or decrease in intensity with pH: at 1138  $\text{cm}^{-1}$  (C-H in-plane bend), at 1415  $\text{cm}^{-1}$  (COO<sup>-</sup> symmetric stretch), at 1483  $\text{cm}^{-1}$  (ring chain vibrations) and at 1710  $\text{cm}^{-1}$  (C=O symmetric stretch). A trend that is harder to see is the shift in the peak at approximately 1585  $\text{cm}^{-1}$ , which is attributed to the ring C-C stretching mode.<sup>19, 33,51-53</sup> The pH sensitivity in the 1415 and 1710  $\text{cm}^{-1}$  peaks is straightforward, as the vibrational energy of the carboxylic acid group is directly affected by its protonation state. More protonation will cause a decrease of the COO<sup>-</sup> symmetric stretch peak, as the group is mainly in its protonated form at low pH (COOH). Similarly, the C=O symmetric stretch peak at 1710  $\text{cm}^{-1}$  decreases with high pH due to the resonance forms of the COO<sup>-</sup> group, where there is no longer a well-defined double bond. We attribute the pH-dependency of the C-C stretching vibration at 1585  $\text{cm}^{-1}$  to the resonance that is induced when the carboxylic acid group of 4-MBA is deprotonated. This in turn affects the bond strength in the aromatic ring and therefore causes a shift with changing pH.

When looking at Figure 31, it is clearly visible that with increasing pH, the 1585  $\text{cm}^{-1}$  peak shifts to lower energies (redshifts) and a calibration curve could be determined. For completeness, we also determined calibration curves using the other (intensity-based) trends, which are visible in appendix Figure 49. The spectra used for calibration curve determination are based on the average of 11 spectra that were taken for each pH measurement. When comparing the calibration curves, it can be seen that the peak shifting trend bears the most resemblance to the expected titration curve S-shape. Therefore, we decided to focus on the 1585  $\text{cm}^{-1}$  peak for pH determination. From this trend, it can be concluded that the probe is most sensitive around neutral pH, from approximately pH 6-8, which is in agreement with literature<sup>53</sup>, where Bishnoi *et al.* report a sensitivity of 5.80 to 7.60. Using the vibrational redshift at 1585  $\text{cm}^{-1}$  to explain, this conclusion follows naturally from the fact that the peak wavenumber undergoes the most significant changes around pH 7. For example, an increase from pH 6.5 to 7.5 could easily be determined using their respective Raman spectra, as the peak wavenumber would shift almost 3  $\text{cm}^{-1}$ . On the other hand, an increase from pH 10 to 11 would be impossible to determine, as the wavenumber does not shift at all. The reason for the difference in sensitivity can be explained by

taking into account the  $pK_a$  of the pH-dependent group of 4-mercaptobenzoic acid. When the pH of the environment is around the  $pK_a$ , small changes in pH have relatively large effects on the protonation of the acid group and vice versa, as discussed in the theory chapter. Note that the  $pK_a$  of the carboxylic acid group of 4-MBA is around 4.8 in solution, which would make the probe sensitive at even lower pH. In the work of Phan *et al.*, however, they found that adsorption of 4-MBA on nanoparticles increases the  $pK_a$  of the acid group up to 7.7 because of increasing intermolecular interactions<sup>54</sup>. This is in agreement with our findings, as our 4-MBA probe is most sensitive around pH 7.

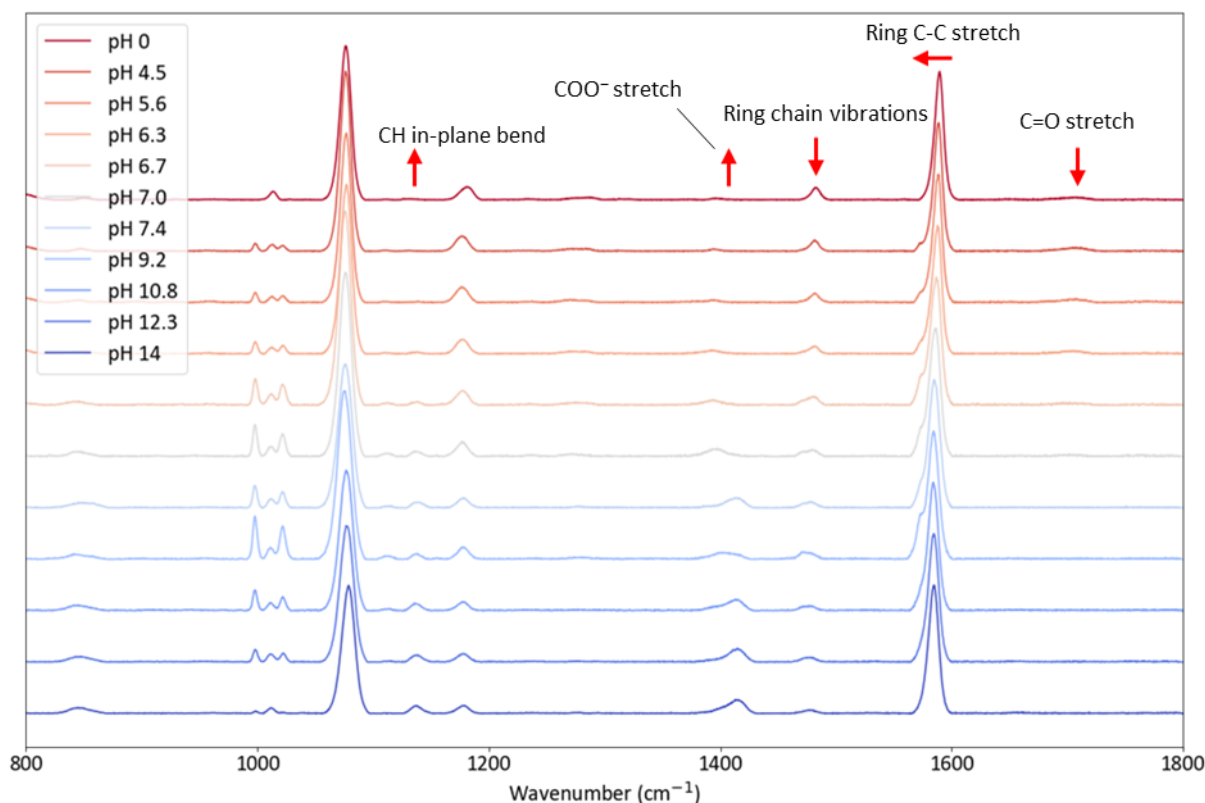


Figure 30. Raman spectra of the 4-MBA-functionalized silica-coated gold nanoparticle probe at different pH values. Spectra are averages over 11 spectra. Red arrows indicate pH-dependent trends.

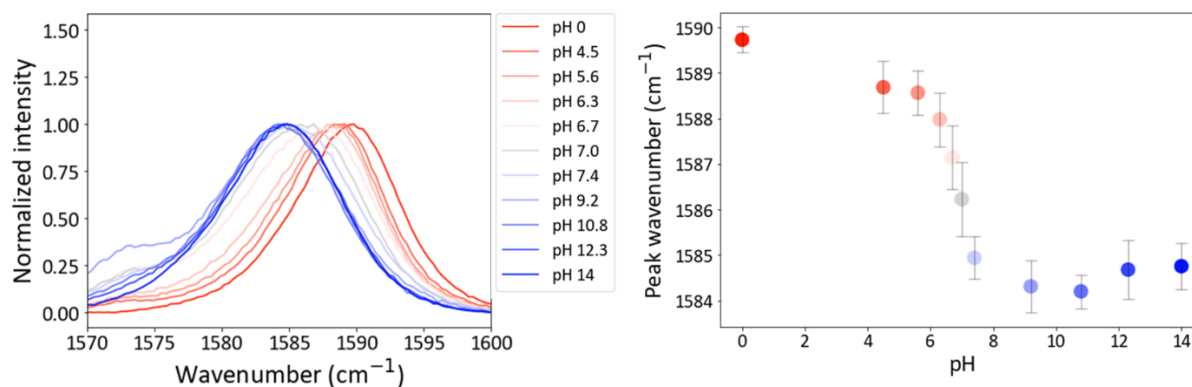


Figure 31. Left: redshifting trend of C-C stretching vibration of 4-MBA. Right: pH calibration curve for the Au-MBA@SiO<sub>2</sub> probe.

The 4-MBA pH probe is functional and the calibration curve was successfully determined, however, the pH range is not optimal for application in the CO<sub>2</sub> reduction reaction. Therefore, we focused on first utilizing our 4-MP probe, where a similar procedure was used. In Figure 32, the spectra for the probe at different pH are provided. In contrast with 4-MBA, 4-MP does not have a peak shifting trend, which we ascribe to the absence of resonance structures. No resonance structures means no influence of protonation on the C-C bond strengths in the aromatic ring and therefore no shift in vibrational energy. There are, however, several peaks that increase or decrease in intensity with changing pH, so

using certain ratios between peaks, calibration curves based on peak ratio can be determined. In Figure 33, the trends are plotted along with their respective calibration curves. As the shape of all curves is roughly the same, it can be stated that there is definitely a pH dependence for 4-MP. Unlike the 4-MBA probe, this probe is most sensitive in basic pH, as the peak ratios undergo the most changes from around pH 10 (going up). This proves more useful in CO<sub>2</sub> electroreduction, as the starting pH of the CO<sub>2</sub> saturated potassium bicarbonate electrolyte is 6.8 and OH<sup>-</sup> is formed in all reactions, causing an increase in pH (expected up to 12). Nonetheless, our 4-MP probe still does not have optimal sensitivity, as small increases (to pH 9, for example) would not be distinguishable. For the application of the 4-MP probe, we focused on two of the four trends: the 1564/1591 cm<sup>-1</sup> and the 1575/1591 cm<sup>-1</sup> peak ratios, as these peaks had the highest relative intensity and thus suffer the least from a low signal to noise ratio.

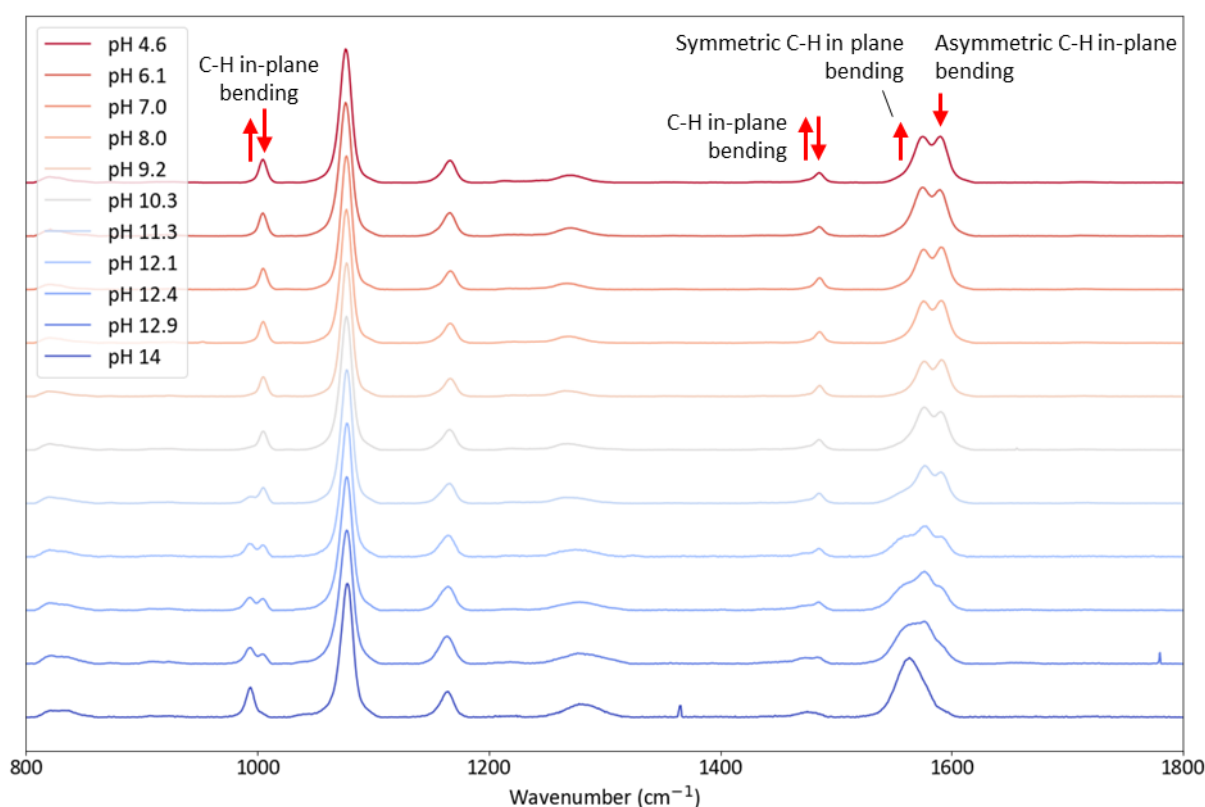
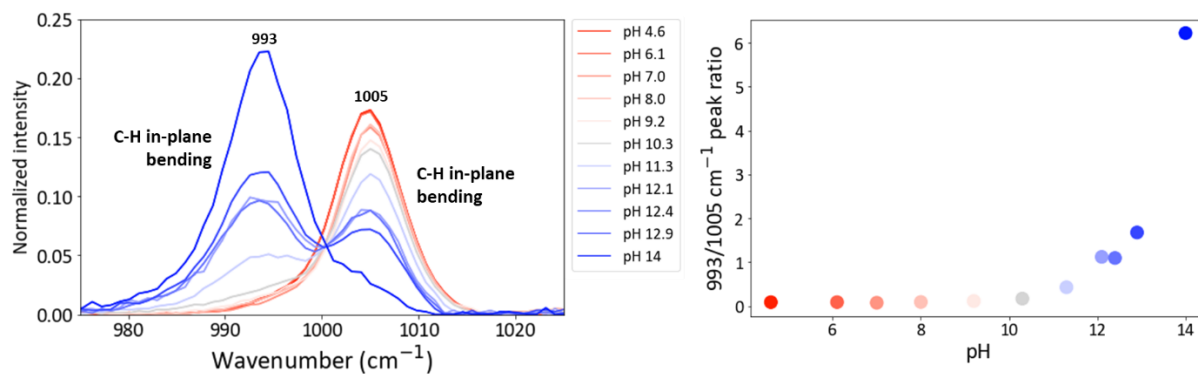


Figure 32. Raman spectra of the 4-MP-functionalized gold nanoparticle probe at different pH values. Red arrows indicate pH-dependent trends. The assignments of the vibrations is based on ref<sup>49</sup>.



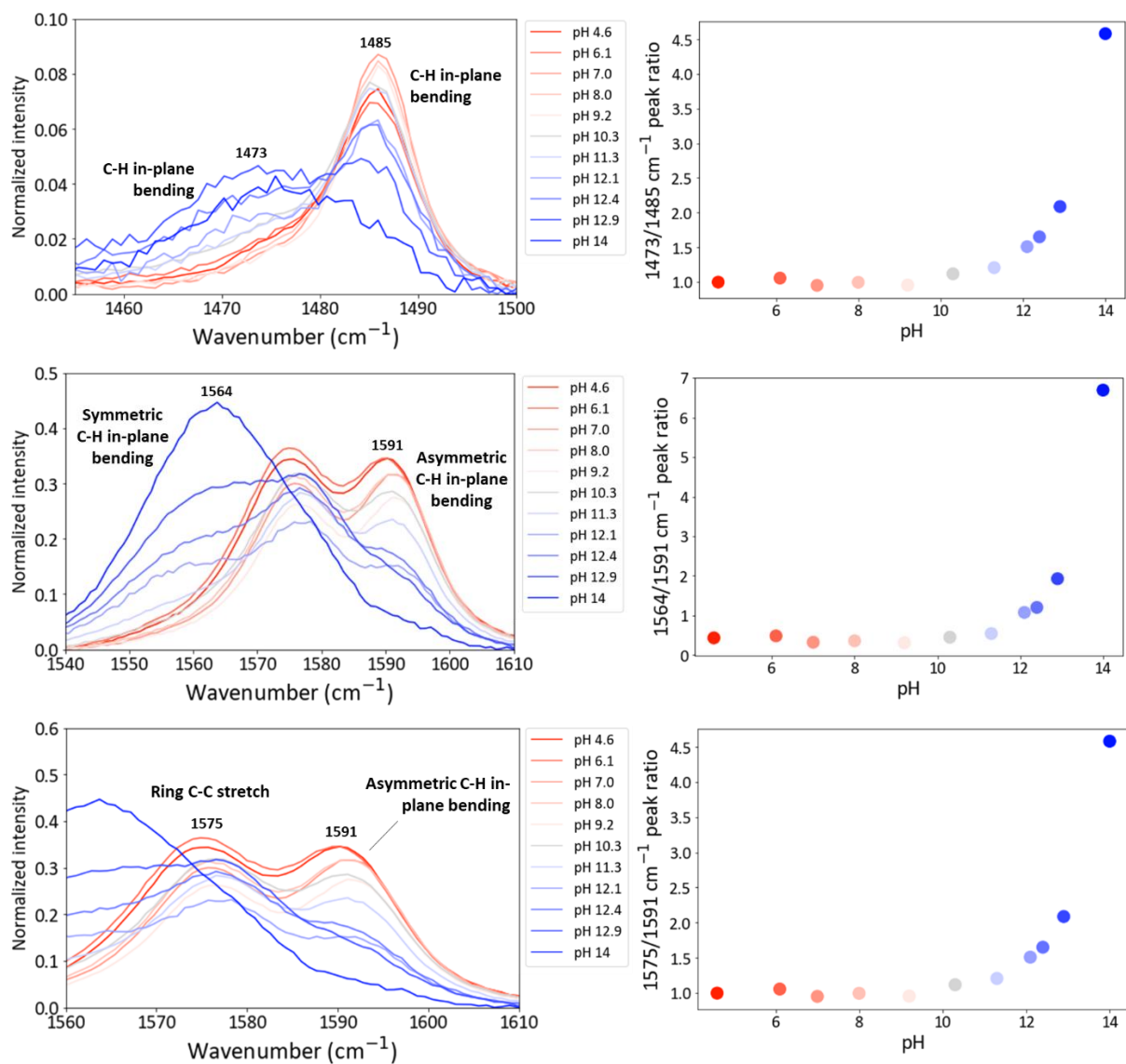


Figure 33. The pH-dependent Raman spectrum trends for four different peaks for the 4-MP probe. Note how all calibration curves have similar shapes.

Calibration curves for both pH probes have been successfully determined, in different pH ranges, so the next step is to use them in electrochemistry, which is discussed in the next section.

### 4.3 *In situ* Raman spectroscopy during electrochemical CO<sub>2</sub> reduction

To get an idea of the probes' behavior during electrochemistry, cyclic voltammetry is a good start to get a complete image of the spectra at different potentials. At reductive potentials, pH is expected to go up due to CO<sub>2</sub> reduction, whereas at oxidative potentials, pH is expected to go down due to the formed OH<sup>-</sup> diffusing away from the surface. This means that when we use our probes, we will be able to see many pH changes during the measurement.

#### 4.3.1 Application of the Au-MBA@SiO<sub>2</sub> probe

To apply the pH probes, the nanoparticle suspension was dropcasted and subsequently dried on a plated (electrodeposited) copper piece prior to using it in the electrochemical cell. The stability of the probes on the surface was investigated by measuring Raman spectra after several cycles of a CV measurement, and proved sufficient as the 4-MBA Raman signal was still recognizable after the CV (appendix Figure 50). Plated copper was used, because the rough surface increases the surface area and thereby the catalytic activity of the electrode. For this cyclic voltammetry measurement, the potential was varied from 0.55 V to -0.85 V to 1.05 V and back to 0.55 V (all vs. RHE) for 4 cycles in total (Figure 34). The regions for copper oxidation, copper reduction and CO<sub>2</sub> reduction are also indicated. It can be seen that the first cycle deviates from the remainder of the cycles, which is why four cycles are measured to ensure a stable and reproducible measurement. The reason for this deviation is that the surface has not been oxidized yet, and only the copper oxide that was already on the copper is reduced. Additionally, the starting point of the first cycle indicates the open circuit potential ( $V_{oc}$ ).

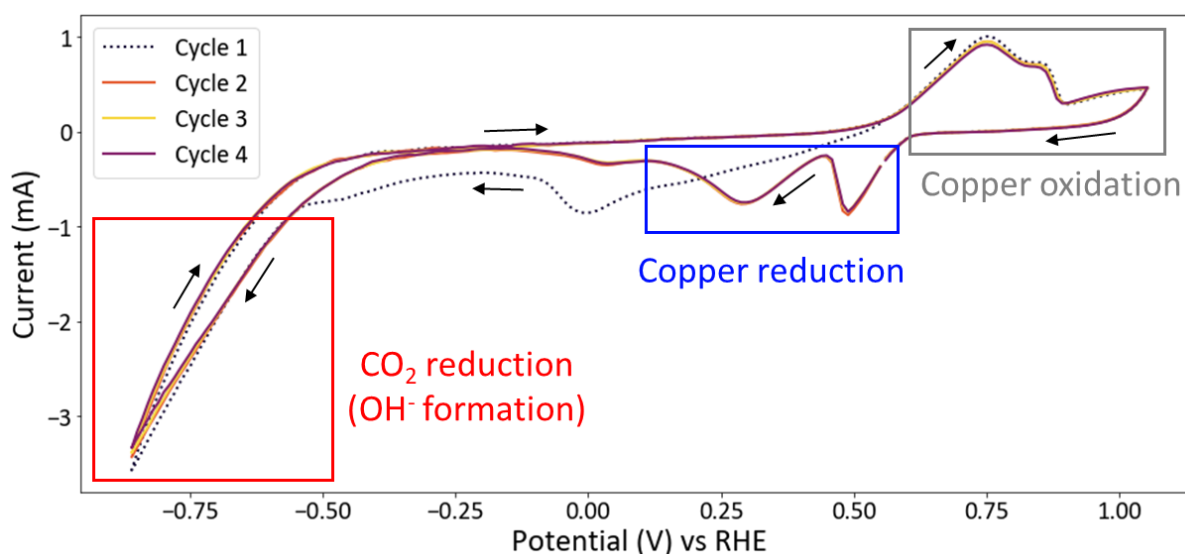


Figure 34. *I/V* diagram for the Raman-CV measurement for the 4-MBA pH probe on plated copper. Reduction and oxidation events are indicated with squares and the chronological direction of the measurement is indicated with arrows.

During the CV, we continually measured Raman spectra of the pH probes adsorbed to the surface. This way, we tried to find a correlation between potential and the pH-dependent Raman spectrum trends of the 4-MBA probe (such as a redshift of the 1580 cm<sup>-1</sup> peak). A spectrum was collected every four seconds, and the CV scan rate was 10 mV/s. This means that one Raman spectrum is taken for every step of 0.04 V in the CV. In Figure 35, the results of this time-resolved Raman experiment are depicted for the second CV cycle. The top graph (Figure 35a) is the chronological *I/V* curve from positive to negative potentials for the 2<sup>nd</sup> cycle. This is essentially the same as the second cycle in Figure 34, but now the x-axis is chronologically ordered and with decreasing potential, which is useful for comparing potentials with corresponding Raman signals. The first two peaks in the *I/V* curve are assigned to the reduction of Cu<sub>2</sub>O to Cu<sup>0</sup> (left) and the reduction of CuO to Cu<sub>2</sub>O (right), according to the work of Briones *et al.*<sup>55</sup>.

Depicted below the I/V curve is a heatmap of the Raman spectra (Figure 35b), where the same chronological order of potential is on the x-axis, the Raman shift wavenumber is on the y-axis, and the Raman intensity is depicted as a color in the heatmap, increasing from purple to yellow. This figure gives a clear overview of the changes in Raman signals in response to the applied potential. Therefore, it should be possible to see changes in the peaks that we used for the calibration curves. To summarize: for increasing pH, we expect a redshift in the 1585  $\text{cm}^{-1}$  peak, and an increase in intensity for the 1415  $\text{cm}^{-1}$  peak. When looking at the heatmap, it can be seen that a peak around 1400 increases with more negative potentials. To see the spectral behavior more clearly, the spectra at 0.51 V and -0.38 V are depicted in Figure 35c and d, and are indicated with a red and orange line in the heatmap, respectively. It can be seen that the spectra deviate in a number of ways from the normal 4-MBA spectrum.

At oxidative potentials, the signal from 4-MBA disappears almost completely, and only the (very weak) 1080  $\text{cm}^{-1}$  and 1585  $\text{cm}^{-1}$  peaks can be distinguished. We ascribe this to the presence of copper oxide, which covers the plated copper electrode. This means that the SERS-active copper is now further away from the 4-MBA probes, reducing enhancement effects, as the number of Cu-Au enhancement hotspots is drastically reduced (see Figure 36). This result clearly shows that there is a significant enhancement effect between the electrode and SHINs, which is needed for a clear Raman spectrum. Another explanation is that the copper oxide might cover a substantial fraction of the adsorbed 4-MBA probes, which in turn blocks their Raman signal. This might be possible because the dendrites formed on the plated copper electrode are larger than the probes, as visible in the SEM image in Figure 37.

Both explanations are supported by the fact that the spectrum in Figure 35c shows peaks at 400, 520 and 610  $\text{cm}^{-1}$ , which are characteristic for copper(I)oxide. In the heatmap, they are increasing in intensity from the start of the CV (1.05 V vs. RHE) until approximately 0.25 V, where they disappear altogether. Coincidentally, this is also the potential where the reduction of copper(I) to metallic copper happens, as visible in the I/V curve above. We argue that this is due to the gradually stronger reducing potential causing the constant reduction of  $\text{Cu}^+$ , thinning the copper oxide layer on top of the metallic copper electrode. Consequently, the distance to the SERS-active copper becomes shorter and the Raman signal gets increasingly more enhanced. Therefore, the three peaks increase in intensity until all of the copper oxide is reduced, and then suddenly disappear from the spectrum. Immediately after, the peak around 1060-1080  $\text{cm}^{-1}$  drastically increases in intensity, which is attributed to the ring breathing vibration of 4-MBA (1076  $\text{cm}^{-1}$ ), but also to  $\text{CO}_3^{2-}$  adsorbed on the copper, which is expected around 1065  $\text{cm}^{-1}$ , according to Klingan *et al.*<sup>56</sup>. This again shows the considerable increase in enhancement when going from copper oxide to metallic copper.

At reductive potentials (Figure 35d), the 4-MBA spectrum is more recognizable. The bands at 1080 and 1585  $\text{cm}^{-1}$ , assigned to ring breathing vibrations, are the most intense peaks. However, the  $\text{COO}^-$  stretching peak at 1415  $\text{cm}^{-1}$  appears to have shifted to just below 1400  $\text{cm}^{-1}$ . We believe that this is due to the electronic effects on Raman signal enhancement that arise when exposed to an applied potential, such as the Stark effect. This effect describes the interactions of electrons with a local electric field, which has an influence on the plasmon enhancement and subsequently the Raman spectrum. For example, Lambert reported that the Raman shift observed for CO on a Pt electrode can shift by 30  $\text{cm}^{-1}/\text{V}$  when exposed to a potential<sup>57</sup>. In addition to the shift, the peak is also much more intense than at any measured pH during the calibration. In the work of Kwon *et al.*<sup>58</sup>, they notice a similar trend for the  $\text{COO}^-$  stretching vibration of benzoic acid adsorbed on a silver electrode. When applying a potential, the peak becomes one of the most intense peaks in the surface-enhanced Raman spectrum, whereas adsorption on a silver sol (dilute silver suspension) causes the peak to have a rather weak intensity. They claim that because the surface complexes are reported to be excited by a charge transfer mechanism, 'the intensification of the  $\text{COO}^-$  stretching band upon the potential lowering may be understood in terms of the availability of charge transfer excitation'. This might also be the reason for the significant peak increase for 4-MBA when applying a negative potential, as seen in this work.

Taking this effect into consideration, we decided to avoid using the  $1380\text{ cm}^{-1}$  peak as its reproducibility during electrochemical events could not be guaranteed, and focused on the  $1580\text{ cm}^{-1}$  peak trend instead.

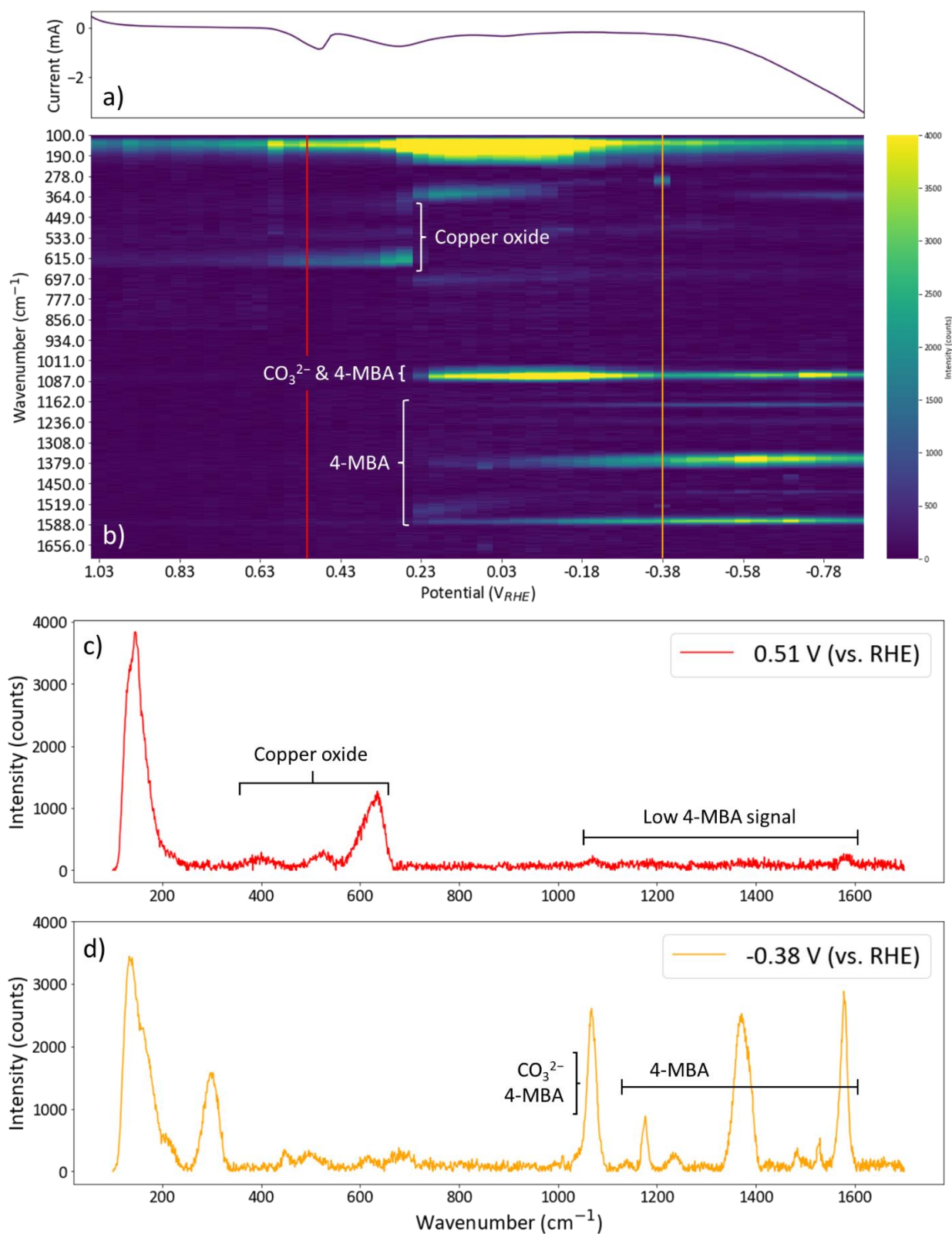
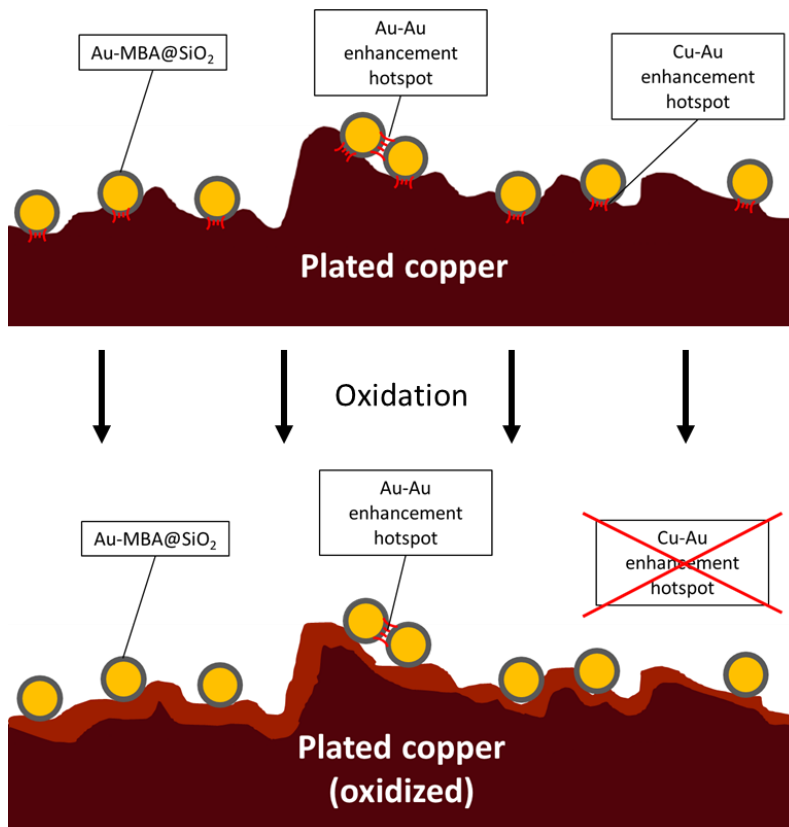


Figure 35. Second cycle in the Raman-cyclic voltammetry (RCV) measurement for the 4-MBA probe. a) Chronological I/V diagram of the second reductive cycle of the CV, from most positive to most negative potential. b) Heatmap of the Raman spectrum at different potentials. The red and orange lines indicate the positions of the spectra in c and d. c, d) Raman spectra at 0.51 V and  $-0.38\text{ V}$  (vs. RHE) respectively, during the 2<sup>nd</sup> cycle of the CV.



Strong Raman signal from probe

Weak Raman signal from probe

Figure 36. Possible cause of enhancement loss upon surface oxidation of copper electrode. The Cu-Au hotspots disappear when a copper oxide layer is formed.

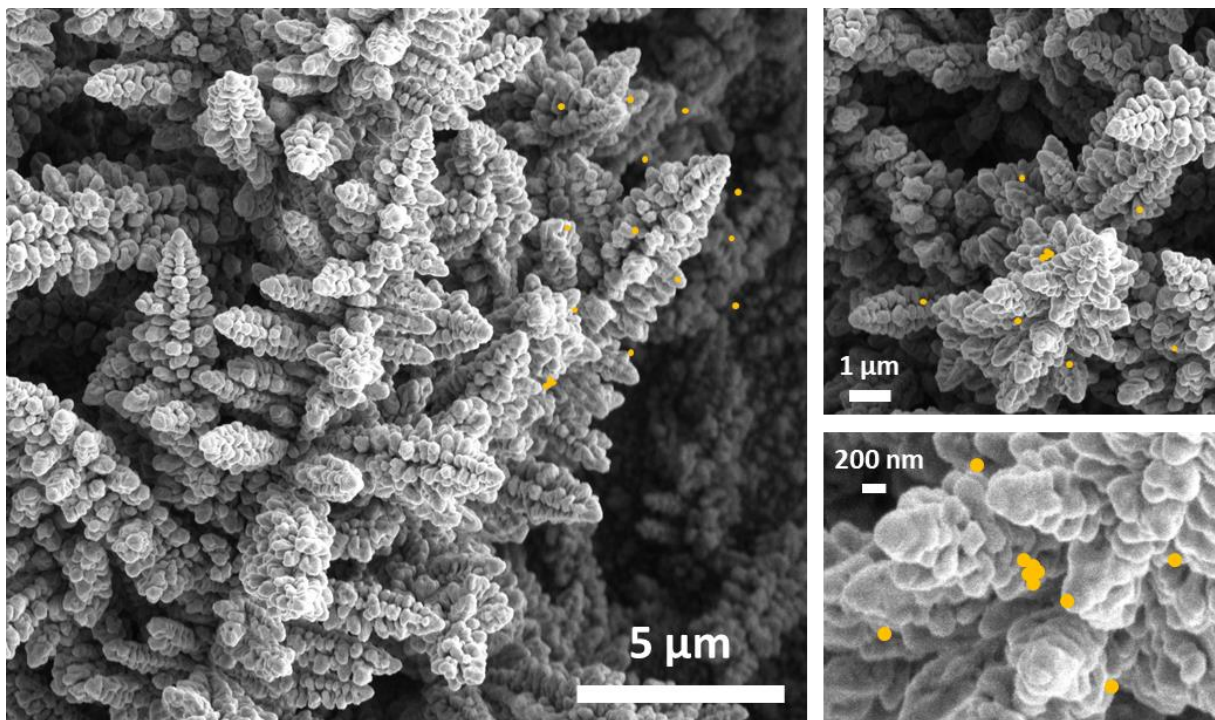


Figure 37. SEM image of a plated copper electrode. The added illustrated yellow dots are 100 nm in diameter and represent the nanoprobe adsorbed on the copper. It can be seen that the dendrites on the copper are much larger than the SHINs, so copper oxide formation could possibly cover the probes and distort the Raman signal.

As determined with the calibration curve and according to literature<sup>19</sup>, the  $1580\text{ cm}^{-1}$  peak shift can also be used to measure the local pH. However, as the above discussed experiment has a time

resolution of 4 seconds and also featured quite noisy spectra, a follow-up measurement was performed to acquire results with a better time resolution. The CV settings were unchanged, but the Raman spectra were recorded in a narrower wavenumber range and with two accumulations instead of one, resulting in a time resolution of 2 seconds as well as stronger signals. In Figure 38, the results are depicted similarly to the previous experiment. It can be seen that the  $1580\text{ cm}^{-1}$  peak redshifts with more negative potentials and shifts back to higher wavenumbers when returning to positive potentials. When looking at the calibration curve in Figure 31, it is clear that a shift to higher wavenumbers corresponds to an increase in pH. Consequently this means that with more negative potentials (and thus with increasing  $\text{CO}_2$  reduction), the pH increases. This is related to  $\text{OH}^-$  formation due to  $\text{CO}_2$  reduction. To further correlate peak shift to pH, the peak wavenumber is plotted against potential in Figure 39. Even though it is possible to roughly see the peak wavenumber shift during the measurement, the spread is too large to correlate these results to a numerical pH value. The main reason for this is that the probe is active in medium pH region, which is unsuitable for the alkaline electrochemical environment that these measurements were performed in. Additionally, the range of peak wavenumbers is between  $1577$  and  $1591\text{ cm}^{-1}$ , whereas the calibration curve only features peaks between  $1584$  and  $1590\text{ cm}^{-1}$ . One explanation for this is the noise in the spectra during the CV measurement. Another explanation is the fact that the electronic effects introduced by an applied potential can cause peak shifts too (Stark effect<sup>57</sup>). Solutions for these problems include the determination of a calibration curve during electronic potentials and spectral correction for the electronic effects, but even then the sensitivity of the 4-MBA pH probe (pH 6-8) would not be optimal for the application in the  $\text{CO}_2$  electroreduction (pH 7-12). Therefore, we shifted our focus towards the 4-MP probe, which has better sensitivity in alkaline environments.

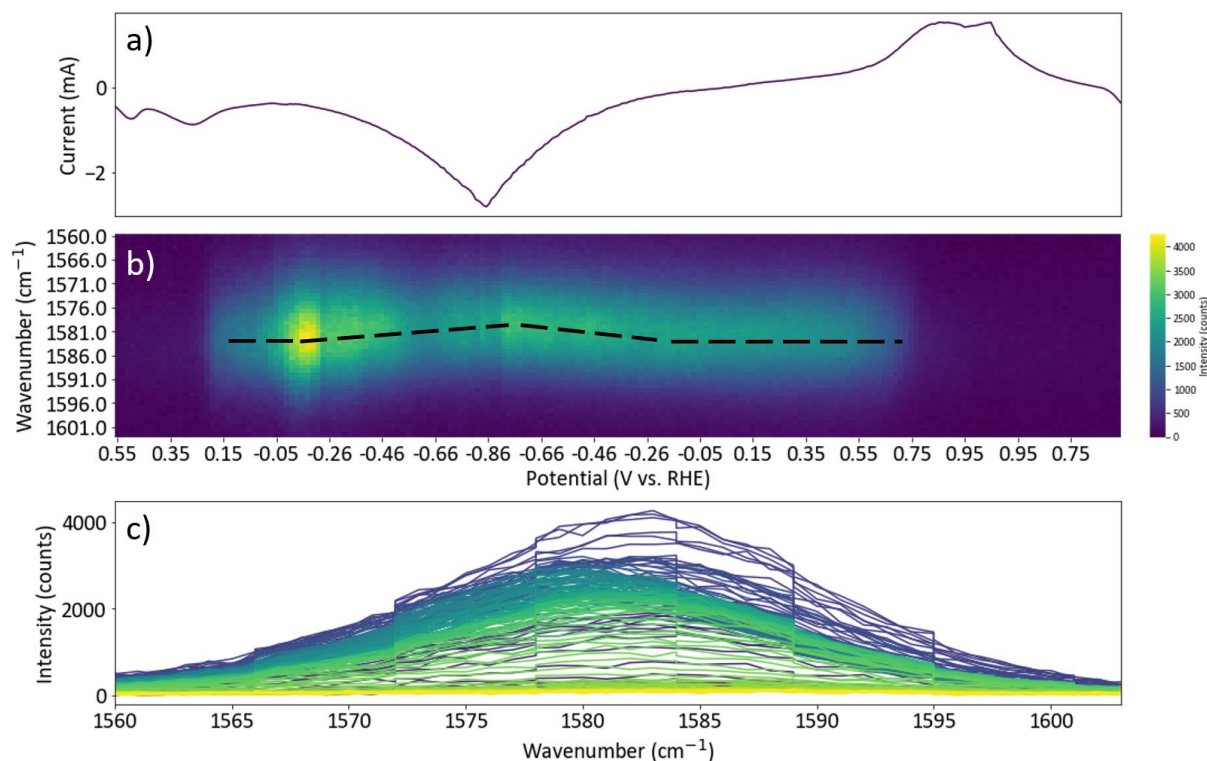


Figure 38. Second cycle of the RCV measurement using the 4-MBA probe. a) I/V curve of the 2<sup>nd</sup> cycle. b) Heatmap of Raman spectra dependence on potential. The central position is roughly indicated by the black dotted line. Note how the intensity reversibly shifts to lower wavenumbers at more negative potentials. c) Development of the pH-dependent C-C stretching vibration peak at  $1580\text{ cm}^{-1}$ . The same trend as in b) is visible.

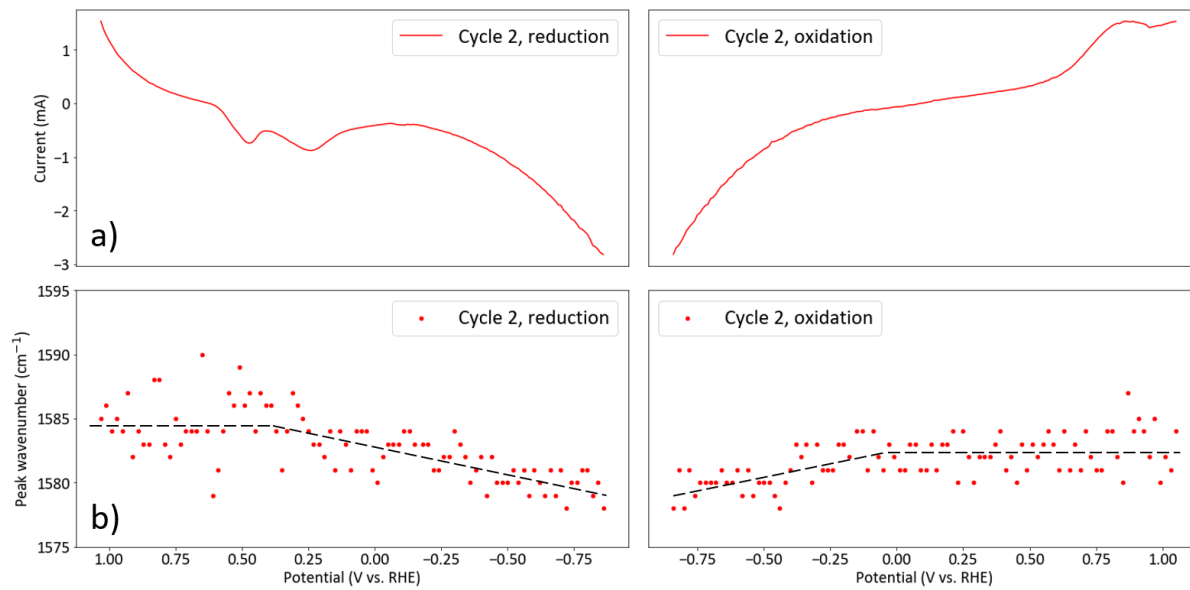


Figure 39. a) I/V curve of reduction (left) and oxidation (right) during the RCV measurement. b) 1580 cm<sup>-1</sup> peak wavenumber at given potentials. A black dotted line indicates the trend.

#### 4.3.2 Application of the Au-MP@SiO<sub>2</sub> probe

For the 4-MP probe, Raman-cyclic voltammetry (RCV) measurements were also performed to get an indication of its effectivity in electrochemical environments. Polished (flat) copper was used instead of plated (rough) copper in an effort to reduce the signal distortion by copper oxide. Less surface area means less copper oxide formation, but also leads to fewer reactions. As a consequence, the I/V curves of the CV feature lower peaks, as visible in Figure 40. The RCV measurement can be found in the appendix (Figure 51). To determine the pH from these measurements, we used all four intensity-based trends found in the pH calibration curve, the results of which are visible in appendix Figure 52-Figure 55. In the plots, it can be seen that the measurements had many outliers, which is because of the low signal to noise ratio. This makes it hard to draw definite conclusions from this experiment. For example, for the 2<sup>nd</sup> cycle in the 1473/1485 cm<sup>-1</sup> peak ratio plot (appendix Figure 53), the ratio is the highest at oxidative potentials and then decreases with reductive potentials. Looking at the 3<sup>rd</sup> cycle, however, the ratio is highest for both negative and positive potentials. The reason for these results can only be ascribed to the low Raman signal of the probe during the measurement, which complicates the interpretation of the spectra.

Only the 995/1005 cm<sup>-1</sup> peak ratio shows an increase with more negative potentials. When comparing this to the calibration curve for 4-MP in Figure 33, it indicates that CO<sub>2</sub> reduction results in a pH increase. As all peak ratios should have the same trend, this experiment suggests that the peaks at 995 cm<sup>-1</sup> and 1005 cm<sup>-1</sup> (assigned to ring breathing modes) might be least affected by the applied potential. We therefore argue that the reason for the deviation in the other peak ratios is due to the external electronic effects on the Raman signals suppressing the intensity of selected vibrations and subsequently adversely affecting the pH-dependency of the peaks. Follow-up experiments have been conducted to investigate this hypothesis later in this work (page 44).

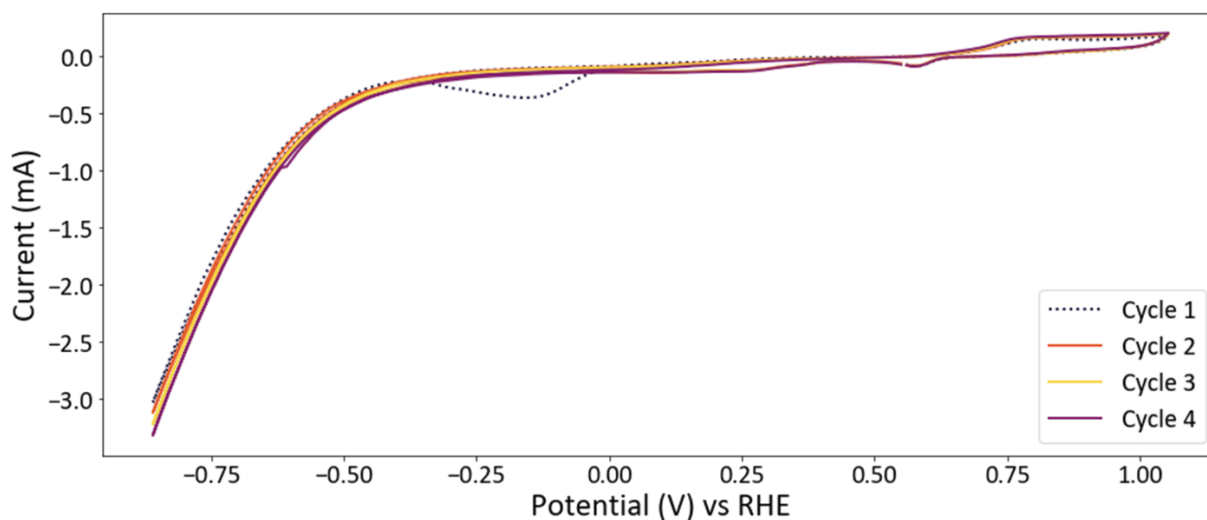


Figure 40. I/V diagram for the Raman-CV measurement for the 4-MP pH probe on polished copper.

After the cyclic voltammetry measurements yielded indefinite results for the 4-MP probe, the focus was shifted to more static measurements at reductive potentials, such as chronoamperometry and pulsed electrolysis, to mainly gain information about the local pH during CO<sub>2</sub> reduction. By avoiding oxidation of the surface, the probe signal is retained throughout the measurement, as no copper oxide is present to distort the Raman signal. For the first follow-up measurement we performed, we again used our 4-MP probe on a polished copper electrode in a CO<sub>2</sub>-saturated 0.1M KHCO<sub>3</sub> solution electrolyte (pH = 6.8). A potential of -0.35 V (vs. RHE) was applied for 300 seconds, and Raman spectra were collected before, during and after the reduction. One spectrum was taken every 5 seconds, and the results are visible in Figure 41.

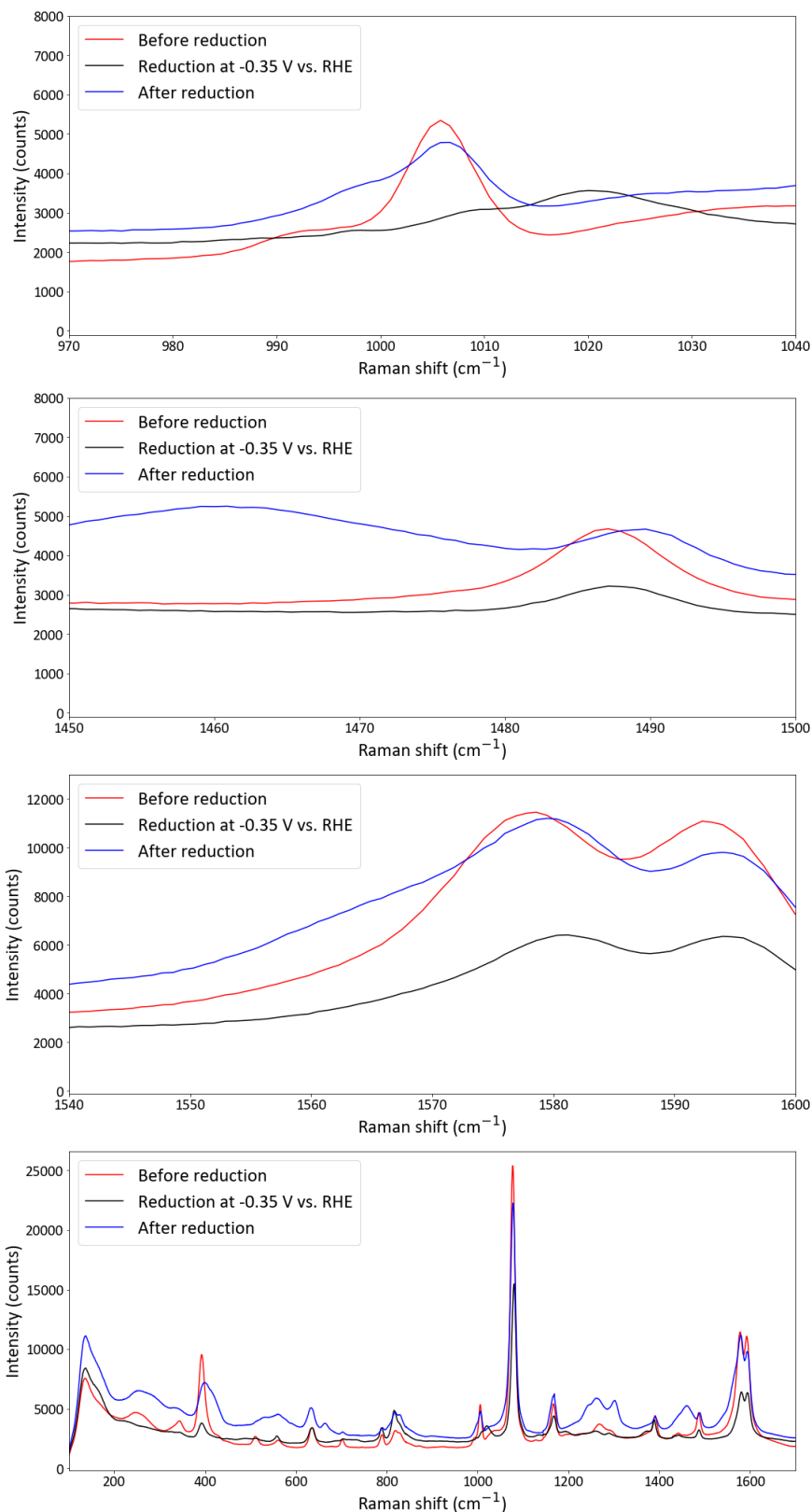


Figure 41. Averaged spectra of the relevant peaks during the static potential measurement. 10 spectra were taken before and after the reduction, and 50 spectra were collected during the reduction.

It appeared that the relevant pH-dependent peak ratios were highly dependent on potential, as they underwent significant changes when a potential was applied. In Figure 42, it can be seen that for the 1578/1595 cm<sup>-1</sup> peak ratio, the ratio gets suppressed during reduction, whereas the opposite happens for the 993/1005 cm<sup>-1</sup> peak ratio. When looking at the calibration curves in Figure 33, higher peak

ratios mean higher pH, which in turn indicates that pH increases after reduction. However, this would also mean that during the reduction the pH temporarily decreases, but  $\text{CO}_2$  reduction should increase the pH due to  $\text{OH}^-$  formation. Therefore, it is assumed that the peaks used in the ratios are not only pH-dependent, but also potential-dependent. This is problematic, as this means that pH cannot be determined directly from the peak ratios during electrochemical reactions. What we can do is compare the ratios before and after applying the potential to see how the pH has changed. From Figure 42, it can be concluded that the  $993/1005\text{ cm}^{-1}$  peak ratio has increased from around 0.4-0.5 before the reduction to around 0.7 after the reduction. Comparing this to the values in the calibration curve indicates a pH increase from approximately 10-11 to 11-12. Using the  $1578/1595\text{ cm}^{-1}$  trend, the pH increases to a maximum of 11. This is, however, only a rough estimate as the spread of the ratio is too large to accurately determine the pH. Also the pH should be around 7 at the start of the measurement, as that is the pH of a 0.1M  $\text{CO}_2$  saturated  $\text{KHCO}_3$  solution, which is in conflict with what the probe reports (pH 10-11). Additionally, an slow increase in ratio before and after reduction is apparent. This could be because the system is not yet in equilibrium, and pH is slowly increasing. Taking these factors into consideration, these results are too unreliable for tracking of local pH behavior on the surface of the electrode, but still provide a starting point for follow-up experiments (next page) and also provide insight into the electronic effects of reductive potentials on Raman signals.

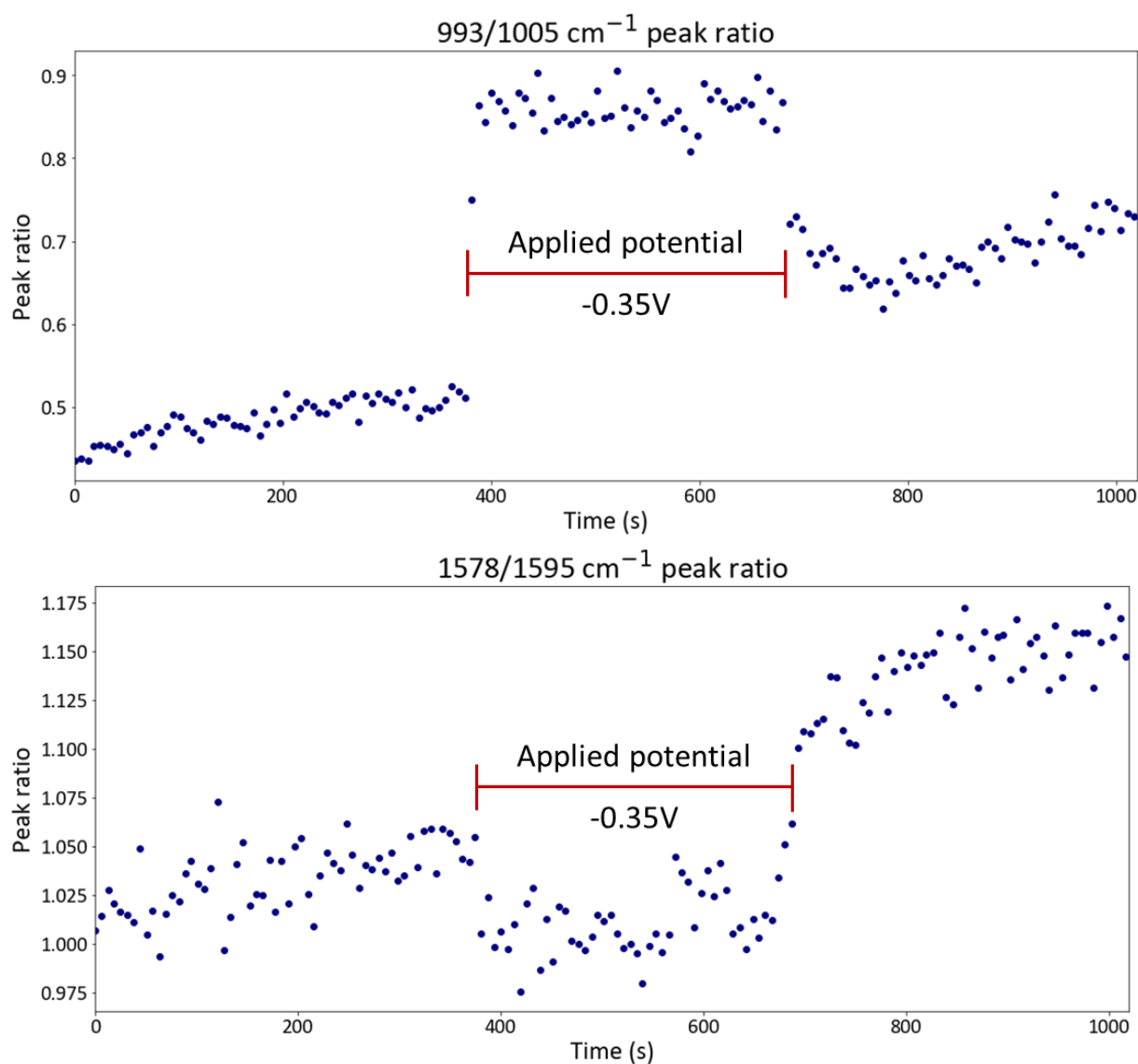


Figure 42. Peak ratio developments for the 4-MP probe on polished copper before, during and after applying a reductive potential of  $-0.35\text{ V}$  (vs. RHE). Potential applied between  $t=390$  and  $t=690$ . Higher ratios mean higher pH, according to the calibration curve. The remaining ratios are attached in the appendix (Figure 56).

To further investigate the effects that an applied potential has on enhanced Raman spectroscopy, an extensive Raman-electrochemical experiment was conducted. For six electrolytes with different pH (6.8, 8.6, 9.0, 10.0, 11.5, 12.1), we measured Raman spectra during five different reductive potentials ( $-0.75$ ,  $-0.65$ ,  $-0.55$ ,  $-0.45$ ,  $-0.35$  V vs. RHE), that were applied for 5 minutes each. Additionally, several spectra were collected before and after applying the potential. It appeared that the pH-dependent peaks at around  $1580\text{ cm}^{-1}$  clearly changed with changing potential during reduction. In Figure 43, a close-up of the peaks of the averaged Raman spectra during the 5 minutes of reduction are depicted. From left to right (so with increasing pH), the peak changes are similar to the calibration curve. However, from top to bottom (decreasing reductive potential), peak changes are apparent as well. In Figure 44, the  $1568/1595\text{ cm}^{-1}$  peak ratios (note that peaks undergo a small blueshift during reduction) at different potentials are plotted against pH (results before and after reduction can be seen in appendix Figure 57). It can be seen that during all potentials the ratio goes up with increasing pH, but when comparing the curves for  $-0.45$  V and  $-0.75$  V, it is clear that there is a significant discrepancy in the shape of the curve. This confirms that the spectral changes used for our pH probe are also directly affected by the applied potential. A reason for this effect could be the strength of enhancement that might change with different potentials because of electronic interactions with the localized surface plasmons. However, as not only the signal intensity but peak ratios are affected as well, the enhancement might also be stronger or weaker for specific vibrations only, which translates to the peak ratios being significantly and unexpectedly lower during electroreduction. This considerably complicates the probing of pH during electroreduction of  $\text{CO}_2$ , which is the reason that we focused on determining the pH-change from before and after spectra instead. However, when comparing the before and after spectra (Figure 58, see appendix), it became apparent that the peak ratio (and therefore pH) actually slightly decreases, as is the case during the reduction. We ascribe this to the electrode surface still retaining some charge after stopping the reductive potential, which was evidenced by the continuous measurements of the potentiostat. As the ratio during reduction is much lower than expected, it is logical that a somewhat negatively charged surface also features slightly suppressed Raman signals and therefore lower ratios. Therefore, the following experiment was conducted similarly, but this time with a potential close to the open-circuit potential ( $V_{\text{oc}}$ ) applied before and after the reduction in order to account for the negative bias that is left on the surface after reduction. Because the potential applied is almost the same as the  $V_{\text{oc}}$ , it can be assumed that no reactions are happening during this time.

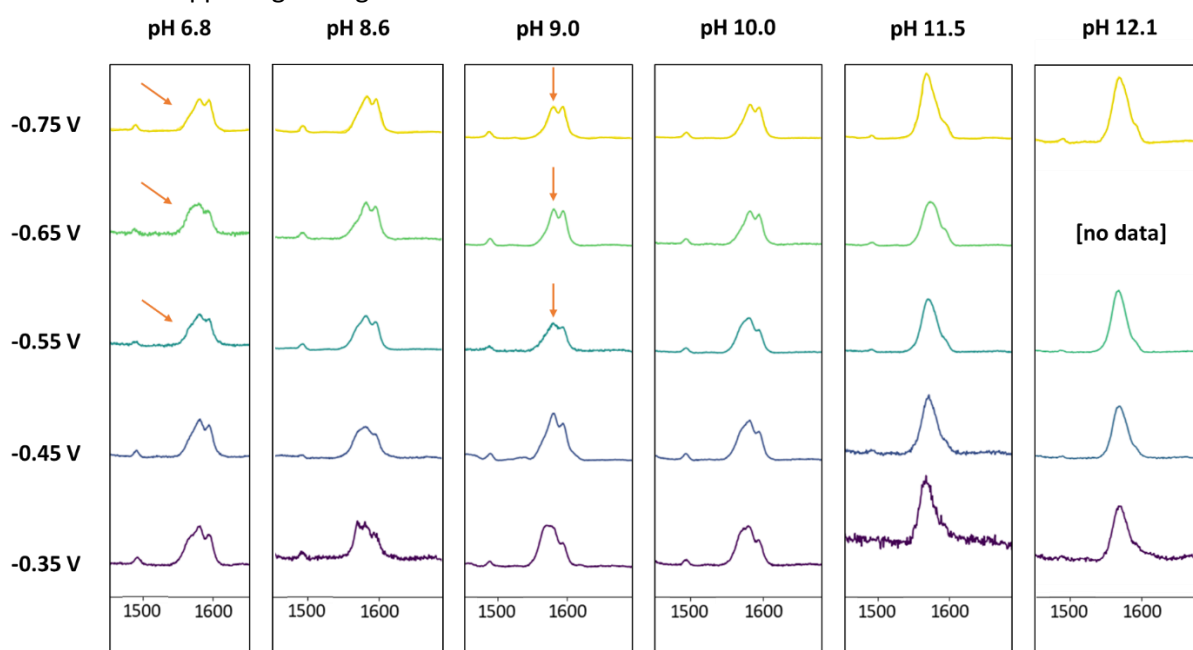


Figure 43. The pH-dependent peaks around  $1580\text{ cm}^{-1}$  of averaged Raman spectra at given pH and potentials (in V vs. RHE). Note how the peaks change even though bulk pH stays the same (some trends indicated by arrows).

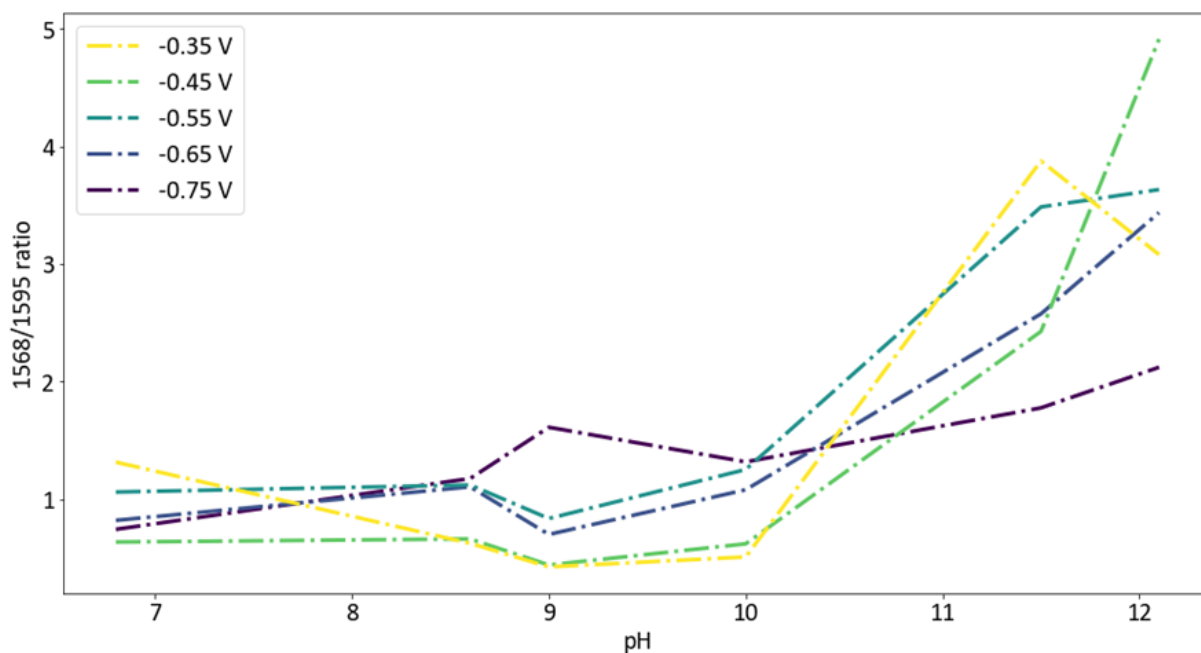


Figure 44. The 1568/1595  $\text{cm}^{-1}$  peak ratio development during electroreduction at given potentials in electrolytes with different pH. Note the different shapes of the curves, indicating that applying a potential has a significant effect on the Raman spectra.

For the next experiment, a potential of 0.55 V (vs. RHE) was applied for 300 seconds, prior to 300 seconds of reduction at  $-0.55$  V (vs. RHE). The open circuit potential was approximately 0.65 V, so it was assumed that no reactions would occur at 0.55 V. After the reduction, a potential of 0.55 V was again applied in an effort to measure pH differences before and after reduction while eliminating the charge effects. During the potentials, a Raman spectrum was collected every 6 seconds, and the peaks around  $1560\text{--}1600$   $\text{cm}^{-1}$  in the averaged spectra are visible in appendix Figure 59.

In Figure 45, the 1568/1595  $\text{cm}^{-1}$  peak ratio is shown as a function of time. Once again, it can be seen that the ratio is much lower during the reduction, which supports the hypothesis that certain peaks are suppressed at negative potentials. We ascribe this suppression to the effects of a charged surface on the electronic properties of the aromatic ring of 4-MP. As the peaks at  $1568$  and  $1595$   $\text{cm}^{-1}$  are assigned to aromatic ring vibrations, it follows that their ratio is affected as well. In the work of Heo *et al.*, it is found that applied voltages on an aromatic structure can have an effect similar to electron-withdrawing or electron-donating groups, which is called the electro-inductive effect<sup>59</sup>. This means that the reactivity of the adsorbed molecule (4-mercaptophenol) can change with applied potential and changes in the Raman spectrum might therefore result from unwanted side-reactions involving the probe molecule.

Even though pH determination from the peak ratio is complicated (due to multiple effects) during the reduction, it can still be monitored before and after. In Figure 45, it is visible that the peak ratio increases from approximately 1.5 to 4, which would correspond to a pH increase of about 11–12 to about 13–14, when comparing with the calibration curve in Figure 33. Once again, the probe-reported initial pH is unusually high, as the pH should be 6.8 at the start. Still, the measurement indicates that the pH increases after reduction, which is expected. What also stands out in the plot is the apparent peak ratio increase prior to the reduction. A possible explanation is that after several minutes in the electrolyte, the way 4-MP is adsorbed is adjusted, which influences its polarizability and thereby its Raman signal. Finally, it appears that the ratio does not seem to decrease after removing the potential, which would be expected, because of  $\text{OH}^-$  diffusion away from the surface when  $\text{CO}_2$  reduction ( $\text{OH}^-$  formation) is stopped. This indicates that either the  $\text{CO}_2$  bubbling (acidification) cannot compete with the pH increase, or the  $\text{OH}^-$  does not diffuse quickly enough. Both are unlikely when taking into

consideration that the collection of Raman spectra after reduction took more than half an hour. This would be enough time for  $\text{CO}_2$  to bubble through the electrolyte and for  $\text{OH}^-$  to diffuse from the surface. Therefore, the probe was most likely not functioning properly during this time.

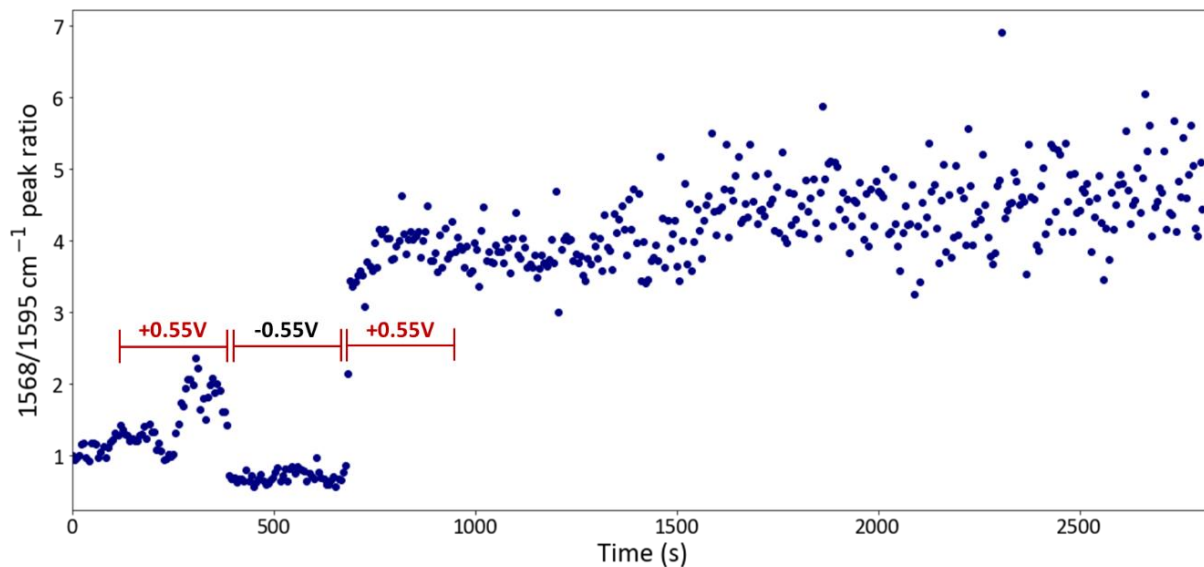


Figure 45. The  $1568/1595\text{ cm}^{-1}$  peak ratio before, during and after reduction at  $-0.55\text{ V}$  (vs. RHE). The regions of  $V_{oc}$  and reduction are indicated and represent 300 seconds each. Raman spectra were taken every 6 seconds.

After these experiments, we got an idea of how certain reduction potentials affect the peak ratios, and with that the pH. In a follow-up measurement (using the same electrolyte and copper piece), we tried to investigate the effects of applying different subsequent reductive potentials. Similar to the last procedure, we again applied a potential close to the open circuit potential ( $0.55\text{ V}$  vs. RHE) for 300 seconds before and after applying a negative potential of  $-0.35\text{ V}$  (vs. RHE), also for 300 seconds. Then, potentials of  $-0.55\text{ V}$ ,  $-0.75\text{ V}$  and  $-0.95\text{ V}$  (vs. RHE) were applied for 300 seconds each, while every time applying  $0.55\text{ V}$  for 300 seconds before and after the reduction. Spectra were collected every 6 seconds, the 50 spectra during every potential window were averaged and the peak ratios were collected in a bar diagram (Figure 46). As usual, it can be seen that the ratios during reduction are much lower than when a potential near the  $V_{oc}$  is applied. The differences between the varying negative potentials are not very significant, as the maximum deviation is only 0.2 (ratio). Additionally, the peak ratio (and thereby pH) is lowest at the strongest reduction potential, even though more reduction reactions take place and more  $\text{OH}^-$  should be formed. This supports the hypothesis that reductive potentials have a substantial effect on the Raman peaks used for pH determination. When looking at the peak ratios at potentials of  $0.55\text{ V}$ , the pH starts at around 13 (ratio = 2.5) and drops down to around 11.5 (ratio = 0.8). The high starting pH is probably due to the preceding measurement (Figure 45), as the ratio at the end of that measurement was around 4, which correlates to a pH of around 13. The decrease after applying  $-0.35\text{ V}$  might be due to the mild reduction potential not forming as much  $\text{OH}^-$ , and the bubbling  $\text{CO}_2$  in combination with diffusion of  $\text{OH}^-$  can compensate causing a decrease in pH. Then, after  $-0.55\text{ V}$ , the ratio increases significantly, which could be because of the  $\text{OH}^-$  formed from  $\text{CO}_2$  reduction. However, as the ratios decrease again after even stronger reductive potentials ( $-0.75\text{ V}$  and  $-0.95\text{ V}$ ), we think that the ratios are influenced by differences in enhancement rather than fluctuations in pH. This could be confirmed in a follow-up measurement where potential is the only variable. An example is to avoid  $\text{CO}_2$  being present in the electrolyte. This way, no  $\text{CO}_2$  reduction takes place, no  $\text{OH}^-$  is formed and pH is roughly constant. All results therefore point out the difficulty in accurate probing of local pH during electrochemical reduction of  $\text{CO}_2$ .

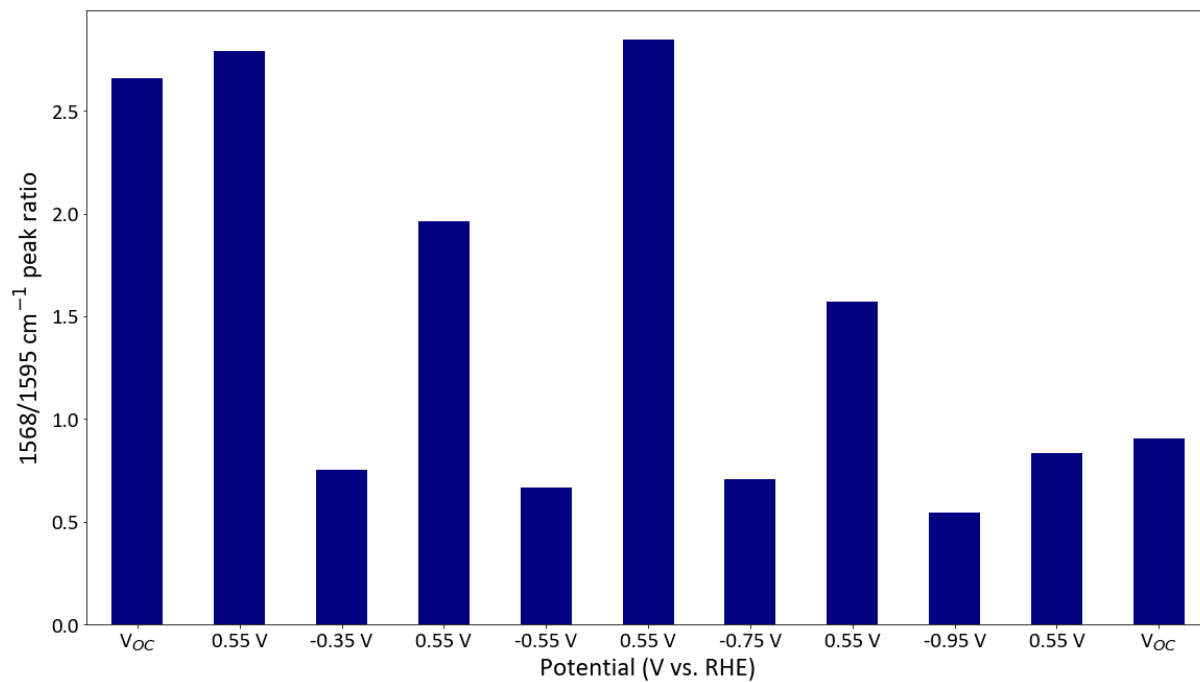


Figure 46. Average  $1568/1595 \text{ cm}^{-1}$  peak ratios for each of the indicated applied potentials for the 4-MP probe. Every bar represents the peak ratio derived from the average of 50 spectra taken over 300 seconds.

## 5 Conclusions

Two pH probes based on Raman reporter-functionalized gold nanoparticles were successfully synthesized. The Raman reporters used were 4-mercaptobenzoic acid and 4-mercaptophenol. Both probes were synthesized by adsorption of the Raman reporter on gold nanoparticles which was followed by coating of a thin silica layer using tetraethyl orthosilicate (TEOS) hydrolyzation. Resulting pH probes had a size of approximately 90 nm with a silica coating of approximately 1-3 nm. The 4-mercaptobenzoic acid (4-MBA) probe was found to be sensitive in a pH region of 6 to 8, whereas the other probe (4-mercaptophenol, 4-MP) had a sensitivity of pH 10 to 14.

We used the probes to track the local pH on a copper surface during electrochemical reduction of CO<sub>2</sub> in a CO<sub>2</sub>-saturated potassium carbonate solution electrolyte. As the pH of this solution is 6.8, the 4-MBA probe pH sensitivity was too low and the 4-MP probe pH sensitivity was too high, as pH changes from 7 to 12 were expected. Still, the 4-MBA pH probe indicated an increase in pH when applying negative potentials (from -0.5 V to -0.85 V vs. RHE), as well as an immediate decrease in pH upon reversing the scan direction (from -0.85 V to -0.5 V vs. RHE) during cyclic voltammetry measurements. Because of this subsequent decrease in pH, it was concluded that the measured pH was indeed local, and the decrease happened because of OH<sup>-</sup> diffusion away from the surface. As CO<sub>2</sub> reduction reactions form OH<sup>-</sup> as a side product, these results are in agreement with expected pH behavior. Quantitative values for the pH could not be collected, because of the probe's inability to accurately track pH values higher than 8.

The 4-MP pH probe was also used in electrochemical environments, but the pH-dependent Raman peaks in its spectrum appeared to be heavily influenced by the applied reductive potential. We have ascribed this to changes in adsorption due to interactions between the probes and the charged surface, which influence the polarizability and hence the Raman signal of the 4-MP. A different strategy to measure local pH was therefore applied for this probe, where we measured the spectra before and after reduction, rather than during reduction. This led to ambiguous results, as some measurements indicated an increase in pH, but other results showed a decrease.

In conclusion, we managed to gain more insight into the behavior of SERS and SHINERS during electrochemistry. The knowledge gained in this work can be of significant use for follow-up measurements.

## 6 Outlook

In future work, the probes synthesized in this work can very well be used in environments outside of electrochemistry. That way, the influence of applied potentials on the pH-dependent peaks is eliminated, so that the ratios of the 4-mercaptophenol-based probe can be accurately correlated to pH. However, systems where the extremely basic sensitivity of 4-MP is useful might be hard to find. To make the probes suitable for electrochemical environments, an idea is to deconvolute pH and electric potential effects. If a clear trend is found in electronic effects on the spectrum, this could be used to correct the signals during CO<sub>2</sub> reduction and enable pH tracking on the surface of the electrode.

Additionally, the synthesis that we used for probe synthesis can easily be expanded to other pH-dependent Raman reporters. When a molecule with a more fitting sensitivity is found (around 7-13), the spectral changes might be more defined at certain pH. Other probe molecules should have similar functional groups as the probes discussed in this work, namely a thiol or amine group to bind to the gold and a pH sensitive group (with a pK<sub>a</sub> around 10). Preferably, the Raman reporter also has an aromatic ring structure, as these vibrations give rise to strong Raman signals. An example of a molecule that might work is 4-mercaptopyridine, as the nitrogen atom gives rise to both pH-sensitivity and resonance structures. This would mean that the ring vibrations change with protonation, and might cause a peak shift dependent on pH. The pK<sub>a</sub> of 4-mercaptopyridine is 8.86<sup>59</sup>, so its pH sensitivity should

be around that point. A problem with this probe, however, is that the aromatic ring could encounter the same problems as the previously used probes, as aromatic structures are electronically affected by potential. A solution for this could be to add several CH<sub>2</sub> groups in between the thiol and the aromatic ring, to slightly isolate the ring from the surface charge. More research is necessary to investigate the suggested probe.

In this work, we also briefly explored another way of pH probing, based on fluorescence, for which we used so-called 'carbon quantum dots' (CQDs). In collaboration with dr. Y. Ganjkhanlou, several different kinds of CQDs were tested for pH sensitivity, but no apparent pH-dependent trend was found and they were therefore unsuitable for further use in this research. However, with a few adjustments to the functional groups of these carbon quantum dots, these probes could possibly be successfully applied in electrochemistry.

## 7 Acknowledgements

I want to thank Jim de Ruiten MSc. for his excellent daily supervision and personal guidance throughout the project, but also for the great laughs we had during the past year. Also, I'd like to thank dr. Ward van der Stam for the supporting feedback he provided me with during this time, as he has often led me towards the right direction for my research. Additional thanks go to Thimo Jacobs MSc. for making the TEM images provided in this thesis, and to the entire ICC electrobuzz team for the interesting discussions and suggestions during the meetings. Lastly, I want to thank dr. Danny Broere for taking the time for being my second examiner and thereby making sure that I can complete my project.

## 8 References

1. *IPCC Climate Change 2014: Synthesis Report. Contribution of Working Groups I, II and III to the Fifth Assessment Report of the Intergovernmental Panel on Climate Change* (eds. Core Writing Team, Pachauri R.K. & Meyer L.A.). IPCC (2014).
2. Jovanov, Z. P., Hansen, H. A., Varela, A. S., Malacrida, P., Peterson, A. A., Nørskov, J. K., Stephens, I. E. L. & Chorkendorff, I. Opportunities and challenges in the electrocatalysis of CO<sub>2</sub> and CO reduction using bifunctional surfaces: A theoretical and experimental study of Au–Cd alloys. *J. Catal.* **343**, 215–231 (2016).
3. Yang, H., Zhang, C., Gao, P., Wang, H., Li, X., Zhong, L., Wei, W. & Sun, Y. A review of the catalytic hydrogenation of carbon dioxide into value-added hydrocarbons. *Catal. Sci. Technol.* **7**, 4580–4598 (2017).
4. Yan, B., Yang, X., Yao, S., Wan, J., Myint, M. N. Z., Gomez, E., Xie, Z., Kattel, S., Xu, W. & Chen, J. G. Dry Reforming of Ethane and Butane with CO<sub>2</sub> over PtNi/CeO<sub>2</sub> Bimetallic Catalysts. *ACS Catal.* **6**, 7283–7292 (2016).
5. Shaner, M. R., Atwater, H. A., Lewis, N. S. & McFarland, E. W. A comparative technoeconomic analysis of renewable hydrogen production using solar energy. *Energy Environ. Sci.* **9**, 2354–2371 (2016).
6. Kuhl, K. P., Cave, E. R., Abram, D. N. & Jaramillo, T. F. New insights into the electrochemical reduction of carbon dioxide on metallic copper surfaces. *Energy Environ. Sci.* **5**, 7050–7059 (2012).
7. Dunwell, M., Yang, X., Setzler, B. P., Anibal, J., Yan, Y. & Xu, B. Examination of Near-Electrode Concentration Gradients and Kinetic Impacts on the Electrochemical Reduction of CO<sub>2</sub> using Surface-Enhanced Infrared Spectroscopy. *ACS Catal.* **8**, 3999–4008 (2018).
8. Yang, K., Kas, R. & Smith, W. A. In Situ Infrared Spectroscopy Reveals Persistent Alkalinity near Electrode Surfaces during CO<sub>2</sub> Electroreduction. *J. Am. Chem. Soc.* **141**, 15891–15900 (2019).
9. Gattrell, M., Gupta, N. & Co, A. A review of the aqueous electrochemical reduction of CO<sub>2</sub> to hydrocarbons at copper. *J. Electroanal. Chem.* **594**, 1–19 (2006).
10. Ryu, J., Wuttig, A. & Surendranath, Y. Quantification of Interfacial pH Variation at Molecular Length Scales Using a Concurrent Non-Faradaic Reaction. *Angew. Chemie - Int. Ed.* **57**, 9300–9304 (2018).
11. Liu, X., Schlexer, P., Xiao, J., Ji, Y., Wang, L., Sandberg, R. B., Tang, M., Brown, K. S., Peng, H., Ringe, S., *et al.* pH effects on the electrochemical reduction of CO<sub>(2)</sub> towards C<sub>2</sub> products on stepped copper. *Nat. Commun.* **10**, 1–10 (2019).
12. Jeon, H. S., Timoshenko, J., Rettenmaier, C., Herzog, A., Yoon, A., Chee, S. W., Oener, S., Hejral, U., Haase, F. T. & Roldan Cuenya, B. Selectivity Control of Cu Nanocrystals in a Gas-Fed Flow Cell through CO<sub>2</sub> Pulsed Electroreduction. *J. Am. Chem. Soc.* **143**, 7578–7587 (2021).
13. Moura de Salles Pupo, M. & Kortlever, R. Electrolyte Effects on the Electrochemical Reduction of CO<sub>2</sub>. *ChemPhysChem* **20**, 2926–2935 (2019).
14. Kuhl, K. P., Hatsukade, T., Cave, E. R., Abram, D. N., Kibsgaard, J. & Jaramillo, T. F. Electrocatalytic conversion of carbon dioxide to methane and methanol on transition metal surfaces. *J. Am. Chem. Soc.* **136**, 14107–14113 (2014).
15. Hartman, T. Shell-Isolated Nanoparticle-Enhanced Raman Spectroscopy for Heterogeneous Catalysis. (Utrecht University, 2019).

16. Wondergem, C. S. TIME to SHINE: Plasmon-Enhanced Raman Spectroscopy for Catalysis. (Utrecht University, 2019).
17. Barlow, B. C., Guo, B., Situm, A., Grosvenor, A. P. & Burgess, I. J. Shell isolated nanoparticle enhanced Raman spectroscopy (SHINERS) studies of steel surface corrosion. *J. Electroanal. Chem.* **853**, 113559 (2019).
18. Li, J. F., Huang, Y. F., Ding, Y., Yang, Z. L., Li, S. B., Zhou, X. S., Fan, F. R., Zhang, W., Zhou, Z. Y., Wu, D. Y., *et al.* Shell-isolated nanoparticle-enhanced Raman spectroscopy. *Nature* **464**, 392–395 (2010).
19. Scarpitti, B. T., Morrison, A. M., Buyanova, M. & Schultz, Z. D. Comparison of 4-Mercaptobenzoic Acid Surface-Enhanced Raman Spectroscopy-Based Methods for pH Determination in Cells. *Appl. Spectrosc.* **74**, 1423–1432 (2020).
20. Choi, J., Kim, J., Wagner, P., Gambhir, S., Jalili, R., Byun, S., Sayyar, S., Lee, Y. M., MacFarlane, D. R., Wallace, G. G., *et al.* Energy efficient electrochemical reduction of CO<sub>2</sub> to CO using a three-dimensional porphyrin/graphene hydrogel. *Energy Environ. Sci.* **12**, 747–755 (2019).
21. Hori, Y. Electrochemical CO<sub>2</sub> Reduction on Metal Electrodes. *Mod. Asp. Electrochem.* 89–189 (2008) doi:10.1007/978-0-387-49489-0\_3.
22. Atkins, P., Weller, M., Overton, T., Rourke, J., Armstrong, F. *Inorganic Chemistry*. (Oxford University Press, 2014).
23. Nitopi, S., Bertheussen, E., Scott, S. B., Liu, X., Engstfeld, A. K., Horch, S., Seger, B., Stephens, I. E. L., Chan, K., Hahn, C., *et al.* Progress and Perspectives of Electrochemical CO<sub>2</sub> Reduction on Copper in Aqueous Electrolyte. *Chem. Rev.* **119**, 7610–7672 (2019).
24. Calle-Vallejo, F. & Koper, M. T. M. Theoretical considerations on the electroreduction of CO to C<sub>2</sub> Species on Cu(100) electrodes. *Angew. Chemie - Int. Ed.* **52**, 7282–7285 (2013).
25. Kas, R., Kortlever, R., Yilmaz, H., Koper, M. T. M. & Mul, G. Manipulating the Hydrocarbon Selectivity of Copper Nanoparticles in CO<sub>2</sub> Electroreduction by Process Conditions. *ChemElectroChem* **2**, 354–358 (2015).
26. Varela, A. S., Kroschel, M., Leonard, N. D., Ju, W., Steinberg, J., Bagger, A., Rossmeisl, J. & Strasser, P. pH Effects on the Selectivity of the Electrocatalytic CO<sub>2</sub> Reduction on Graphene-Embedded Fe-N-C Motifs: Bridging Concepts between Molecular Homogeneous and Solid-State Heterogeneous Catalysis. *ACS Energy Lett.* **3**, 812–817 (2018).
27. Andor. What are the Basic Principles of Raman Spectroscopy. *Oxford Instruments 7* [https://andor.oxinst.com/learning/view/article/raman-spectroscopy%0Ahttps://web.stanford.edu/class/siw198q/websites/reprotech/New Ways of Making Babies/EthicVoc.htm](https://andor.oxinst.com/learning/view/article/raman-spectroscopy%0Ahttps://web.stanford.edu/class/siw198q/websites/reprotech/New%20Ways%20of%20Making%20Babies/EthicVoc.htm) (2020).
28. Jena. Towards Clinical Translation of Raman Spectroscopy for Tumor Cell Identification. (Friedrich-Schiller-Universität, 2019).
29. Polman, A. & Atwater, H. A. Plasmonics: Optics at the nanoscale. *Mater. Today* **8**, 56 (2005).
30. Michota, A. & Bukowska, J. Surface-enhanced Raman scattering (SERS) of 4-mercaptobenzoic acid on silver and gold substrates. *J. Raman Spectrosc.* **34**, 21–25 (2003).
31. Madzharova, F., Heiner, Z. & Kneipp, J. Surface-Enhanced Hyper Raman Spectra of Aromatic Thiols on Gold and Silver Nanoparticles. (2020) doi:10.1021/acs.jpcc.0c00294.
32. Shin, D., Seo, H. & Jhe, W. Exploring the Hydration Water Character on Atomically Dislocated

- Surfaces by Surface Enhanced Raman Spectroscopy. *ACS Cent. Sci.* **6**, 2079–2087 (2020).
33. Ho, C. H. & Lee, S. SERS and DFT investigation of the adsorption behavior of 4-mercaptobenzoic acid on silver colloids. *Colloids Surfaces A Physicochem. Eng. Asp.* **474**, 29–35 (2015).
  34. Wei, C., Xu, M. M., Fang, C. W., Jin, Q., Yuan, Y. X. & Yao, J. L. Improving the sensitivity of immunoassay based on MBA-embedded Au@SiO<sub>2</sub> nanoparticles and surface enhanced Raman spectroscopy. *Spectrochim. Acta - Part A Mol. Biomol. Spectrosc.* **175**, 262–268 (2017).
  35. Wang, J., Dong, J. C., Yang, J., Wang, Y., Zhang, C. J., Xu, M. M., Mao, B. W., Yao, J. L., Li, J. F. & Tian, Z. Q. In situ SERS and SHINERS study of electrochemical hydrogenation of p-ethynylaniline in nonaqueous solvents. *Electrochem. commun.* **78**, 16–20 (2017).
  36. Ma, C. & Harris, J. M. Surface-enhanced raman spectroscopy investigation of the potential-dependent acid-base chemistry of silver-immobilized 2-mercaptobenzoic acid. *Langmuir* **27**, 3527–3533 (2011).
  37. Stadler J., Schmid T. & Zenobi R. Nanoscale Chemical Imaging Using Top-Illumination Tip-Enhanced Raman Spectroscopy. *Nano Lett.* **10**, 4514–4520 (2010).
  38. Zeng, Z. C., Huang, S. C., Wu, D. Y., Meng, L. Y., Li, M. H., Huang, T. X., Zhong, J. H., Wang, X., Yang, Z. L. & Ren, B. Electrochemical Tip-Enhanced Raman Spectroscopy. *J. Am. Chem. Soc.* **137**, 11928–11931 (2015).
  39. Ray, N. K. & Anderson, A. B. Variations in carbon-oxygen and platinum-carbon frequencies for carbon monoxide on a platinum electrode. *J. Phys. Chem.* **86**, 4851–4852 (1982).
  40. Cushman, C. Anatomy of pH Electrodes. *YSI* <https://www.yei.com/ysi-blog/water-blogged-blog/2019/02/anatomy-of-ph-electrodes> (2019).
  41. Wirnsberger, G., Scott, B. J. & Stucky, G. D. pH sensing with mesoporous thin films. *Chem. Commun.* 119–120 (2001) doi:10.1039/b003995k.
  42. Le Guern, F., Mussard, V., Gaucher, A., Rottman, M. & Prim, D. Fluorescein derivatives as fluorescent probes for pH monitoring along recent biological applications. *Int. J. Mol. Sci.* **21**, 1–23 (2020).
  43. Haiss, W., Thanh, N. T. K., Aveyard, J. & Fernig, D. G. Determination of size and concentration of gold nanoparticles from extinction spectra. *Anal. Chem.* **79**, 4215–4221 (2007).
  44. Li, J. F., Tian, X. D., Li, S. B., Anema, J. R., Yang, Z. L., Ding, Y., Wu, Y. F., Zeng, Y. M., Chen, Q. Z., Ren, B., *et al.* Surface analysis using shell-isolated nanoparticle-enhanced Raman spectroscopy. *Nat. Protoc.* **8**, 52–65 (2013).
  45. Mons, S. Schematic representation of the silica surface: with and without a hydration layer. [https://commons.wikimedia.org/wiki/File:Schematic\\_silica\\_gel\\_surface.png](https://commons.wikimedia.org/wiki/File:Schematic_silica_gel_surface.png) (2007).
  46. Rhodamine 6G. *Sersitive* [https://sersitive.eu/application\\_types/dyes/rhodamine-6g/](https://sersitive.eu/application_types/dyes/rhodamine-6g/).
  47. Monteiro, M. C. O., Jacobse, L., Touzalin, T. & Koper, M. T. M. Mediator-Free SECM for Probing the Diffusion Layer pH with Functionalized Gold Ultramicroelectrodes. *Anal. Chem.* **92**, 2237–2243 (2020).
  48. Piotrowski, P., Wrzosek, B., Królikowska, A. & Bukowska, J. A SERS-based pH sensor utilizing 3-amino-5-mercapto-1,2,4-triazole functionalized Ag nanoparticles. *Analyst* **139**, 1101–1111 (2014).
  49. Li, R., Ji, W., Chen, L., Lv, H., Cheng, J. & Zhao, B. Vibrational spectroscopy and density

- functional theory study of 4-mercaptophenol. *Spectrochim. Acta - Part A Mol. Biomol. Spectrosc.* **122**, 698–703 (2014).
50. Phenols, alcohols and carboxylic acids - pK<sub>a</sub> values. *Engineering ToolBox*  
[https://www.engineeringtoolbox.com/paraffinic-benzoic-hydroxy-dioic-acids-structure-pka-carboxylic-dissociation-constant-alcohol-phenol-d\\_1948.html](https://www.engineeringtoolbox.com/paraffinic-benzoic-hydroxy-dioic-acids-structure-pka-carboxylic-dissociation-constant-alcohol-phenol-d_1948.html) (2017).
  51. Wei, H., Vejerano, E. P., Leng, W., Huang, Q., Willner, M. R., Marr, L. C. & Vikesland, P. J. Aerosol microdroplets exhibit a stable pH gradient. *Proc. Natl. Acad. Sci. U. S. A.* **115**, 7272–7277 (2018).
  52. Wei, H., Willner, M. R., Marr, L. C. & Vikesland, P. J. Highly stable SERS pH nanoprobosc produced by co-solvent controlled AuNP aggregation. *Analyst* **141**, 5159–5169 (2016).
  53. Bishnoi, S. W., Rozell, C. J., Levin, C. S., Gheith, M. K., Johnson, B. R., Johnson, D. H. & Halas, N. J. All-optical nanoscale pH meter. *Nano Lett.* **6**, 1687–1692 (2006).
  54. Phan, H. T. & Haes, A. J. Impacts of pH and Intermolecular Interactions on Surface-Enhanced Raman Scattering Chemical Enhancements. *J. Phys. Chem. C* **122**, 14846–14856 (2018).
  55. Caballero-Briones, F., Artés, J. M., Díez-Pérez, I., Gorostiza, P. & Sanz, F. Direct observation of the valence band edge by in situ ECSTM-ECTS in p-type Cu<sub>2</sub>O layers prepared by copper anodization. *J. Phys. Chem. C* **113**, 1028–1036 (2009).
  56. Klingan, K., Kottakkat, T., Jovanov, Z. P., Jiang, S., Pasquini, C., Scholten, F., Kubella, P., Bergmann, A., Roldan Cuenya, B., Roth, C., *et al.* Reactivity Determinants in Electrodeposited Cu Foams for Electrochemical CO<sub>2</sub> Reduction. *ChemSusChem* **11**, 3449–3459 (2018).
  57. Lambert, D. K. Vibrational Stark Effect of Adsorbates. *Electrochim. Acta* **41**, 623–630 (1996).
  58. Kwon, Y. J., Son, D. H., Ahn, S. J., Kim, M. S. & Kim, K. Vibrational spectroscopic investigation of benzoic acid adsorbed on silver. *J. Phys. Chem.* **98**, 8481–8487 (1994).
  59. Heo, J., Ahn, H., Won, J., Son, J. G., Shon, H. K., Lee, T. G., Han, S. W. & Baik, M. H. Electro-inductive effect: Electrodes as functional groups with tunable electronic properties. *Science (80-. )*. **370**, 214–219 (2020).
  60. 4-Mercaptopyridine. *ChemicalBook*  
[https://www.chemicalbook.com/ChemicalProductProperty\\_EN\\_CB2748207.htm](https://www.chemicalbook.com/ChemicalProductProperty_EN_CB2748207.htm) (2017).

## 9 Appendix

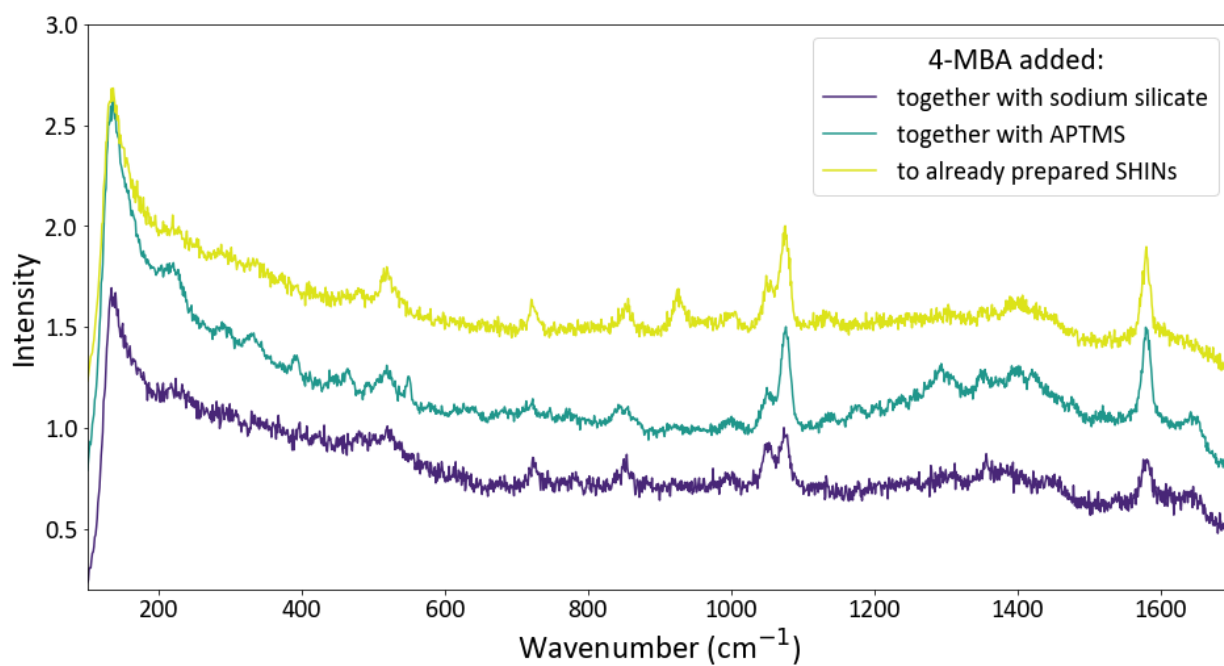


Figure 47. Spectra of Au-MBA@SiO<sub>2</sub> synthesized with APTMS and sodium silicate. It is visible that the signal to noise ratio is low and the 4-MBA spectrum is hardly recognizable.

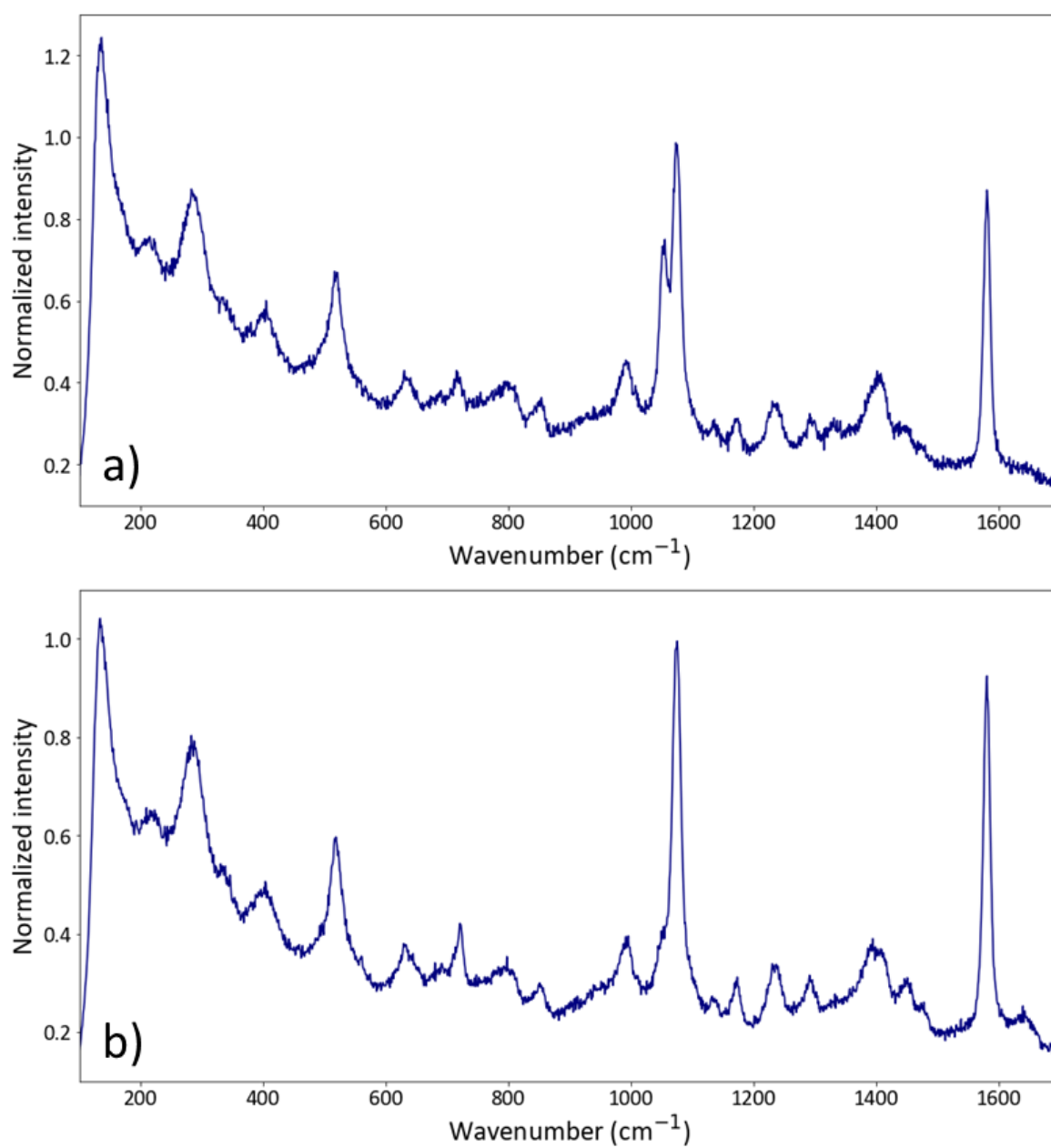


Figure 48. Spectrum of Au-MBA@SiO<sub>2</sub> synthesized with MPTES and sodium silicate, where: a) 10  $\mu$ l 0.03 mM 4-MBA was added 3 minutes before MPTES. b) 20  $\mu$ l 0.03 mM 4-MBA was added 6 minutes before MPTES.

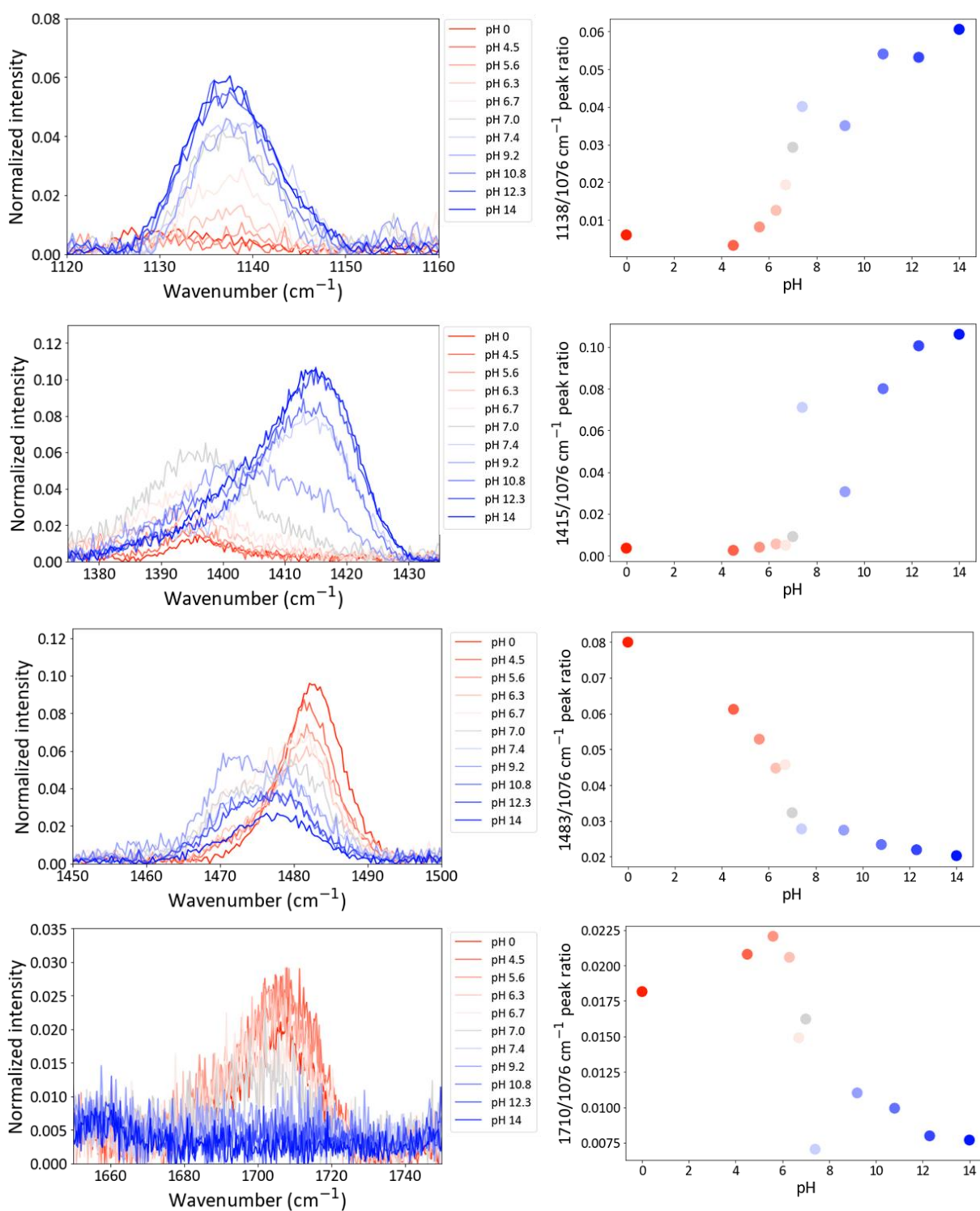


Figure 49. The four intensity-based pH-dependent trends for the 4-MBA pH probe. The results are an average of 11 spectra. It can be seen that the trends are all of less quality than the peak shifting trend (Figure 31).

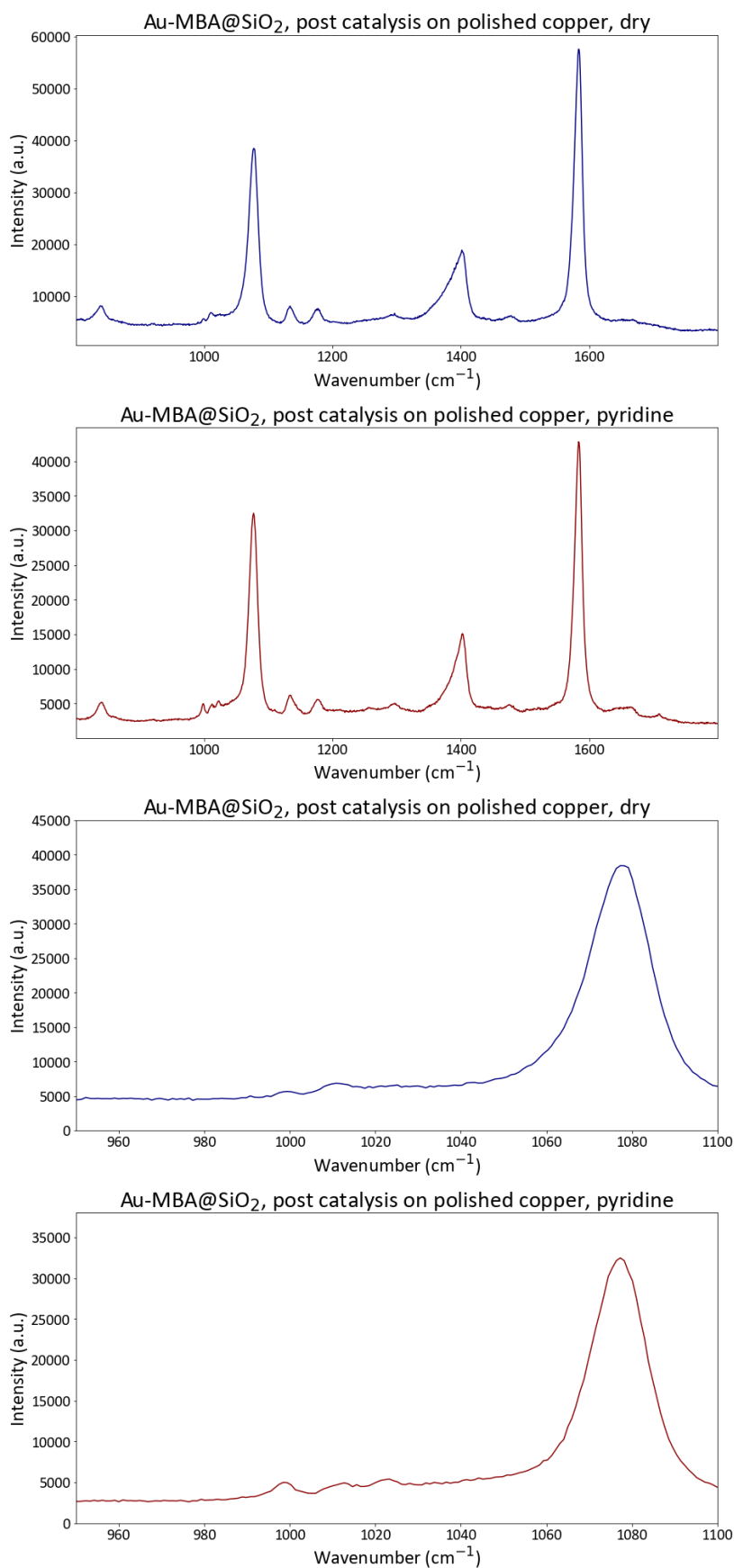


Figure 50. Raman measurements of the 4-MBA probe on polished copper after 4 CV cycles (post-catalysis), including pyridine pinhole test results. The 4-MBA spectrum is still clearly recognizable, indicating the stability of the probes on the copper.

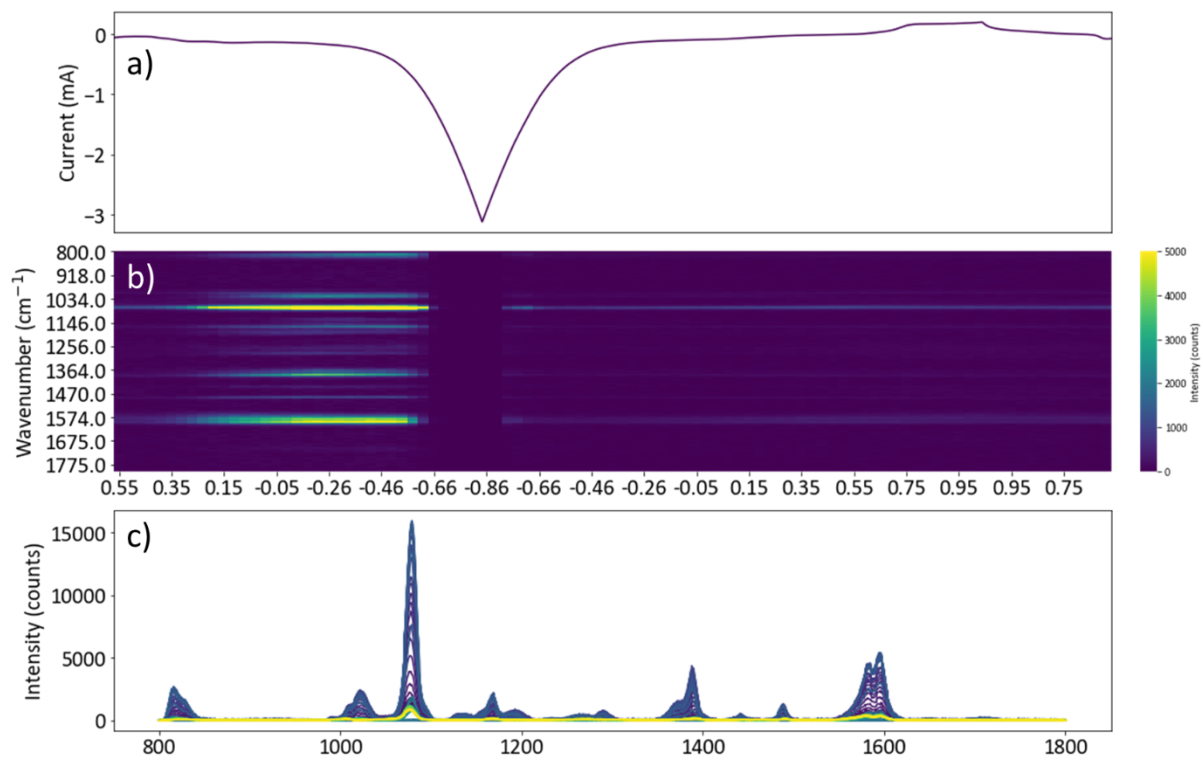


Figure 51. Second cycle of the RCV measurement of the 4-MP probe. a)  $I/V$  curve. b) Heatmap showing spectral development with potential. c) Spectral changes during CV.

Au-MP on polished copper 995/1005 peak ratio at different potentials during CV

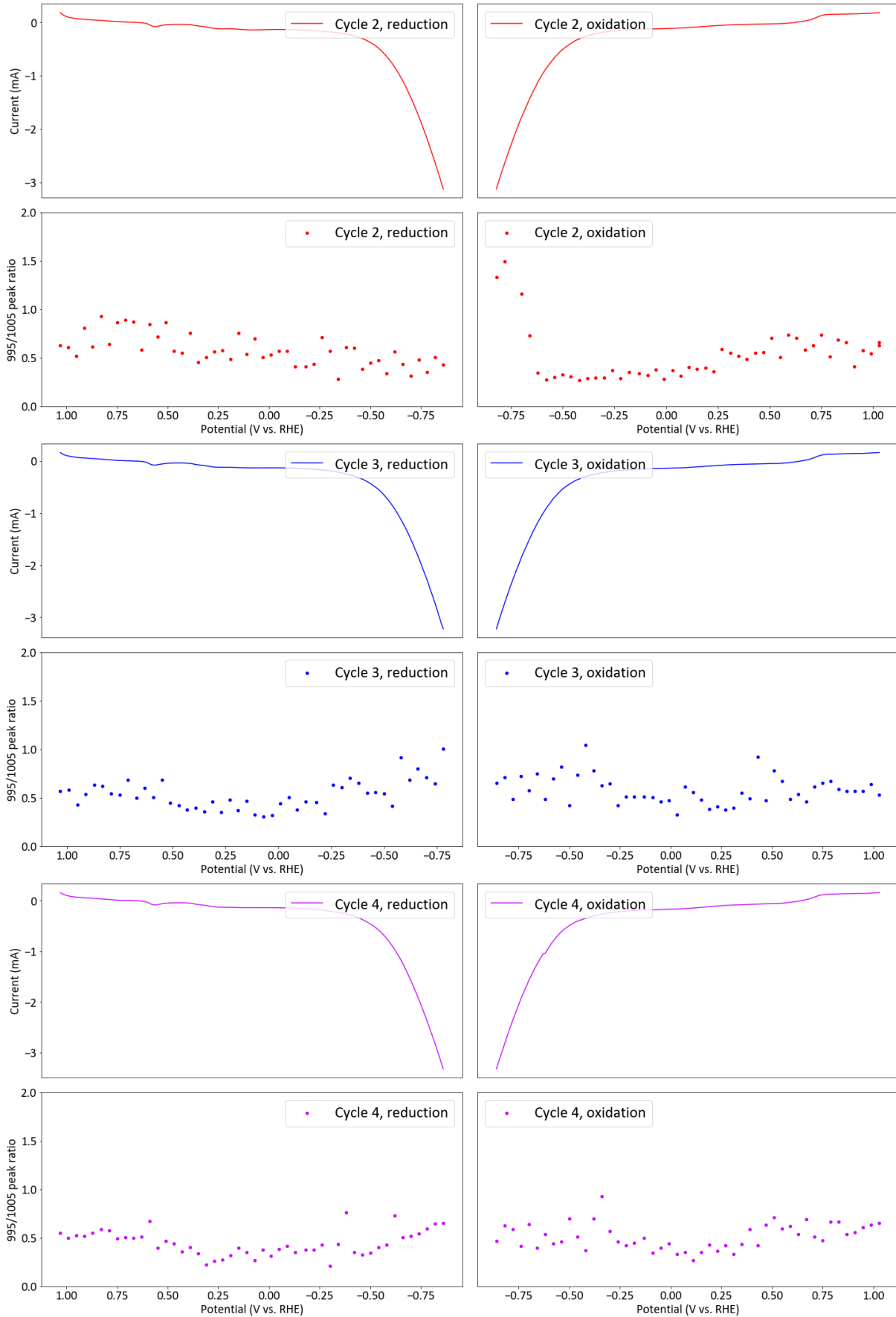


Figure 52. The 995/1005  $\text{cm}^{-1}$  peak ratio during the RCV measurement for the 4-MP pH probe.

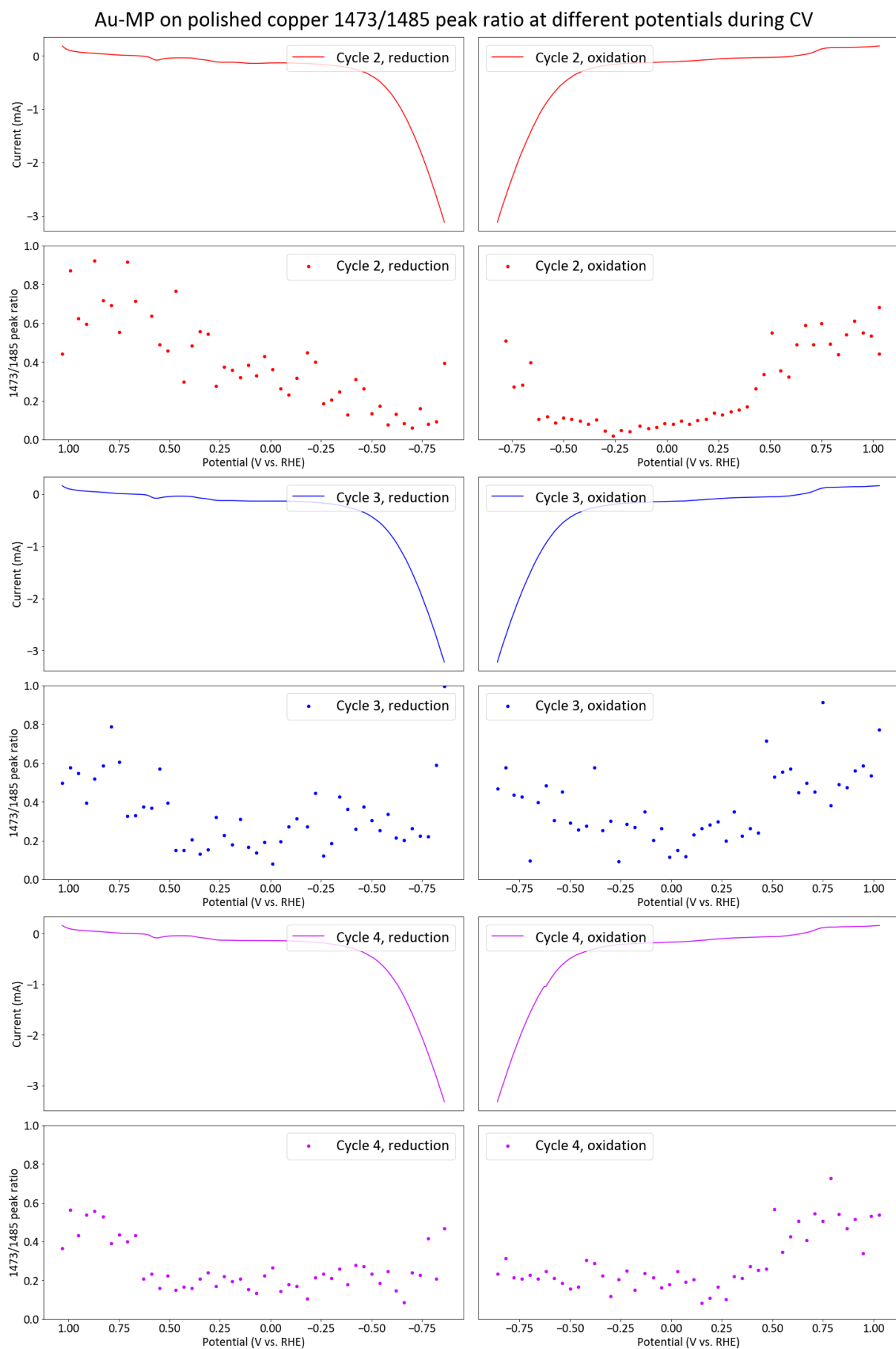


Figure 53. The 1473/1485  $\text{cm}^{-1}$  peak ratio during the RCV measurement for the 4-MP pH probe.

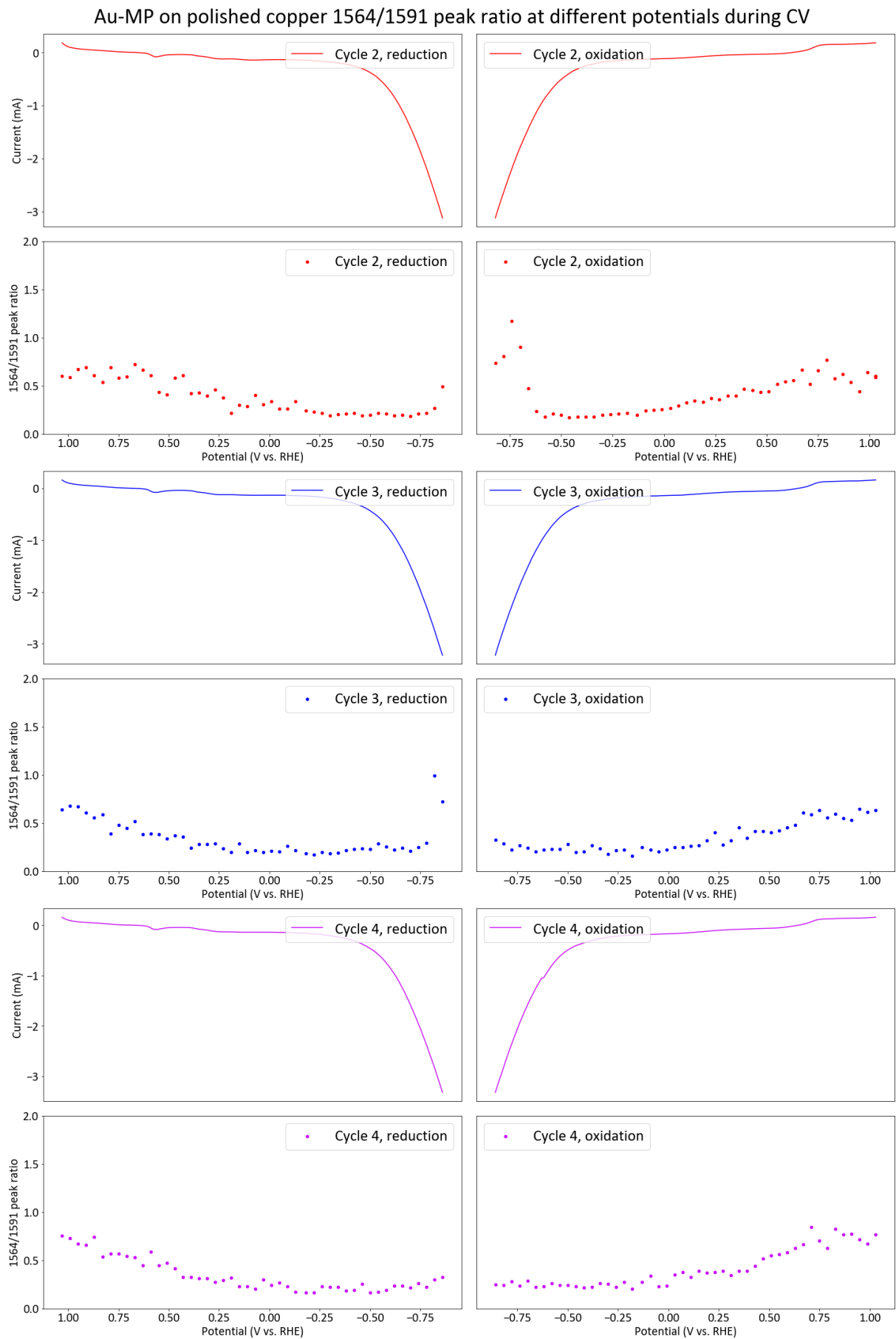


Figure 54. The 1564/1591  $\text{cm}^{-1}$  peak ratio during the RCV measurement for the 4-MP pH probe.

Au-MP on polished copper 1578/1591 peak ratio at different potentials during CV

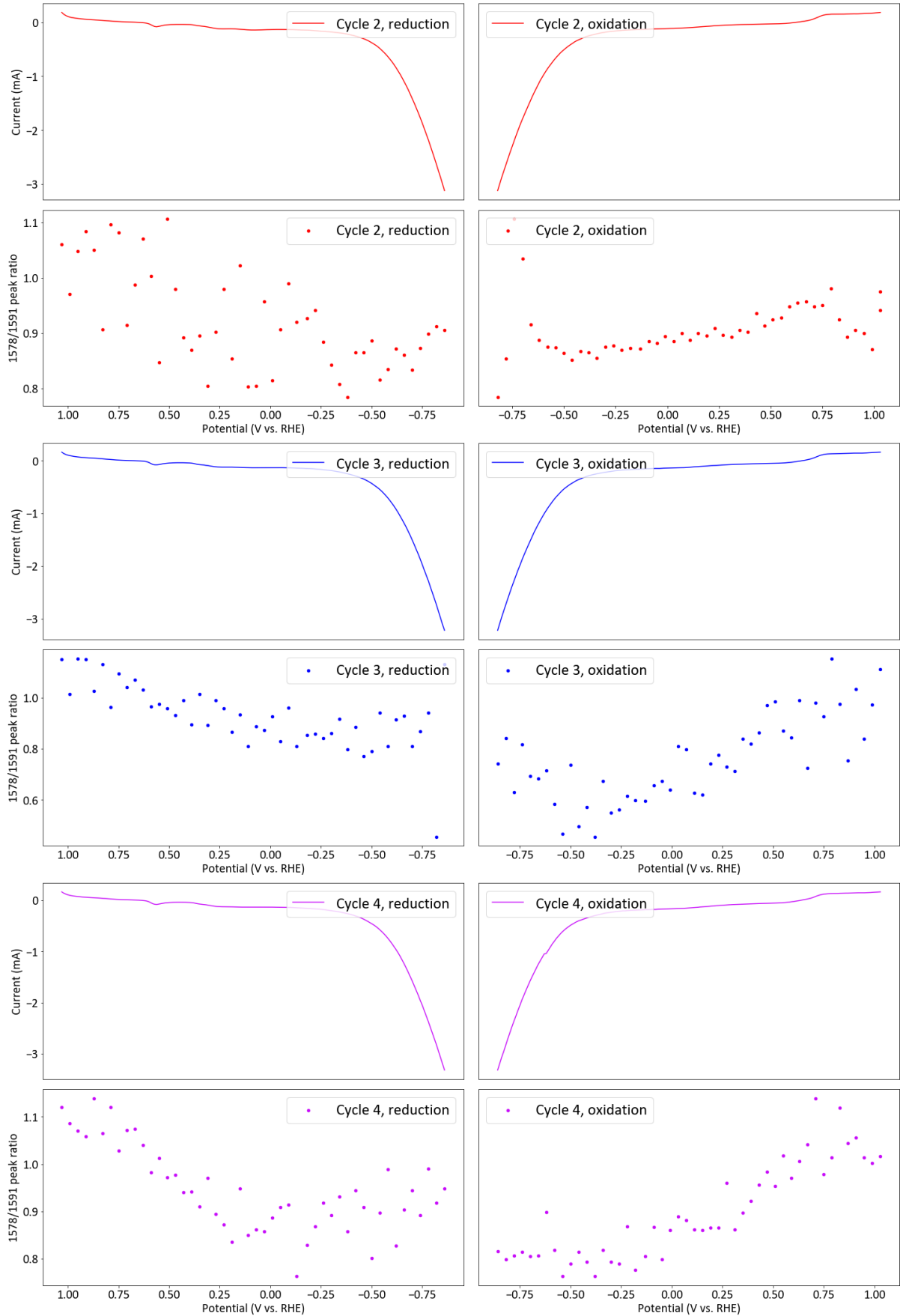


Figure 55. The 1578/1591  $\text{cm}^{-1}$  peak ratio during the RCV measurement for the 4-MP pH probe.

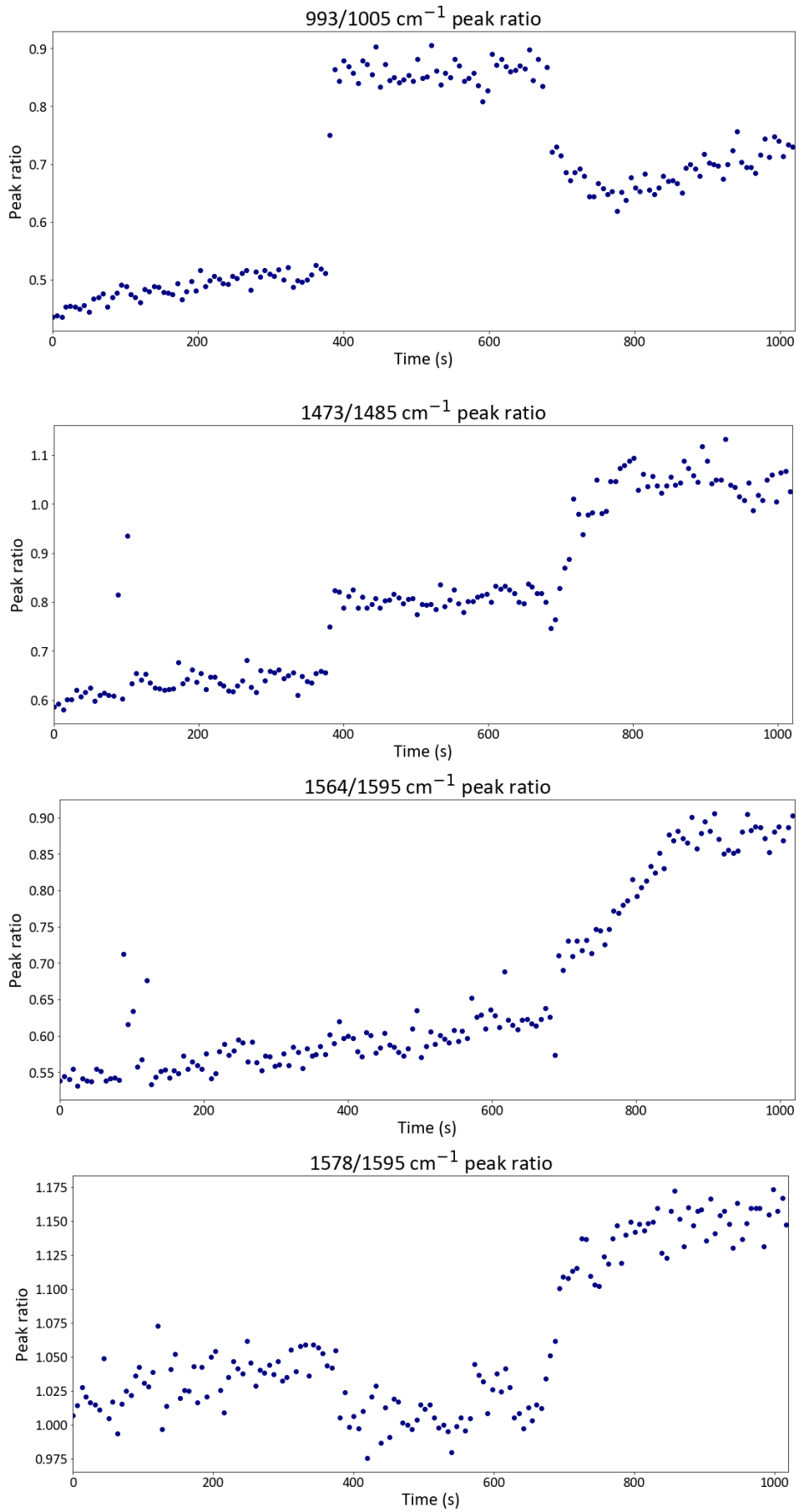


Figure 56. All trends for the static potential measurement.

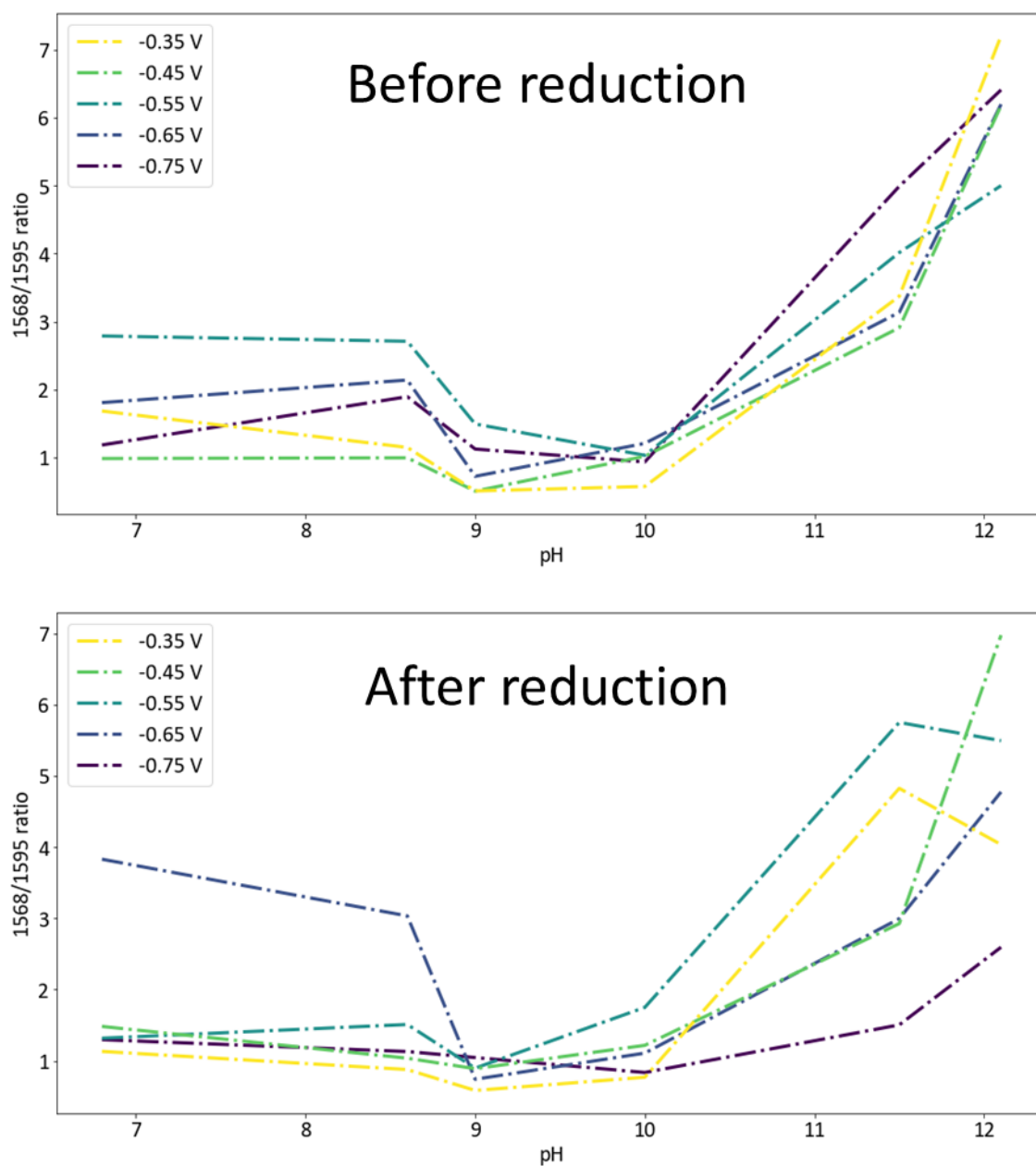


Figure 57. The 1568/1595  $\text{cm}^{-1}$  peak ratio development before (top) and after (bottom) electroreduction at given potentials in electrolytes with different pH. Results determined from the average of 10 spectra.

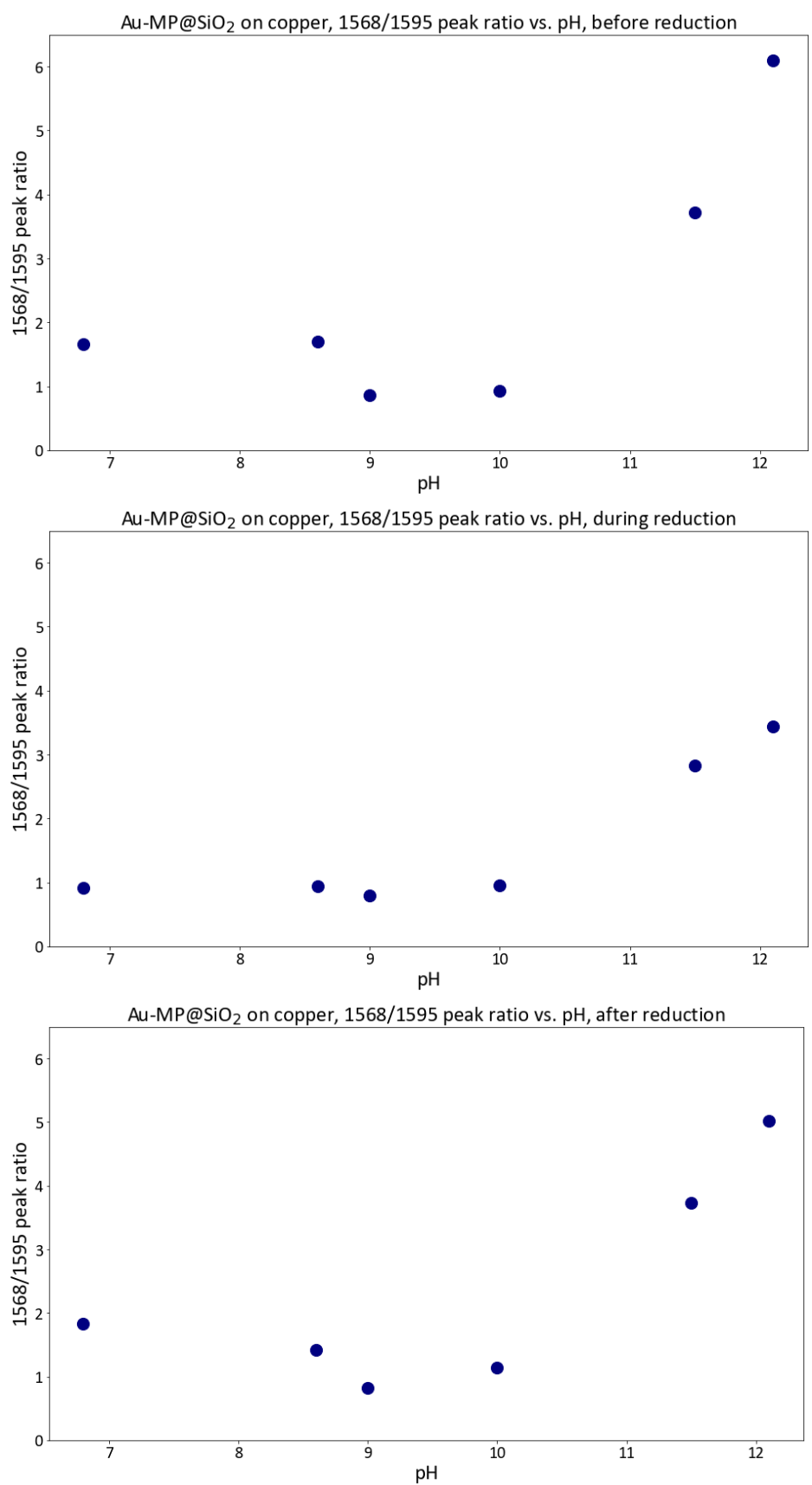


Figure 58. From top to bottom respectively: before, during and after reduction 1568/1595  $\text{cm}^{-1}$  peak ratios based on average spectra of all used potentials. Decreased ratios after reduction are ascribed to the surface still being charged. 10 spectra were taken before and after the reduction, and 50 spectra were collected during the reduction.

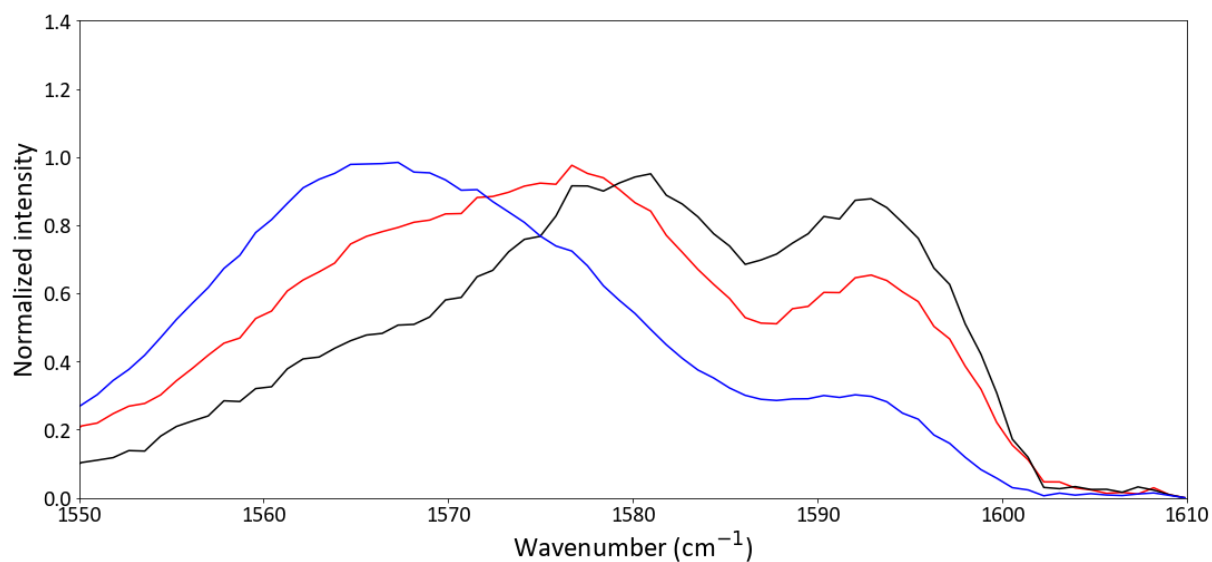


Figure 59. Close-up of the peaks at 1560-1600  $\text{cm}^{-1}$  for the [+0.55V, -0.55V, +0.55V] measurement of the 4-MP probe. Spectra based on the average of 50 spectra for each step.